Numerical Simulation of Stress Generation and Whisker Growth in Sn Films

by

Eric J. Buchovecky

M.S., Earth Science, Massachusetts Institute of Technology, 1992

M.Ed., Teaching and Learning, Harvard University, 1992

B.S.E., Civil Engineering, Princeton University, 1986

A dissertation submitted in partial fulfillment of the
requirements for the Degree of Doctor of Philosophy
in the Division of Engineering at Brown University

Providence, Rhode Island

May 2010

This dissertation by Eric J. Buchovecky is accepted in its present form by the Division of Engineering as satisfying the dissertation requirement for the degree of Doctor of Philosophy.

Date _____ _____

Professor Allan F. Bower, Advisor

Recommended to the Graduate Council

Date _____ _____

Professor K. Sharvan Kumar, Reader

Date _____ _____

Professor Pradeep Guduru, Reader

Approved by the Graduate Council

Date _____ _____

Professor Sheila Bonde
Dean of the Graduate School

Vita

Eric Buchovecky was born on December 26, 1964 in Pittsburgh, Pennsylvania. He studied Civil Engineering and Geology at Princeton University where he received the Bachelor of Science in Engineering degree in 1986. After working as an environmental and geotechnical engineer for SRW-ICF, Inc. in Pittsburgh for three years, he began graduate study in Structural Geology at MIT in Cambridge, MA. In 1992 he received the Master of Science degree from MIT and the Master of Education degree with specialization in physics instruction from Harvard University. From 1992 until 2003, he taught physics in public high schools in Massachusetts and Vermont, and consulted on a number of curriculum development and education reform projects.

Acknowledgements

I am deeply grateful for the guidance, support, and continual encouragement provided by Professor Allan Bower throughout this project. His incisive ability to cut straight to the core of a problem stands as a model I can only hope to emulate. I would also like to express my gratitude to Professor Eric Chason, who originally piqued my interest in this problem. His infectious enthusiasm and ceaseless curiosity has been an inspiration that has carried me along. I would like to thank my readers Professor Sharvan Kumar and Professor Pradeep Guduru for taking time out of their schedules to review my work and provide thoughtful critique and valuable insights.

I am indebted to all of my friends and colleagues at Brown who have enriched my academic life and made my time here so enjoyable. Among them, a few names deserve special mention, particularly Nikhil Medhekar, Rassin Grantab, Asha Nurse, Tanmay Bhandakkar, Prateek Nath, Ningning Du, Dave Cipoletti, Nitin Jadhav, Dhananjay Tambe and Ram Hariharaputran.

I thank my parents for encouraging me to aim high, yet helping me stay grounded along the way. Their unconditional support has been a source of comfort and strength.

Finally, none of this would have been possible without the unwaivering love and support of my wife, Holly, and our two children Benjamin and Anya. They have been a source of joy and comfort throughout this long process, and have kept me in touch with the things that really matter.

Contents

⋆ Parts of this thesis have appeared in the following peer-reviewed publications:

Buchovecky, E. J., Du, N. and Bower, A. F. (2009),'A model of Sn whisker growth by coupled plastic flow and grain boundary diffusion', *Applied Physics Letters* **94** (191904).

Buchovecky, E. J., Jadhav, N., Bower, A. F. and Chason, E. (2009),'Finite element modeling of stress evolution in Sn films due to growth of the Cu_6Sn_5 intermetallic compound', *Journal of Electronic Materials* **38** (2676–2684).

Jadhav, N., Buchovecky, E. J., Reinbold, L., Kumar, S., Bower, A. F. and Chason, E. (2010),'Understanding the correlation between intermetallic growth, stress evolution and Sn whisker nucleation', *IEEE Transactions on Electronics Packaging Manufacturing*. [accepted]

List of Tables

List of Figures

Chapter 1

Introduction

When a thin film of pure tin is deposited on copper, filamentary "whiskers" often grow spontaneously from the surface of the tin. Understanding this process and how to mitigate it is critically important to the electronics industry, as tin-based coatings are routinely applied to copper conductors to improve solderability and reduce corrosion [Galyon (2005)]. The growth of whiskers on closely spaced interconnects in electronic components can result in electrical short-circuit, and the consequences of such failures, particularly in high-reliability applications such as satellites and missiles, are at best costly and have the potential to be catastrophic. As an example, at least four commercial satellites have been rendered inoperable due to Sn whisker formation, and whiskers have been implicated in numerous other failures involving satellites, missiles, aircraft, medical equipment and even the control system for a nuclear power plant [NASA (2009)].

Until recently, whisker formation has been effectively suppressed by alloying the tin plating layer with a few percent lead (Pb) [Arnold (1959), Galyon (2005)]. However, enactment of "The Restriction of the Use of Certain Hazardous Substances in Electrical and Electronic Equipment Regulations" (known by the acronym RoHS) by the European Union in 2006 and the anticipated passage of similar legislation in the

United States has prompted a rapid transition to Pb-free manufacturing practices within the electronics industry. In response, the majority of electronic component manufacturers have reverted to the use of pure Sn plating, as it is the simplest and most cost-effective means of eliminating Pb from plating formulations [iNEMI (2006)]. Consequently, the potential for component failure due to whisker growth from Sn-plated components has re-emerged as a significant threat, and the high-reliability electronics industry is urgently seeking new whisker mitigation strategies. This has prompted a major resurgence of research activity into whisker growth and renewed interest in understanding its fundamental mechanisms. The current understanding of whisker growth can be summarized as follows.

Among the most widely accepted and least controversial ideas is that compressive stress within the film provides the driving force for whisker growth in high-mobility metals (*e.g.* Sn, Cd, Zn) [Fisher *et al.* (1954), Tu (1973), Lee and Lee (1998), iNEMI (2006)]. This stress can result from externally applied pressure [Fisher *et al.* (1954), Pitt and Henning (1964), Shibutani *et al.* (2006), Lin *et al.* (2007)], residual stress due to deposition [Lindborg (1975)], thermal expansion mismatch between the film and substrate [Chaudhari (1974), Nakadaira *et al.* (2007)], post-deposition bending or forming, or the growth of an intermetallic phase [Tu (1973), Lee and Lee (1998)]. In the industrially important system of Sn coatings on Cu, stress generation by the growth of intermetallic compounds (IMC's) is of particular concern as the reaction proceeds spontaneously at room temperature, is difficult to suppress, and can continue for a period of months to years [Tu (1973), Tu and Thompson (1982)].

Whisker growth is generally viewed as a mechanism for relaxing compressive stress in the Sn by transporting material out of the plane of the film. Given that whiskers typically attain lengths many times greater than the thickness of the film and the film immediately surrounding a whisker does not show signs of obvious thinning, it

is widely assumed that long-range transport is necessary to supply sufficient material to the whisker to sustain growth [Fisher *et al.* (1954), Chaudhari (1974), Tu (1994), Hutchinson *et al.* (2004)]. Self-diffusion along grain boundaries provides a likely transport pathway in room temperature Sn, as this process is several orders of magnitude faster than lattice self-diffusion [Gale and Totemeier (2004), Lange and Bergner (1962)]. Recent experimental work byReinbold *et al.* (2009) provides strong evidence for long-range transport of Sn by grain boundary diffusion associated with stress build-up and whisker formation. Other fast transport mechanisms such as pipe diffusion [Nakadaira *et al.* (2007)] and grain boundary fluid transport [Tu and Li (2005)] have also been proposed.

While the preceding ideas provide a useful framework for understanding whisker growth, many questions remain. In the case of spontaneous whisker growth from Sn-Cu bimetallic films, the mechanisms by which IMC growth generates stress within the Sn film are not fully understood. Experimental evidence shows a clear correlation between the build-up of compressive stress and the growth of IMC within the Sn film [Tu (1973), Lee and Lee (1998), Boettinger *et al.* (2005), Reinbold (2007), Chason *et al.* (2008)]. However, the relationship is not straightforward. Previous quantitative analyses which make simplifying assumptions about the material behavior (*e.g.* purely elastic deformation), the geometry (*e.g.* uniform IMC layer), or both, do not adequately explain the observed relationship between stress and IMC growth.

Despite intensive study and a large body of experimental data, a comprehensive understanding of the processes controlling whisker growth has been surprisingly elusive. In part, this is due to the large number of process variables affecting whisker formation which makes correlation of results from different experiments difficult. Among these variables are "plating bath chemistry, impurities, deposition rates, substrate material, thickness and grain size of the deposit, residual stress, alloying, temperature,

atmosphere and humidity and surface layers" [Reinbold (2007)]. Further complicating the problem is the fact that the phase transformation, deformation, and transport processes involved appear to be coupled in complex and non-linear ways. Thus it is extremely challenging, if not impossible, to design experiments that can systematically probe the relative importance of individual mechanisms.

The ability to conceive of and evaluate new whisker mitigation strategies is limited by our incomplete understanding of the fundamental processes controlling whisker growth and how they are coupled. At present, the primary guiding principle for whisker mitigation strategies is to minimize the development of compressive stress in the Sn [iNEMI (2006)]. A number of treatments such as reflow (fusing of the plating layer after deposition) and post-bake (post-deposition annealing) have been shown to reduce or eliminate both compressive stress in the Sn and whisker growth. However, prediction of their long-term performance requires knowledge of how stress develops within the Sn film and, consequently, the mechanisms by which these treatments are able to prevent stress build up. Without a fundamental understanding of the mechanisms of stress generation and relaxation, it is difficult to determine whether a particular treatment will prevent the development of stress indefinitely or merely delay its build up. As an example, Sobiech *et al.*(2007) found that stress in a pure Sn plating on Cu remained tensile for one month after post-bake treatment, but within a year compressive stress developed that was nearly equal to that measured in untreated samples.

The research presented in this thesis aims to provide quantitative analysis of the mechanical processes involved in whisker growth. The focus is limited to Sn films on Cu, in which IMC growth has been clearly correlated with the development of compressive stress within the Sn. The primary goals are to understand how IMC growth generates stress in the Sn film and how that stress ultimately results in whisker

growth.

To investigate these questions a finite element model is developed that includes the essential features of the three-dimensional geometry of the system as well as the key mechanical behavior of the materials involved. The primary purpose of the modeling is to reveal how IMC growth, elastic-plastic deformation within Sn grains and mass diffusion along grain boundaries interact to produce the experimentally observed behavior. Numerical simulation is used as a tool to quantitatively test the consequences of different assumptions about material behavior and explore the plausibility of proposed mechanisms. The modeling is not intended to replicate the full complexity of the Sn-Cu system, but rather to probe the combined effects of several of the most important processes.

The remainder of this chapter provides a more detailed description of the Sn-Cu system followed by a brief discussion of experimental results that help frame the questions that will be examined in subsequent chapters.

1.1 Phenomenological Description

Before considering the driving forces and mechanisms for whisker growth, it is useful to review the characteristics of both whiskers and the films from which they grow. The following sections provide a brief overview of the physical features of pure Sn films and whiskers, as well as a summary of measured whisker densities and growth rates. The purpose is to provide the necessary background for discussing theories of whisker growth in subsequent sections.

1.1.1 Characteristics of Thin Sn Films

The most common method of applying Sn coatings to electronic components is by electroplating. Depending on the processing conditions, two distinct forms of electroplated Sn are possible, one with a matte surface luster ("matte Sn"), the other with a shinier, more reflective surface ("bright Sn"). Both bright and matte Sn electroplate, as well as vapor-deposited Sn films, exhibit a well-developed columnar microstructure with nearly all Sn-Sn grain boundaries extending from the substrate to the free surface. This microstructure is characteristic of pure Sn films including those produced by vapor deposition, and is very difficult to disrupt or alter through processing. In sharp contrast, films of Sn-Pb alloys exhibit a much more equiaxed grain structure with Sn-Sn grain boundaries of all orientations present. As will be discussed in Chapter 3, the columnar microstructure of pure Sn plays a key role in stress development and whisker growth by constraining relaxation via Coble creep.

Typically, Sn plating for electronic applications ranges in thickness from 1 to 10μm. In matte Sn the mean grain size is comparable to the thickness of the film (typically 1–5μm[Smetana (2007*a*)]) and tends to increase with film thickness in a systematic way. In one study, grain size was shown to scale as the square root of film thickness [Tsuji (2003)]. Since the plating thickness increases steadily during deposition, the correlation between grain size and film thickness for identically processed films indicates that grain size must increase during the deposition process.

The grain size of bright Sn (measured in the plane of the film) is smaller than that of matte Sn. Grain size less than 1 μm is used as a defining characteristic in distinguishing bright from matte Sn [Smetana (2007*a*)]. The columnar grains of bright Sn are typically more elongated than those of matte Sn. The higher aspect ratio of bright Sn grains may be the consequence of low grain boundary mobility [Boettinger *et al.* (2005)]. Bright Sn coatings also tend to have higher carbon content, develop higher

compressive stress and are more prone to whisker growth than matte Sn [Smetana (2007*a*)].

In addition to columnar microstructure, Sn films often exhibit a preferred crystallographic orientation, or crystal texture. The specific orientation for a given film depends on details of the deposition process [Lee and Lee (1998), Zhao *et al.* (2006)], and a wide range of preferred orientations has been reported in the whisker literature (see, for example, the summary table presented in [Galyon (2005)]). The most commonly reported preferred crystal orientations associated with whisker growth are (220) and (321) [Galyon (2005)]. However, not all studies provide grain orientation information, so it is difficult to generalize about the effect of texture on a film's likelihood to form whiskers based on existing experimental work.

Crystal texture has the potential to significantly influence the mechanical behavior of polycrystalline Sn films due to the highly anisotropic properties of the individual crystal grains [*e.g.* Bieler *et al.* (2008), Zamiri *et al.* (2008)]. Crystalline Sn has body centered tetragonal (bct) structure with the c-axis dimension of the unit cell approximately half that of the two equivalent a-axes ($\frac{c}{a} = 0.55$) [Gale and Totemeier (2004)]. This gives the unit cell the form of a cube shortened along one dimension. Material properties vary significantly with crystal orientation. For example, the elastic stiffness in the [001] direction is more than 50% greater than that in the [100] and [010] directions, and the coefficient of thermal expansion (CTE) in the [001] direction is twice as great as in the [100] and [010] directions. The low symmetry of the Sn crystal also results in anisotropic single-crystal plastic deformation due to dislocation motion on a complex set of slip systems comprising as many as ten distinct slip plane–slip direction families [Barrett (1943), Fujiwara and Hirokawa (1987), Kirichenko (1987), Nagasaka (1989), Zamiri *et al.* (2008)].

1.1.2 Physical Description of Sn Whiskers

Tin whiskers are long, slender single crystal grains that emerge from the surface of the film (see Figure 1.1). They typically grow to lengths measured in tens of microns but have been known to attain lengths up to 10 mm [NASA (2009)]. The diameter and cross-sectional shape of whiskers are often similar to those of the columnar grains in the surrounding Sn film. Irregularities in the cross-sectional shape persist along the length of the whisker producing longitudinal striations. Morphologically there appears to be no systematic difference between whiskers which grow spontaneously due to IMC growth and those induced by externally applied pressure or thermal expansion mismatch. In addition to whiskers, hillocks and other irregularly shaped surface protrusions are also observed.

Koonce and Arnold (1954), showed that whiskers grow by addition of material at their base or "root" as evidenced by the observation that distinctive morphologic features at the tip are carried along unaltered during growth. A number of cross-sectional scanning electron microscope (SEM) images prepared by focused ion beam (FIB) thinning have been published showing whisker roots terminating at obliquely angled grain boundaries within the Sn film, rather than extending to the base of the film (see Figure 1.2) [Sheng *et al.* (2002), Hutchinson *et al.* (2004), Smetana (2007*b*)]. Whether these grain boundaries are present in the as-deposited film or result from subsequent grain growth or recrystallization is the subject of ongoing debate, as are the mechanisms by which new material is accreted to the whisker [Boettinger *et al.* (2005), Smetana (2007*b*), Vianco and Rejent (2009)].

Several studies have examined the growth direction of individual whiskers. Based on a compilation of 30 measurements from various sources, Ellis *et al.* (1958) showed that no single crystallographic growth direction was preferred for Sn whisker growth. They did note however that low index directions were favored (*e.g.* $\langle 100 \rangle$, $\langle 001 \rangle$, $\langle 101 \rangle$, $\langle 123 \rangle$).

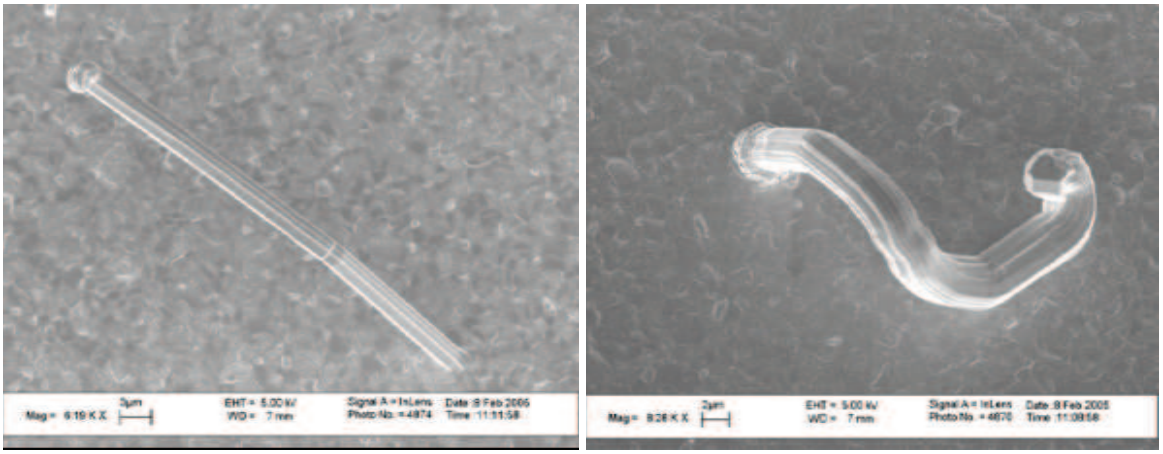

Figure 1.1: Scanning electron microscope (SEM) images of whiskers emerging from a Sn film. Note the longitudinal striations and abrupt changes in growth direction. (Replace with images from Nitin – note that kinked whisker is from the copper-top sample of Lucy's).

Later Lee and Lee (1998) analyzed whisker growth direction in relation to the texture of the film for two samples and found that the bases of all the whiskers they examined shared the same crystallographic orientation and that that orientation differed from the dominant crystal orientation within the film. Hutchinson *et al.* (2004) also found that whiskers tended to have growth directions different from the surrounding grains in the film, but, like Ellis *et al.* (1958), they observed multiple low-index whisker growth directions.

When Sn is deposited on Cu, whiskers do not form immediately. Nucleation of the first whiskers is preceded by a latency, or "incubation", period lasting from hours to months or even years after deposition. Incubation periods of a few days are typically reported for pure matte Sn on Cu aged at room temperature [Reinbold (2007), Sobiech *et al.* (2008), Chason *et al.* (2008)]. After initial nucleation, the number density of whiskers (number/area) has been observed to increase at a rate that decreases with time [Lee and Lee (1998), Chason *et al.* (2008), Jadhav *et al.* (2010)]. Number densities ranging from $10^3/\text{cm}^2$ to $10^4/\text{cm}^2$ have been reported after

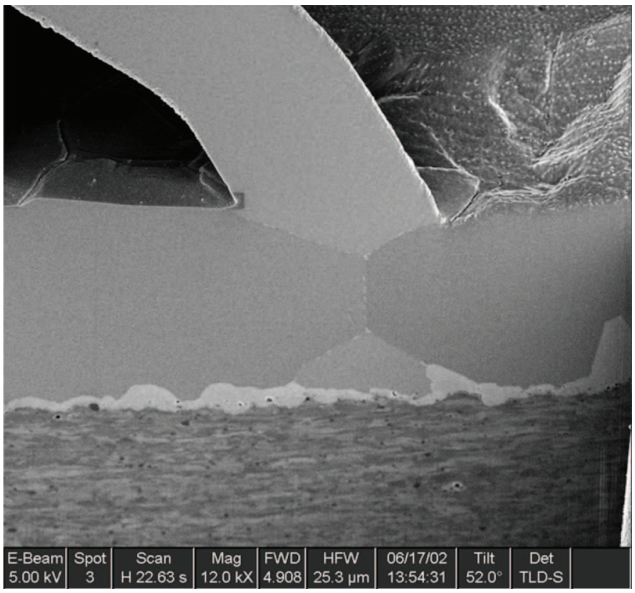

Figure 1.2: Cross-sectional SEM/FIB image of a whisker root showing oblique angle grain boundaries separating the whisker from Sn grains within the film. Micrograph by Nick Vo, Freescale Semiconductors, Inc. [Smetana (2007*b*)].

1 to 2 months of aging [Tu (1973), Lee and Lee (1998)]. The distribution of whiskers across the surface of the film appears to be random, with two whiskers occasionally emerging much nearer to each other than the mean spacing.

1.2 Correlated measurements of IMC volume, Sn stress, and whisker density

The computational work presented in this thesis was motivated, in large part, by experimental work conducted by Eric Chason's research group at Brown University. In this section I briefly describe the results of one series of experiments that illustrate some of the central questions addressed by the computational work. More thorough analyses of these data and detailed descriptions of the experimental methods have been publish previously [Chason *et al.* (2008), Jadhav *et al.* (2010)].

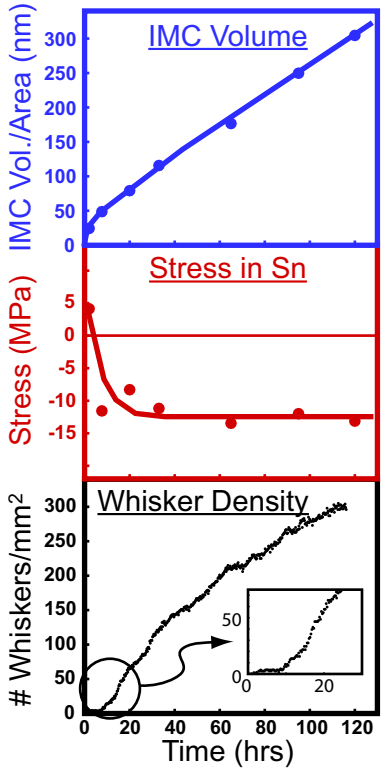

Figure 1.3: Correlated measurements of IMC volume (blue), stress in the Sn (red) and whisker density (black) for a 1.45 μm Sn film on Cu. Graphs stacked vertically share the same time axis and data points on the IMC volume and Sn stress plots are measurements from the same samples made at the same time. The curves have been added as a visual guide. [Chason *et al.* (2008), Jadhav *et al.* (2010)].

The data presented in Figure 1.3 are from carefully designed experiments that allow direct correlation among measurements of IMC volume, stress and whisker density for matte Sn films electroplated on Cu. In the figure, graphs stacked vertically share the same time axis.

Looking first at the IMC growth data, we see that IMC volume increases monotonically and that the rate of growth is initial fast, then slows somewhat with time. If we now consider the in-plane stress measured in the same samples we see that the stress is initially tensile, then quickly becomes compressive. Within about 20 hours, the stress reaches a maximum compressive value then remains relatively constant over

time. Important things to notice here are that the total IMC volume is quite small when the stress reaches its "steady state" level, and that the stress remains constant even as IMC continues to grow. Turning our attention to the whisker density, we see that first the whiskers do not nucleate until after about 10 hours. Then the number of whiskers increases monotonically at a rate than decreases with time.

The fact that the stress level remains constant as IMC continues to grow indicates that stress generated by IMC growth must be simultaneously relaxed. The question is, what processes are responsible for this relaxation? In particular, we would like to know whether whisker growth alone can account for the observed relaxation, or if other processes such as plastic deformation within the film are involved. Evidence from transmission electron microscope study indicates extensive dislocation emission within the Sn grains in neighborhood of IMC particles growing into the film [Kumar *et al.* (2008)]. There is also evidence for the long-range transmission of stress through the film via grain boundary self-diffusion [Reinbold *et al.* (2009)].

In the following chapters, computational modeling is used first to test whether plastic relaxation processes operating within the film are sufficient to account for the balance between stress generation and relaxation, without the growth of whiskers. This is found to be true. Finite element modeling is then used to understand how relaxation is partitioned between plastic deformation within the film and whisker growth, and at the same time, investigate the factors controlling the growth velocity of whiskers.

This thesis is structured as follows. In Chapter 2 we present a finite element model that includes the essential features of the three-dimensional geometry of the system, elastic and plastic deformation within Sn grains, stress-driven diffusion along grain boundaries, and the mechanical effects of the IMC transformation reaction.

In Chapter 3 the finite element model is used to investigate the generation of stress

due to the growth of discrete IMC particles at the base of the Sn film. Through numerical simulation we test the effects of different assumptions about material behavior. We conclude that the coupled action of intra-granular plastic deformation and grain boundary diffusion provide an important mechanism for stress transmission through the film.

In Chapter 4 the finite element model is extended to include a mechanism for whisker growth and the relationship between whisker growth velocity and IMC growth rate is explored. The partitioning of strain relaxation between whisker growth and intra-granular plastic flow is also examined.

In Chapter 5 an analytical model for whisker growth velocity is presented. The model includes the effects of strain generation and strain relaxation by both whisker growth and intra-granular plastic flow. The model is also applied to the case of whisker growth caused by thermal cycling.

Chapter 6 presents the conclusions gathered from this work.

Chapter 2

Finite Element Formulation

The primary goals of this work are to understand how IMC growth generates stress in the Sn film and how that stress ultimately results in whisker growth. Experimental evidence suggests that strain produced by localized expansion of IMC particles is accommodated by both dislocation motion within Sn grains and mass diffusion along Sn-Sn grain boundaries. Understanding the mechanisms by which these processes generate stress and drive whisker growth requires knowledge of the microscopic stress field within the Sn and how it evolves over time. Experimental measurement of stress at a spatial resolution comparable to the size of IMC particles is exceedingly difficult and cannot be directly correlated with dislocation-mediated plastic deformation within the grains or with grain boundary diffusion[1]. Computational modeling, however, offers a means of predicting the stress that develops. The microstructure and constitutive behavior of the material can be directly specified and the consequent deformation and stress evolution calculated. While no model can fully

[1]High energy X-ray diffraction can provide sub-micron resolution measurement of deviatoric strain within the Sn film and a number of recent studies make use of this technique [Choi *et al.* (2003), Sobiech *et al.* (2009)]. Due to the anisotropic elastic properties of the Sn crystals, however, the stress tensor, and even the deviatoric stress tensor, cannot be fully determined from the deviatoric strain. Furthermore, the deviatoric strain reflects only the elastic distortion of the crystals and provides no information regarding the amount of plastic deformation that may have accumulated.

replicate the behavior of the real system, models do allow the free manipulation of material properties in a way that is not possible experimentally. Used as a complement to experimental measurement, computational modeling provides an efficient means to explore and test the roles played by different processes and mechanisms.

Toward this end, we develop a finite element model that captures the essential features of the three-dimensional geometry of the system as well as the key mechanical behavior of the materials involved. The primary purpose of this model is to reveal how elastic-plastic deformation within Sn grains and mass diffusion along grain boundaries couple with one another at the microscopic level to produce the experimentally-observed macroscopic behavior. To highlight these relationships and facilitate the interpretation of the model results, a number of simplifying assumptions and approximations have been made, as described in the following sections. The remainder of this chapter describes a finite element approach that accounts for strain generation due to the IMC transformation reaction and accommodation of that strain by dislocation motion within Sn grains and stress-driven mass transport along Sn-Sn grain boundaries.

2.1 Model Geometry

As discussed in Chapter 1, both the columnar microstructure of the Sn film and the non-uniform distribution of discrete IMC particles growing at Cu-Sn interface are believed to contribute to the development of compressive stress. These features are incorporated into a finite element model that simulates a polycrystalline Sn film with columnar grain structure bonded to a Cu substrate, as shown in Figure 2.1. The copper substrate is treated as a homogeneous solid, while the Sn film is idealized as a periodic array of identical hexagonal grains. The Sn grains are separated by

vertically-oriented[2] grain boundaries which support stress-driven diffusion and inter-grain sliding. Symmetry boundary conditions (zero lateral displacement and zero grain boundary flux) applied at the lateral boundaries of the model cell create a periodic repetition of the model in the in-plane directions. Zero displacement conditions are imposed at the base of the Cu substrate layer. Vertical displacement is unconstrained at the surface of the Sn and the lateral boundaries.

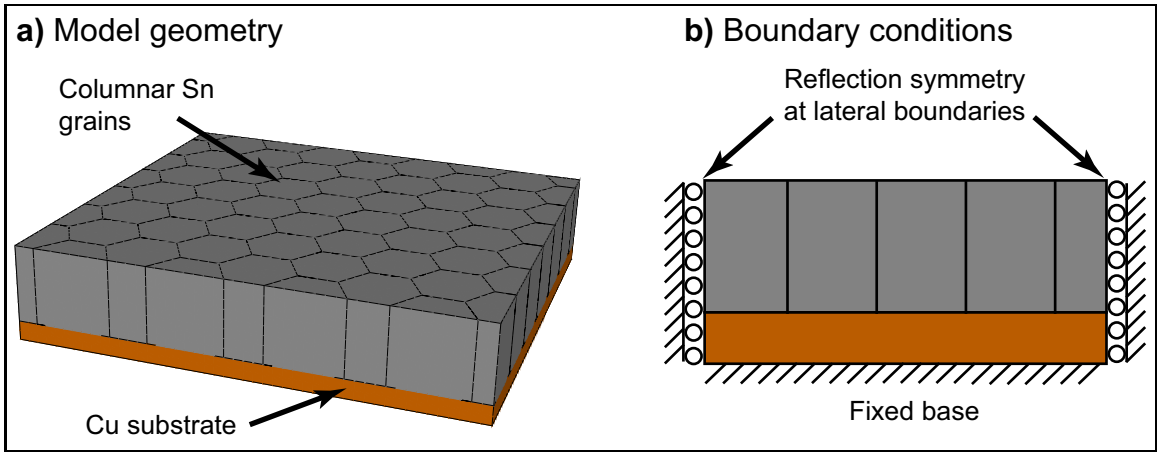

Figure 2.1: a) The Sn film is idealized as a periodic array of columnar hexagonal grains bonded to a Cu substrate. b) Lateral dimensions of the model cell are held fixed (reflection symmetry conditions) and no displacement is allowed at the base of the Cu substrate. Vertical displacement is unconstrained at the surface of the Sn and along the lateral boundaries.

2.2 Deformation Within Sn Grains

Isotropic elastic-plastic constitutive behavior is assumed within the individual Sn grains with plastic deformation governed by either rate-independent plastic yield or rate-dependent viscoplasticity. While the constitutive behavior of single-crystal Sn is known to be significantly more complex, exhibiting anisotropy in elastic, plastic

[2]For convenience, the terms horizontal and vertical will be used to describe the in-plane and out-of-plane directions, respectively.

and thermal properties, we have chosen to make this approximation for the following reasons. First, limited experimental data exist to characterize dislocation-mediated plastic deformation within Sn single crystals. While experimental measurements of critical resolved shear stress (CRSS) have been reported for six of the ten slip system families that have been identified in Sn, there is disagreement regarding the order in which slip systems are activated and inconsistency among the reported CRSS values [Barrett (1943), Weertman and Breen (1956), Hirokawa *et al.* (1968), Fujiwara and Hirokawa (1987), Kirichenko (1987), Nagasaka (1999), Zamiri *et al.* (2008)]. Second, detailed grain orientation data are not available for the Sn films which provide the experimental basis for the finite element modeling. For these reasons, a single-crystal plasticity model of deformation within Sn grains would be both difficult to validate and of limited value. The approximation of isotropic behavior within the solid grains is sufficient to evaluate the relative effectiveness of stress relaxation by intra-grain plastic deformation compared with inter-grain mass transport via grain boundary diffusion.

The elastic-plastic constitutive behavior included in the finite element implementation is briefly summarized as follows[3]. For infinitesimal deformation, the increment of total strain is decomposed into the sum of elastic and plastic components:

$$d\varepsilon_{ij} = d\varepsilon^e_{ij} + d\varepsilon^p_{ij} \tag{2.1}$$

where only the elastic strain contributes to the stress in the solid. For a linear elastic material the stress is given by:

$$\sigma_{ij} = C_{ijkl}\varepsilon^e_{kl} = C_{ijkl}\left(\varepsilon_{kl} - \varepsilon^p_{kl}\right) \tag{2.2}$$

[3]A more thorough development of the constitutive equations presented here can be found in a graduate level solid mechanics text such as Bower (2010) or Malvern (1969).

where C_{ijkl} is the elastic modulus tensor. Under the assumption of isotropic elasticity this further reduces to:

$$\sigma_{ij} = \frac{E}{(1+\nu)}\left(\frac{1}{2}\varepsilon^e_{ij} + \frac{\nu}{(1-2\nu)}\varepsilon^e_{kk}\delta_{ij}\right) \tag{2.3}$$

where E is Young's modulus and ν is Poisson's ratio. Equation 2.3 can be inverted to relate the increment of elastic strain in Equation 2.1 to the stress increment:

$$d\varepsilon^e_{ij} = \left(\frac{1+\nu}{E}\right) d\sigma_{ij} - \left(\frac{\nu}{E}\right) d\sigma_{kk}\delta_{ij}. \tag{2.4}$$

Calculation of the plastic strain increment depends on the choice of plastic flow potential and plastic flow rule. Two different plastic constitutive behaviors are considered here. The simplest is rate-independent plastic yield with isotropic hardening. The yield surface is defined by the von Mises yield criterion:

$$f(\sigma_e, \bar{\varepsilon}^p) = \sigma_e - Y(\bar{\varepsilon}^p) = 0 \tag{2.5}$$

where

$$\sigma_e \equiv \sqrt{\frac{3}{2}S_{ij}S_{ij}} \quad \text{and} \quad \bar{\varepsilon}^p \equiv \int \sqrt{\frac{3}{2}d\varepsilon^p_{ij}d\varepsilon^p_{ij}}, \tag{2.6}$$

$S_{ij} = \sigma_{ij} - \frac{1}{3}\sigma_{kk}\delta_{ij}$ is the deviatoric stress, and $Y(\bar{\varepsilon}^p) = Y_0 + h\bar{\varepsilon}^p$ is the yield stress with hardening rate h. The associated flow rule which relates the increment of plastic strain to the stress is:

$$d\varepsilon^p_{ij} = d\bar{\varepsilon}^p \frac{\partial f}{\partial \sigma_{ij}} = d\bar{\varepsilon}^p \frac{3}{2}\frac{S_{ij}}{Y}. \tag{2.7}$$

To model rate-dependent viscoplastic behavior, the plastic strain rate is specified by a von Mises flow potential with power-law rate sensitivity which has the form:

$$g(\sigma_e, \sigma_0) = \dot{\varepsilon}_0 \exp\left(\frac{-Q}{kT}\right)\left(\frac{\sigma_e}{\sigma_0}\right)^m \tag{2.8}$$

where σ_e is the von Mises equivalent stress defined above, σ_0 is the nominal yield stress which can evolve with strain, and $\dot{\varepsilon}_0$, Q, and m are material parameters that define the characteristic strain rate, activation energy, and stress sensitivity, respectively. This model assumes that plastic flow is controlled by a thermally-activated process such as dislocation climb. No hardening is included in the viscoplastic constitutive relation used in our finite element models, so σ_0 is taken to be constant. The associated plastic flow rule that specifies plastic strain rate is:

$$\dot{\varepsilon}_{ij}^{p} = \dot{\varepsilon}_0 \exp\left(\frac{-Q}{kT}\right)\left(\frac{\sigma_e}{\sigma_0}\right)^m \left(\frac{3}{2}\frac{S_{ij}}{\sigma_e}\right). \tag{2.9}$$

The choice of material parameters defining the elastic and plastic behavior of Sn and Cu in the finite element models is presented in Chapters 3 and 4.

2.3 Grain Boundary Diffusion and Sliding

In addition to elastic and plastic deformation within the solid Sn grains, we explicitly model stress-driven mass diffusion and sliding along the Sn-Sn grain boundaries. The development of the constitutive relations and finite element formulation is described in detail by Bower and Wininger (2004) for two dimensions. An extension to three dimensions implemented by Du (2009) has been incorporated into the present model. In this model, grain boundaries are treated as sharp two-dimensional surfaces that separate solid grains. Diffusional transport of atoms within the grain boundaries is governed by Fick's laws and driven by gradients in the chemical potential. In addition, shear stress across a grain boundary causes the solid grains on opposite sides to slide relative to one another at a rate proportional to the shear stress. Grain boundary migration is not included in the model.

2.3.1 Grain Boundary Diffusion

For grain boundary self-diffusion, the chemical potential is dominated by the mechanical work term associated with inserting an atom into the grain boundary. In the model, the chemical potential is approximated as $\mu = -\Omega\sigma_{\mathrm{n}}$, where Ω is the atomic volume of Sn and σ_{n} is the normal stress acting across the plane of the grain boundary. Applying Fick's first law with concentration equal to 1.0, the flux of volume along the grain boundary is given by

$$\vec{j}_{\mathrm{v}} = -\frac{\delta D_{\mathrm{gb}}}{kT}\nabla\mu = \frac{\Omega\delta D_{\mathrm{gb}}}{kT}\nabla\sigma_{\mathrm{n}} \tag{2.10}$$

where δ is the nominal grain boundary width, D_{gb} is the grain boundary diffusivity at temperature T, k is Boltzmann's constant, and the gradient is taken in the plane of the grain boundary. The diffusivity is described by an Arrhenius relation: $D_{\mathrm{gb}} = D^0_{\mathrm{gb}} \exp\left(-Q_{\mathrm{gb}}/kT\right)$ where Q_{gb} is the activation energy associated with diffusion along the grain boundary. The finite element calculations are performed at constant temperature so D_{gb} remains fixed at its room temperature value.

Differences in the normal stress across the grain boundary from one location to another lead to variations in the volume flux along the grain boundary. Net mass transport results as volume is removed from regions of more compressive normal stress and added to regions of less compressive normal stress. The rate of volume removal (per unit area) at any point in the grain boundary is given by the divergence of the volume flux (Fick's second law). Physically, the rate of volume accumulation per area describes the relative velocity of opposite faces of the grain boundary, in the direction normal to the grain boundary plane. This velocity discontinuity can be expressed as:

$$[v_{\mathrm{n}}] = \nabla\vec{j}_{\mathrm{v}} = \frac{\Omega\delta D_{\mathrm{gb}}}{kT}\nabla^2\sigma_{\mathrm{n}} \tag{2.11}$$

An additional set of constraints arises from the thermodynamic requirement that the chemical potential be continuous. In particular, at grain boundary junctions, the normal stress on each of the adjoining grain boundaries must be equal.

2.3.2 Grain Boundary Sliding

Shear stress across the grain boundary can similarly cause relative sliding motion of the opposite grain faces. In the model, the velocity discontinuity across the grain boundary is related to the resolved shear stress by means of a linear viscous constitutive law consistent with a thermally-activated process:

$$[v_{\mathrm{t}}]_i = \frac{\Omega \nu_0 \exp\left(Q_{\mathrm{gbs}}/kT\right)}{kT} \tau_{\equiv} \eta_0 \tau_i \tag{2.12}$$

where $[v_{\mathrm{t}}]_i$ is the velocity jump tangential to the grain boundary plane, ν_0 is a characteristic sliding velocity, and Q_{gbs} is the activation energy associated with grain boundary sliding. $\tau_i = \sigma_{ij} n_j - (\sigma_{kl} n_k n_l) n_i$ is the resolved shear stress on the grain boundary. For calculations at constant temperature, the relation can be expressed in terms of a single constant, η_0, which is inverse to viscosity.

2.4 IMC Transformation Reaction

One of the more challenging physical behaviors to incorporate into the model is the IMC transformation reaction. IMC growth involves the transformation of existing Sn into a new IMC phase which has greater specific molar volume and markedly different constitutive behavior. This reaction cannot simply be modeled as the expansion of a fixed material volume since the reaction front, at the interface between IMC and Sn, propagates into the Sn. Furthermore, the velocity of the interface varies with time. To model these changes in the FEA simulations, the material properties are

selectively altered at specified nodes within the finite element mesh during each time step. This approach eliminates the need to update the topology of the finite element mesh as the size of the IMC particles increases. Instead, the finite element mesh remains fixed while the IMC transformation propagates through it. Details of the implementation are as follows.

2.4.1 Defining the Transformed Region

IMC is idealized as hemispherical nodules that grow up into the Sn from the Cu-Sn interface (see Figure 2.2). The position of each nodule is specified *a priori*, as a model input, and all nodules grow simultaneously at the same rate. The radius of each IMC nodule, r_{imc}, increases incrementally over a series of time steps as shown schematically in Figure 2.2. During each time step, a thin shell of Sn surrounding the existing IMC nodules is transformed to IMC, simultaneously increasing the volume of IMC while consuming some of the Sn.

The spatial extent of the IMC is specified in the simulation by a field variable, Φ, which is assigned a value between 0 and 1 at each node of the finite element mesh. $\Phi = 0$ corresponds to Sn, while $\Phi = 1$ corresponds to IMC. Initially, all nodes within the Sn layer are assigned $\Phi = 0$. During subsequent time steps, the value of Φ is updated at nodes which are transformed to IMC. The value of Φ at each node is determined by its distance, r, from the center of the nearest IMC nodule via a smoothed step function: $\Phi = 1/2[1-\tanh(2(r-r_{\text{imc}})/w)]$ where w is the characteristic width of the IMC-Sn interface (see Figure 2.3). Note that Φ varies from 0.98 to 0.02 between $r = (r_{\text{imc}} - w)$ and $r = (r_{\text{imc}} + w)$. Smoothing of the IMC-Sn interface prevents abrupt property changes as the interface passes through the finite element mesh.

The transformation of Sn to IMC is implemented in the FEM simulations by

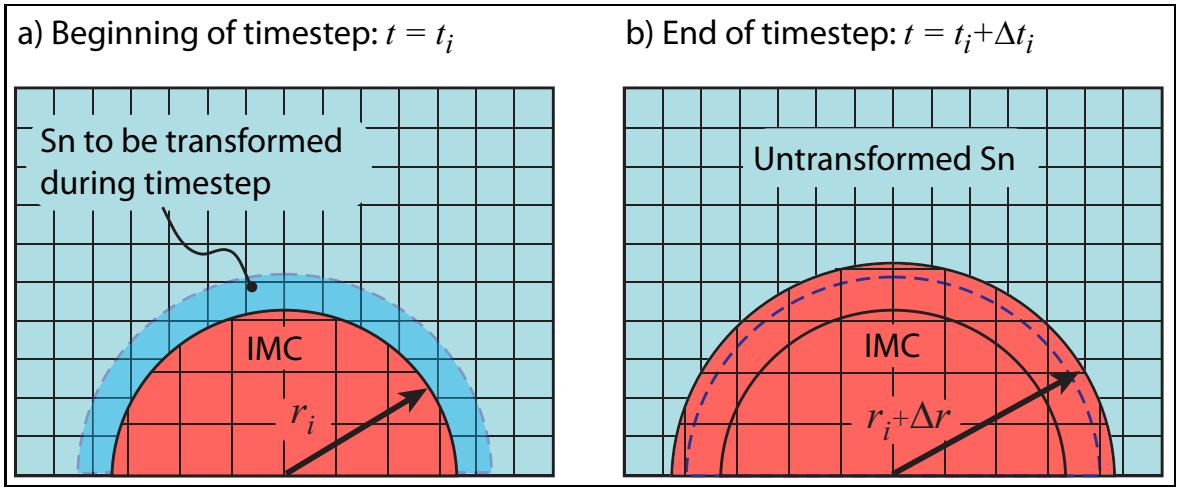

Figure 2.2: Schematic diagram showing how IMC transformation reaction is implemented in the finite element model. Red represents IMC and blue represents Sn. The superimposed grids are an aid to distinguish the region that has expanded from the unexpanded region. The grid lines do not indicate the finite element discretization. a) At the beginning of the time step, the expanded region has radius r_i. During the time step the expansion field will be applied to nodes within the shell shown in darker blue. b) By the end of the time step, the shell identified in a) has fully expanded (the full stress-free transformation strain has been applied). The new (expanded) radius of the IMC particle is $r_i + \Delta r$.

correlating material properties (elastic modulus, yield strength, molar volume) with the local value of Φ. The material has the properties of Sn where $\Phi = 0$ and the properties of IMC where $\Phi = 1$. Property values are interpolated linearly for intermediate values of Φ. The molar volume change associated with the transformation is modeled by applying a stress-free transformation strain, $\varepsilon^t = 0.13$, corresponding to a 44% stress-free volumetric expansion. After application of the transformation strain, the material is in a state of compressive stress and would have to undergo a 44% expansion to become stress-free. The applied transformation strain is the only loading in the model. The transformation process is assumed to occur quasi-statically with stress equilibrium maintained throughout the simulation.

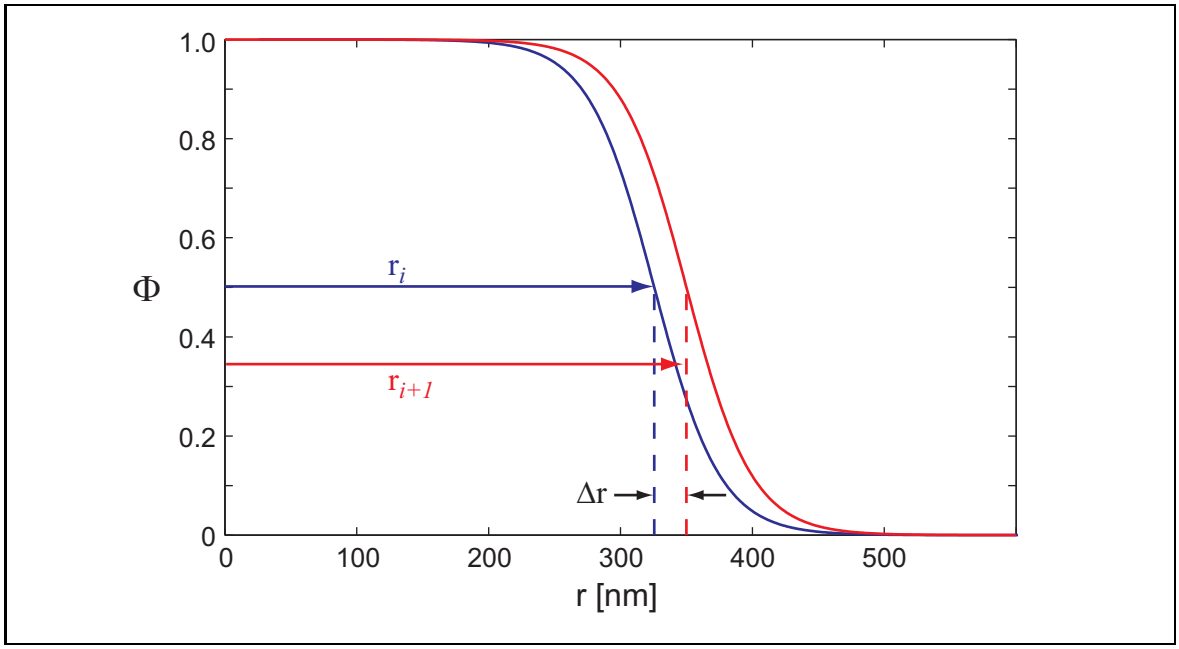

Figure 2.3: Variation of the field variable Φ with radius. The center of the IMC particle is at $r = 0$ and $\Phi(r) = 1/2[1 - \tanh(2(r - r_{\text{imc}})/w)]$. The curves show $\Phi(r)$ applied at two successive time steps; in the first time step (blue) $r_{\text{imc}} = 325$ nm, in the second $r_{\text{imc}} = 350$ nm. The characteristic width of the front shown here is $w = 100$ nm.

2.4.2 Elimination of grain boundaries

When a growing IMC particle impinges on a Sn-Sn grain boundary, the Sn adjacent to and within the grain boundary is transformed to IMC. To account for this elimination of grain boundaries within the transformed region, grain boundary diffusivity is scaled logarithmically with Φ via the relation, $D^*_{\text{gb}} = \epsilon^{\Phi} D_{\text{gb}}$, where D^*_{gb} is the scaled diffusivity and ϵ is finite constant chosen to be as small as possible without causing numerical problems in the solution. In the present case, $\epsilon = 2 \times 10^{-10}$. D^*_{gb} is scaled logarithmically with Φ rather than linearly in order to produce a significant reduction in the grain boundary diffusivity when $\Phi < 1$ while also keeping D_{gb} finite when $\Phi = 1$. Given the high value of D_{gb} for Sn relative to the rate of loading, a reduction of D_{gb} by at least 10^{-4} is necessary to noticeably impede grain boundary

transport within the model.

2.4.3 Specifying IMC Growth Rate

The IMC growth rate in the model is correlated with experimentally measured IMC growth rates via the following procedure. First, the total IMC volume in the model is expressed as a function of a single parameter, the IMC radius r_{imc}. This function, $V(r_{imc})$, depends on the assumed distribution of IMC nodules and accounts for both volumetric expansion associated with the transformation and impingement of the nodules as they grow. Using the inverse of this function, the model parameter r_{imc} is then determined as a function of time for a given experimentally-measured IMC growth curve, $V_{imc}(t)$. During each load step in the finite element model, r_{imc} specifies the current size of the IMC particles .

In the implementation, the radius of each IMC particle (as defined by the value of the field variable Φ) is increased by an increment, Δr, during each load step. To maintain the smooth propagation of the IMC growth front, Δr is set to a value less than the characteristic length scale of the elements in the mesh and is held constant for all load steps. The corresponding time increment for each simulation step is non-uniform and is determined by correlating the total IMC volume at the end of the step with the experimentally measured V(t) function. In a typical simulation the time increment for successive load steps becomes progressively larger, due to the slowing of the observed IMC growth rate and the increasing volume associated with each increment of IMC radius, Δr. The procedure for determining the time increment, Δt, associated with a given increment of IMC growth, Δr, is shown graphically in Figure 2.4.

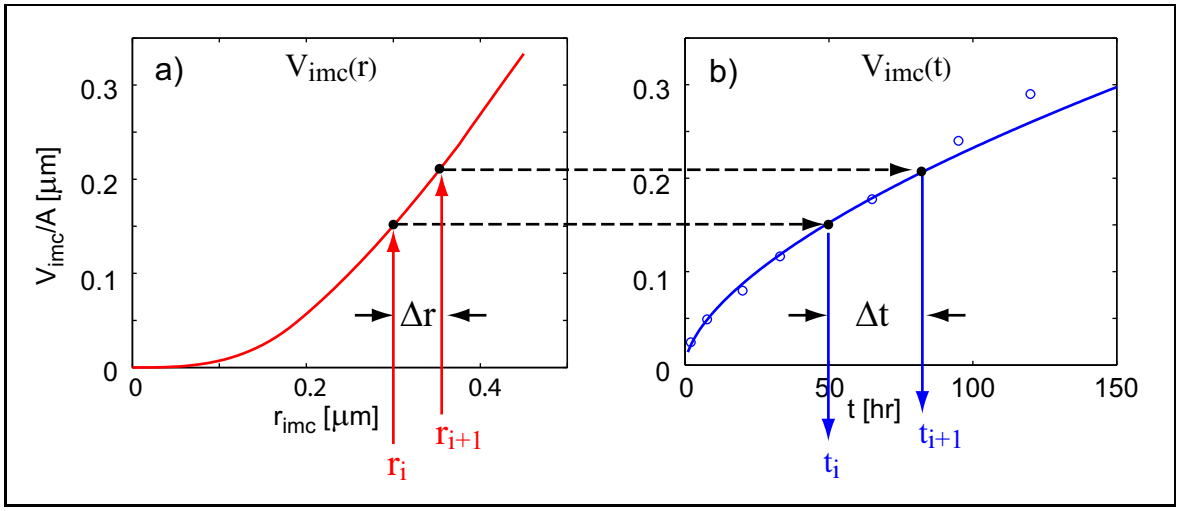

Figure 2.4: Graphical representation of the procedure for determining the time increment, Δt, for each finite element load step. During the load step, the IMC radius increases by a specified amount Δr from r_i to r_{i+1}. The corresponding IMC volumes are determined from the geometric relationship $V_{imc}(r)$ shown in graph (a). The time increment is then determined through the emperically-fit IMC growth function $V_{imc}(t)$ shown in graph (b). The symbols in (b) are experimental measurements.

2.5 Finite Element Implementation

All finite element calculations were performed using ABAQUS commercial finite element software. The Sn grains and the homogeneous Cu layer were meshed using eight-node linear hexahedral solid continuum elements with reduced integration and the interfaces separating Sn grains were meshed with user-defined twelve-node grain boundary elements. The grain boundary elements were implemented via a user subroutine written by Du (2009). Nodes associated with the solid elements have only displacement degrees of freedom, while nodes in the core of each grain boundary element have grain boundary stress components as degrees of freedom. Figure 2.5 shows an expanded view of a grain boundary element and the degrees of freedom associated with each node. Note that the grain boundary elements have zero thickness, so that the three nodes at each corner occupy the same position in space.

Symmetry boundary conditions are imposed on the spatial degrees for boundary

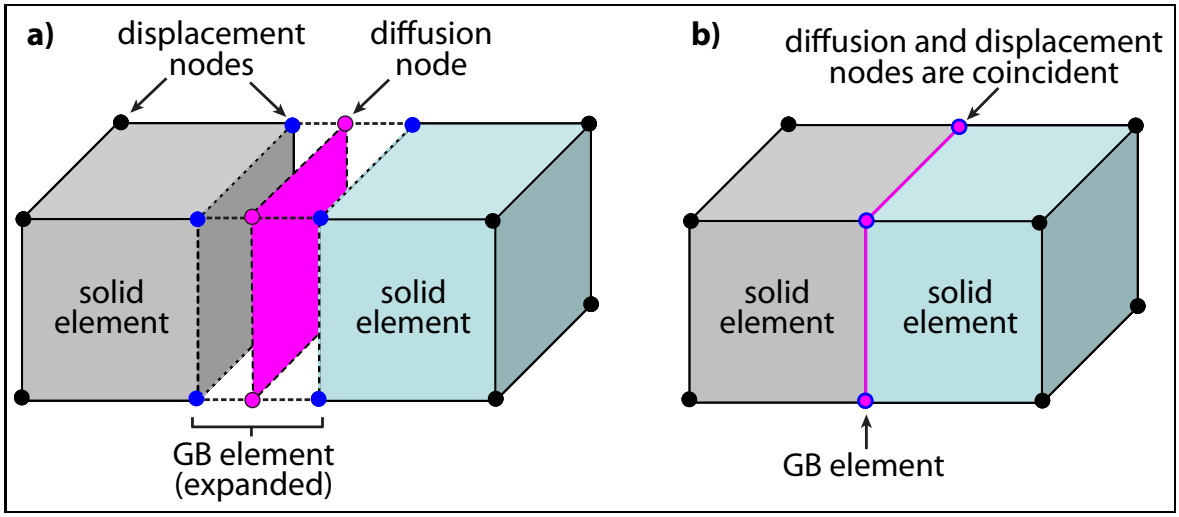

Figure 2.5: Schematic diagram showing nodes associated with the grain boundary diffusion elements. a) Expanded view showing node connectivity within the element. Blue and black nodes have displacement degrees of freedom; pink nodes have diffusion potential degrees of freedom (*i.e.* stress components normal and tangential to the plane of the grain boundary element). b) Node positions as they would appear in the finite element mesh. Note that the grain boundary diffusion element is planar with three coincident nodes at each corner.

nodes by specifying zero displacement normal to the plane of the boundary. When the model boundary coincides with a grain boundary, the properties of the grain boundary elements lying on the model boundary must also be modified to impose the symmetry condition. Zero displacement normal to the plane of the boundary is imposed on the displacement nodes lying on the boundary. In addition, the value of grain boundary diffusivity which is used to solve for the grain boundary normal stress within the elements must be set to half its assumed value. This effectively models one half of the grain boundary with a symmetry plane lying along its center.

Additional information regarding the choice of material parameters and the use of the finite element model are presented in the context of the following two chapters which address the mechanisms of stress generation and relaxation and the kinetics of whisker growth.

Chapter 3

Stress Evolution

3.1 Introduction

The importance of compressive stress in Sn films as a primary driving force for whisker growth is well established [Fisher *et al.* (1954), Galyon (2004)]. This stress can result from mechanical deformation during processing and handling of components, thermal mismatch or, in the case of Sn films on Cu, the spontaneous growth of intermetallic compounds (IMCs). The latter process is of particular concern as it is difficult to control and can continue over long periods of time. A fundamental understanding of the process of stress generation in Sn films could potentially provide insight into strategies to minimize stress and thereby mitigate whisker growth. However, there is no clear consensus regarding the mechanisms by which localized growth of IMC produces stress within the Sn film [Tu (1994, 1996), Lee and Lee (1998), Choi *et al.* (2003), Krishnamurthy and Srolovitz (2005), Tu and Li (2005), Boettinger *et al.* (2005), Galyon and Palmer (2005), Chason *et al.* (2008), Kumar *et al.* (2008)].

In order to understand how stress develops in response to IMC growth, it is necessary to identify the mechanical deformation processes operating in the surrounding

Sn film. Recent experimental work provides evidence of extensive dislocation activity within the Sn film, especially in the neighborhood of IMC grains [Kumar *et al.* (2008), Chason *et al.* (2008)], indicating that the Sn grains yield plastically. This conclusion is also consistent with reported stress measurements within the Sn layer which are very near the nominal yield stress for Sn (14.5 MPa [Gale and Totemeier (2004)]) and remain relatively constant over time [Lee and Lee (1998), Sheng *et al.* (2002), Boettinger *et al.* (2005), Chason *et al.* (2008)]. In addition, self-diffusion along the columnar grain boundary network has been shown experimentally to provide a fast pathway for long-range mass transport associated with stress development and whisker growth in Sn films [Reinbold *et al.* (2009)]. The role played by these plastic deformation processes in the development of stress within Sn films, however, has not been quantitatively assessed.

In this chapter, we present a series of finite element simulations that allow us to quantitatively evaluate different mechanisms for the generation of stress in Sn films due to growth of the Cu_6Sn_5 intermetallic compound at the Cu-Sn interface. Specifically, we examine the role of elastic and plastic deformation within Sn grains and the role of stress-driven diffusion of Sn along grain boundaries. It should be noted that the work presented here does not address the nucleation of whiskers, nor include the effect of local stress relaxation in the region surrounding a whisker. These issues are taken up in Chapter 4. Also, for the purpose of this study we limit attention to stress generation in as-deposited Sn films which exhibit a well-developed columnar microstructure, and do not consider the effect of solder reflow or post-deposition annealing which can significantly alter the micro-structure, thickness, and morphology of the Sn.

The simulations show that elastic deformation and dislocation-mediated plastic flow alone are not sufficient to reproduce the experimentally measured relationship

between stress and IMC volume. However, when grain boundary diffusion is included, the model results agree well with experimental observations. Examination of conditions necessary to produce the observed stresses provide insights into potential strategies for minimizing stress generation and thus mitigating whisker growth.

3.2 Experimental Background

The correlated measurements of IMC volume and stress were discussed in Section 1.2. Here, we briefly review those results, calling attention to several key features. Figure 3.1 shows measured IMC volume per area and the corresponding average stress in the Sn layer obtained from two sample series: 1.45 μm thick Sn and 2.9 μm thick Sn electro-plated over 0.6 μm of Cu. It is important to note that the measured stress represents mean biaxial stress (the average of the two in-plane normal stress components, $(\sigma_{11} + \sigma_{22})/2$) integrated over the thickness of the Sn layer.

Examining the plots of IMC growth over time (Figures 3.1a and 3.1b), IMC volume per area is seen to increase monotonically at a rate that decreases with time. For the thicker, coarser-grained film, the initial rate of IMC growth is faster and the slowing of the growth rate is more pronounced than for the thinner film. The IMC volume measurements also show a greater degree of scatter for the thicker film. The IMC volume as a fraction of the initial Sn volume (Figures 3.1c and 3.1d) is comparable for the two Sn thicknesses.

In both cases, the corresponding stress in the Sn, shown in Figures 3.1e and 3.1f, is initially tensile but quickly becomes compressive. The stress reaches a maximum compressive value after approximately 20 hours, then remains relatively constant even though IMC continues to grow. The observation that the average stress appears to attain a "steady state" value indicates that further IMC growth is accommodated by processes that produce little additional stress within the Sn, such as plastic yield.

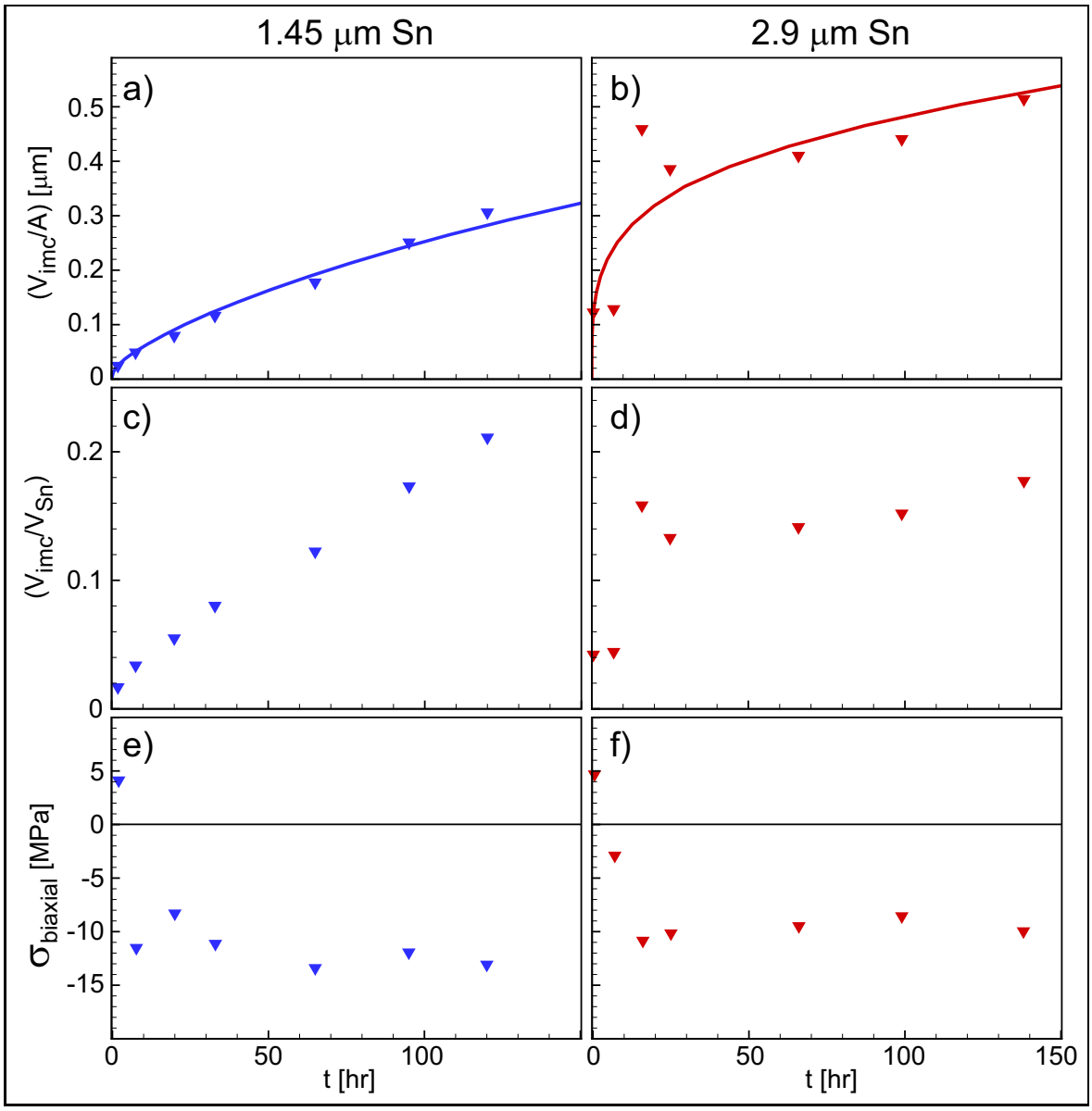

Figure 3.1: Experimental measurements of IMC volume per area (a and b) and mean biaxial stress in the Sn (e and f) for two film thicknesses. The IMC volume per area is normalized by the film thickness to give IMC volume as a fraction of initial Sn volume in c) and d). Data from samples with 1.45 μm Sn electroplated on 0.6 μm Cu are shown in a), c) and e) and data from samples with 2.9 μm Sn electroplated on 0.6 μm Cu are shown in b), d) and f). The empirically fit curves (solid lines) in a) and b) were used to model IMC growth in the numerical simulations. The growth curve for the 1.45 μm Sn has the form $V_{imc}/A = (0.014\ \mu\text{m}\cdot\text{hr}^{-0.6})t^{0.6}$ and that for 2.9 μm Sn has the form $V_{imc}/A = (0.135\ \mu\text{m}\cdot\text{hr}^{-0.25})t^{0.25}$. Data were previously published by Chason *et al.* (2008) and Jadhav *et al.* (2010).

To understand how stress is generated by IMC growth, it is necessary to consider the nature of the IMC transformation reaction. At room temperature, Cu and Sn react irreversibly to form the Cu_6Sn_5 IMC. Scanning electron microscopy (SEM) and transmission electron microscopy (TEM) analyses reveal that IMC particles nucleate within the Sn at the Cu-Sn interface, typically with greater probability at the triple junctions where grain boundaries between Sn grains meet the Cu interface [Chason *et al.* (2008), Kumar *et al.* (2008), Zhang *et al.* (2005)]. After nucleation, growth of the particles proceeds at the IMC-Sn interface [Tu and Thompson (1982), Tu (1994)], with IMC particles primarily growing up into the Sn film [Chason *et al.* (2008), Kumar *et al.* (2008), Zhang *et al.* (2005), Sheng *et al.* (2002)]. TEM analysis also provides evidence of dislocation activity within the Sn layer, particularly near IMC particles [Chason *et al.* (2008), Kumar *et al.* (2008)]. This suggests that IMC growth induces sufficient stress within the surrounding Sn grains to cause dislocation-mediated plastic deformation.

In the case of pure Sn on Cu, SEM and TEM examination of cross-sections through the thickness of the film show that IMC growth occurs primarily at the Sn-Cu interface [Chason *et al.* (2008), Kumar *et al.* (2008)]. There is little evidence of isolated IMC particles away from the Sn-Cu interface, either within Sn-Sn grain boundaries or in the Sn grains themselves. Thus, a model for stress generation must explain how IMC growth that is restricted to the base of the Sn layer results in the development of stress throughout the thickness of the film.

Stress generation in the Sn layer is intimately related to the volume changes associated with the formation of Cu-Sn intermetallic compounds. Here we consider only reaction of Cu and Sn to form Cu_6Sn_5, since this is the sole IMC phase observed at room temperature [Tu (1994)]. As discussed above, Cu_6Sn_5 is observed to grow into the Sn. This requires the transport of Cu to the IMC growth front, where it

Species	Density	Molar Volume
Cu	8.96 g/cm^3	7.09 cm^3/mol
Sn	7.30 g/cm^3	16.3 cm^3/mol
Cu_6Sn_5	8.28 g/cm^3	10.7 cm^3/mol

Table 3.1: Density and molar volume data. Note that the molar volume of Cu_6Sn_5 corresponds to 1 mole of atoms and is based on the composition of $5/11(= 0.45)$ atomic fraction Sn.

then reacts with the adjacent Sn [Tu and Thompson (1982), Tu (1994)]. The net volume change associated with the reaction is therefore partitioned into two spatially separated volume changes: volume loss within the Cu layer and volume increase within the Sn layer. Calculation of the resulting strain within the Sn layer depends on the details of the transformation from Sn to IMC. While these details are not well understood, the consequences of two limiting cases can be explored.

Consider a fixed volume of Sn adjacent to a growing IMC particle. If all of the Sn atoms in this region rearrange to form Cu_6Sn_5 as Cu atoms arrive, then the region will undergo a large volumetric expansion. Referring to the molar volume data summarized in Table 3.1, the initial Sn volume of $(0.45)V_{\mathrm{m}}^{\mathrm{Sn}} = 7.4$ cm^3/mol is replaced by $V_{\mathrm{m}}^{\mathrm{IMC}} = 10.7$ cm^3/mol, corresponding to a 45% volume increase. This value is an upper bound, since some of the IMC volume may also be accommodated by motion of the Cu-Sn interface.

At the other extreme, it is possible for the IMC to occupy the same volume as the Sn it replaces if sufficient Sn is expelled as point defects during the transformation. The expelled Sn could either be accommodated by the surrounding Sn lattice or adjacent grain boundaries. Stress generated by the diffusion of expelled Sn along grain boundaries will be discussed in the results section. For the case of Sn point defects inserted into the surrounding Sn lattice, the extremely low bulk self-diffusivity for Sn ($D \approx O(10^{-18}$ cm^2/s)) [Gale and Totemeier (2004)] would effectively limit the volumetric expansion to a region immediately surrounding the IMC particles. The

resulting localized expansion would be very similar to that produced by expansion of the IMC itself. For the purpose of modeling stress evolution in the Sn film, we assume that the transformation of Sn to Cu_6Sn_5 produces a localized volumetric expansion of 45%. The effect of volume loss within the Cu substrate is not considered here. Since the Cu film is constrained against lateral deformation by the underlying Si wafer, stress in the Cu layer has little influence on the stress in the Sn.

3.3 Simulation Details

Our finite element simulations model a polycrystalline Sn film with columnar grain structure bonded to a Cu substrate, as shown in Figure 3.2. The copper substrate is treated as a homogeneous solid layer while the Sn film consists of a periodic array of identical hexagonal grains. The Sn grains are separated by vertically-oriented grain boundaries which support stress-driven mass transport. We assume that flux of material out of the grain boundaries onto the free surface is prevented by the presence of a passivating oxide layer. Mechanical behavior of the oxide layer, however, is not included in the model. Symmetry boundary conditions are applied at the lateral boundaries of the model cell to effectively model an infinite film, and the base of the model cell is held fixed. All dimensions and parameters used in the simulations are listed in Table 3.2.

The Sn grains and the Cu layer are treated as isotropic, elastic-plastic solids with Young's modulus E_α, Poisson's ratio ν_α (where α is either Sn or Cu). Plastic deformation in the Cu is assumed to be rate-independent with yield stress, Y_{Cu}. In the Sn layer, both rate-independent plastic yield and rate-dependent viscoplastic constitutive behaviors are considered. The isotropic von Mises yield criterion (second stress invariant, J_2) is applied in the rate-independent cases, while an isotropic power-law

Quantity	**Symbol**	**Value**		**Ref.**
Sn film thickness	h_{Sn}	1.45 and 2.9	μm	
Length of hexagonal grain edge	L	0.75 and 1.0	μm	
Cu film thickness	h_{Cu}	0.6	μm	
Elastic modulus of Sn	E_{Sn}	50	GPa	(1)
Poissons ratio of Sn	ν_{Sn}	0.36		(1)
Yield strength of Sn	Y_{Sn}	14.5	MPa	(1)
Elastic modulus of Cu	E_{Cu}	117	GPa	(1)
Poissons ratio of Cu	ν_{Cu}	0.34		(1)
Yield strength of Cu	Y_{Cu}	200	MPa	(2)
Elastic modulus of Cu_6Sn_5	E_{imc}	86	GPa	(3)
Poissons ratio of Cu_6Sn_5	ν_{imc}	0.30		(3)
Yield strength of Cu_6Sn_5 *	Y_{imc}	2000	MPa	(4)
Grain boundary diffusivity of Sn	D_{gb}	4.8×10^{-9}	cm^2/s	(5)
Grain boundary width of Sn	δ	0.5	nm	(5)
Atomic volume of Sn	Ω	0.027	nm^3	
Temperature	T	298	K	

Table 3.2: Parameters used in the simulations. References: (1) Gale and Totemeier (2004); (2) Freund and Suresh (2003); (3) Fields *et al.* (n.d.); (4) Deng *et al.* (2004); (5) Lange and Bergner (1962). *Note: Cu_6Sn_5 is not expected to deform plastically, but a yield strength is required in the model to allow transformation of Sn to IMC. Y_{imc} is given a very large value consistent with experimental measurements.

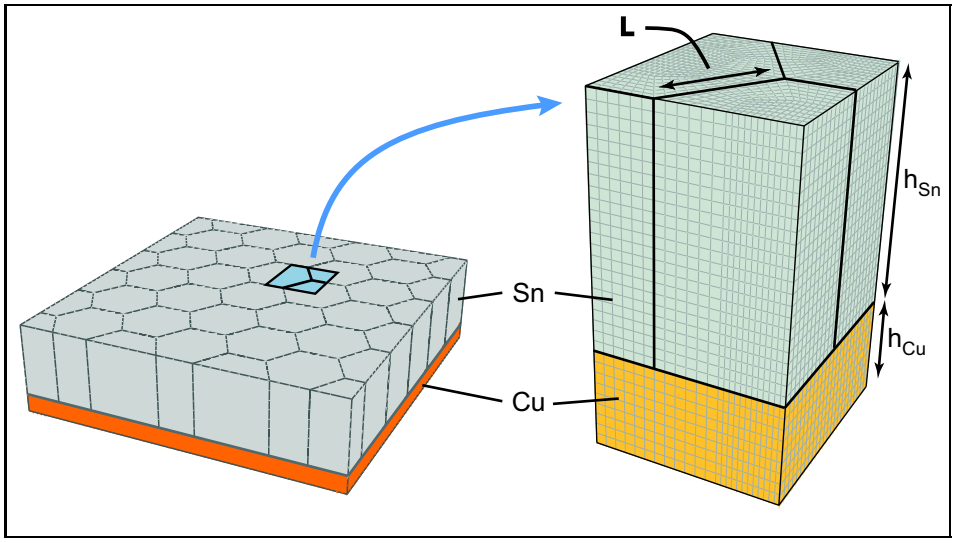

Figure 3.2: The computational model used in the finite element simulations. The diagram on the left shows the Cu-Sn bilayer film represented by the model. The Sn layer is comprised of columnar hexagonal grains separated by vertically oriented grain boundaries which can act as fast diffusion pathways. The highlighted region shows the outline of the actual model cell which is shown in greater detail on the right. By applying symmetry boundary conditions on the lateral boundaries, the model cell simulates a perfectly regular film of infinite extent.

model ($\dot{\varepsilon}_p = A\left(\frac{\sigma}{\sigma_0}\right)^m$ where σ_0 is a characteristic stress and A and m are empirically fit parameters) is assumed for rate-dependent plasticity. While we recognize that the constitutive behavior of Sn is significantly more complex (exhibiting strong anisotropy in elastic and plastic deformation) the simplified behavior modeled here is sufficient to establish the mechanisms by which stress develops and is transmitted through the Sn film.

Stress is generated in our model by the growth of hemispherical IMC nodules up into the Sn from the Cu-Sn interface (see Figure 3.3). These nodules grow radially into the Sn layer by the progressive transformation of adjacent Sn into IMC. In the simulations, the radius of the IMC nodules, r_{imc}, is increased incrementally over a series of time steps, at a rate specified to correspond to the experimentally measured IMC growth curve (see Figure 3.1). During each time step, a thin shell of Sn (~25 nm

thick) surrounding the existing IMC nodules is transformed to IMC, simultaneously increasing the volume of IMC while consuming some of the Sn.

The molar volume change associated with the transformation is modeled by applying a stress-free transformation strain corresponding to a 45% volumetric expansion. After application of the transformation strain, the material is in a state of compressive stress and would have to undergo a 45% expansion to become stress-free. The transformation process is assumed to occur quasi-statically, and stress equilibrium is maintained throughout the simulation. Details of the finite element implementation of the IMC transformation reaction are presented Section 2.4.

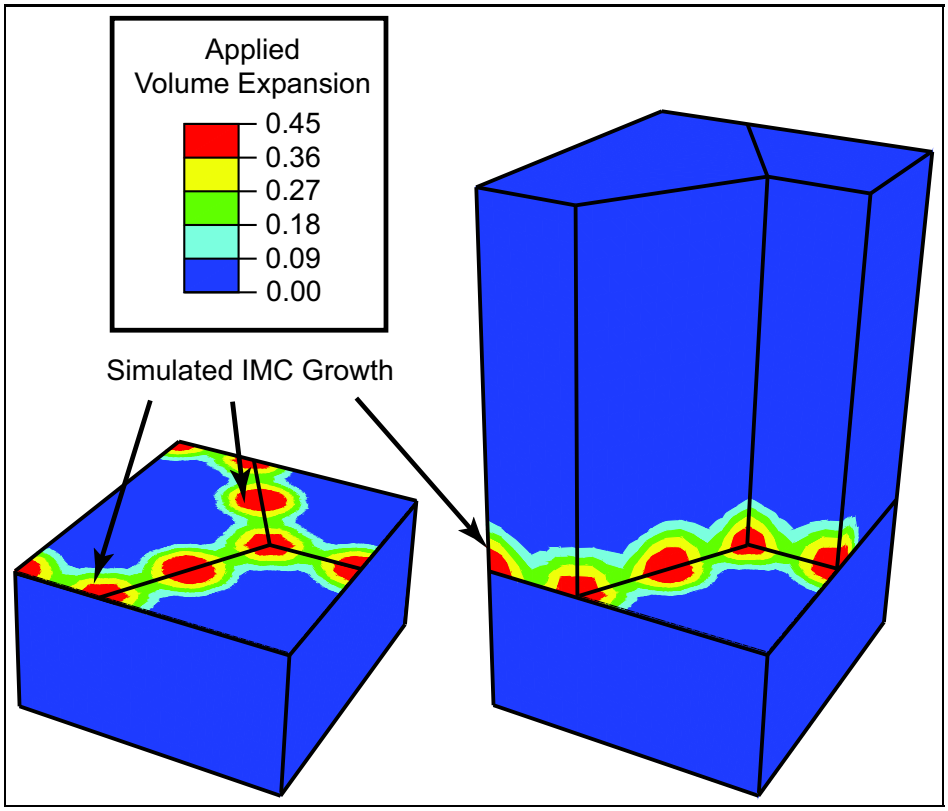

Figure 3.3: IMC growth is simulated by applying a volumetric expansion to hemispherical regions distributed along the Sn-Sn grain boundaries at the base of the Sn layer. The radius of the expanded regions is increased incrementally to model the progressive growth of the IMC. In the images shown, the corresponding IMC volume/area is 0.1 μm.

Finite element simulations are used to calculate the three-dimensional stress and strain fields that develop and evolve over time. From these fields average or integrated quantities must be extracted for quantitative comparison with experimental measurements. For each simulation, mean biaxial stress through the entire Sn layer is computed as a volume weighted average of $(\sigma_{11} + \sigma_{22})/2$ taken over all unexpanded elements. This corresponds to the stress measured experimentally in the Sn via the wafer curvature technique described by Chason *et al.* (2008). In addition, we compute stress profiles through the Sn film along two vertical transects: one directly above a growing IMC nodule at a Sn-Sn-Sn triple junction, the other located at the center of a Sn grain. At each of 22 vertical positions through the film, stresses are averaged over all elements within a 0.15 μm radius of the respective transect lines.

3.4 Results and Discussion

In the following discussion, we examine the consequences of five different combinations of constitutive behaviors. For completeness, we first consider purely elastic deformation within Sn grains, as has been proposed by several authors [Lee and Lee (1998), Krishnamurthy and Srolovitz (2005)]. However, as discussed in Section 3.2, there is strong experimental evidence of strain accommodation by dislocation-mediated plasticity and mass transport by stress-driven grain boundary diffusion, as well. The primary goal of this chapter is to explore how these processes control stress evolution within the Sn film and determine which combination of assumptions regarding constitutive behavior best explains the experimental stress measurements. To this end, we have run simulations with the following four combinations of constitutive behavior: plastic flow within Sn grains, with and without grain boundary diffusion, and power-law viscoplastic behavior within Sn grains, with and without grain boundary diffusion. Linear elastic behavior is also assumed in all cases.

This section is organized as follows. First the results of the purely elastic and elastic-plastic yield cases are presented. Understanding of the fundamental micro-mechanical response of the film to IMC growth is developed through detailed discussion of these results. Many of the core conclusions regarding the role of grain boundary diffusion follow from this discussion. The effect of rate-dependent creep behavior is then examined in relation to the results for rate-independent plasticity. Finally the sensitivity of the model to film thickness and grain boundary diffusivity are explored.

3.4.1 Elastic and Rate-Independent Plastic Behavior

Contour plots of the mean biaxial stress, as well as stress profiles along vertical transects, resulting from different choices of constitutive behavior are presented in Figure 3.4 for a model with 1.45 μm thick Sn. The corresponding history of average Sn stress over time is plotted for each case in Figure 3.5. We examine the meaning of the results for each case below.

We first consider the case of purely elastic behavior. The development of stress over time, shown in Figure 3.5a, appears to mirror the growth of IMC (curve in Figure 3.1). The average stresses calculated in this case are an order of magnitude more compressive than those measured experimentally. Closer examination of the stress field in Figures 3.4a and 3.4d reveals stresses of over one thousand MPa immediately surrounding the IMC nodules. However, the stress field diminishes rapidly with distance from the IMC and regions of both compressive and tensile in-plane stress are observed in the overlying Sn. Within the upper 1/3 of the Sn layer, the magnitude of the elastic stresses is only on the order of a few MPa. Thus, if the Sn were capable of supporting stresses in excess of 1 GPa, a purely elastic mechanism for transmitting stress would result in little compressive stress distributed through the thickness of

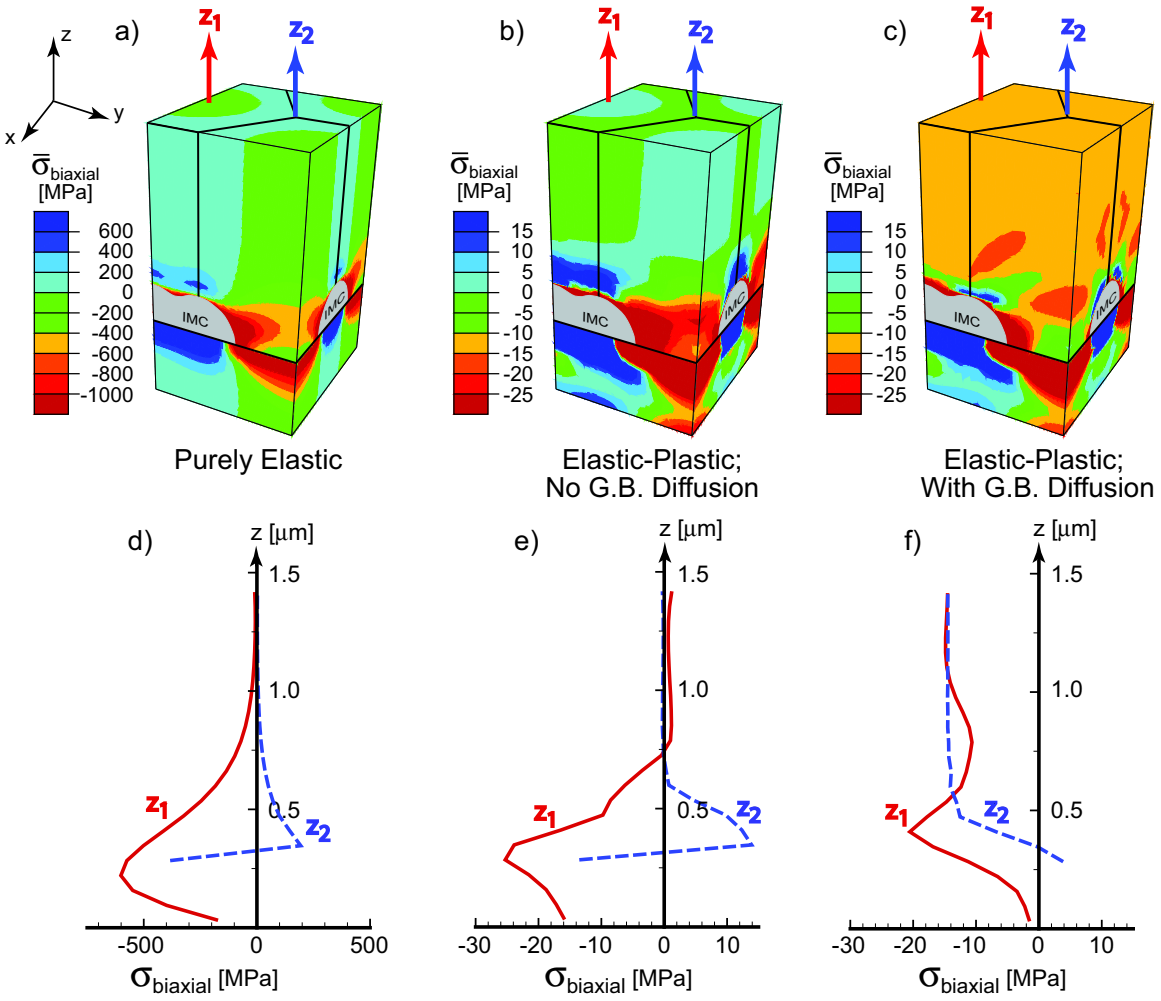

Figure 3.4: Contours of mean biaxial stress through the film (a-c) with stress profiles plotted for the same cases (d-e). Arrows labeled z_1 and z_2 on the contour plots indicate location of the vertical transects used to generate the stress profiles. Note that only the case including grain boundary diffusion (c) produces significant compressive stress (orange and red contours) through the Sn layer. In all cases, $t = 40$ hr corresponding to total $V_{\text{imc}}/A = 0.13$ μm.

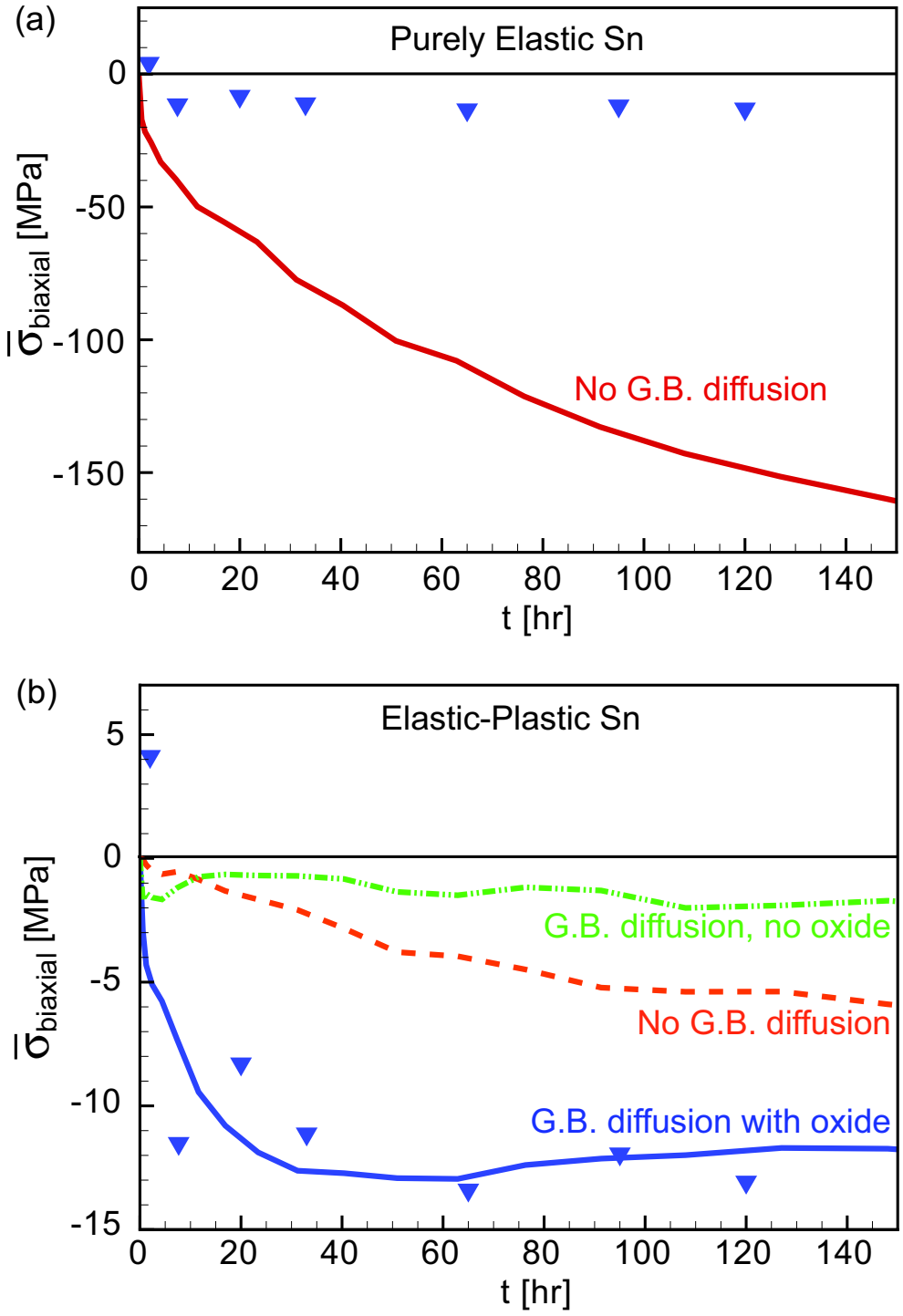

Figure 3.5: Mean biaxial stress averaged over the untransformed Sn. Symbols (∇) are experimentally measured values; lines are simulation results. Results for the purely elastic case (a) are shown separately from elastic-plastic cases (b), as the stress levels differ by an order of magnitude.

the film.

We next consider the case of elastic-plastic yield behavior within the Sn layer, but with no grain boundary diffusion. Although there is experimental evidence for the operation of both dislocation glide and grain boundary diffusion, it is useful decouple these processes to better understand the role each plays. When grain boundary diffusion is not included in the simulation, a plastically deformed zone ($\sigma_{\text{mises}} \geq$ 14.5 MPa in Figure 3.6a) develops at the base of the Sn layer, around the growing IMC particles. Yield within the Sn allows the expansion of the IMC to be accommodated without generating the large stresses seen in the elastic case. Beyond the plastically deformed region, however, the stress field is elastic and therefore diminishes rapidly with distance from the IMC, as seen in Figure 3.4b. In addition, regions of both compressive and tensile biaxial stress are observed in the Sn overlying the plastic zone.

As shown in Figure 3.5b, the biaxial stress becomes steadily more compressive with continued IMC growth, reaching a value of -6 MPa after 150 hours. The gradual increase in compressive stress averaged through the Sn reflects the increasing fraction of the Sn layer that is at its yield stress. In contrast, the experimentally observed stress in the Sn reaches a maximum compressive value of 10 to 12 MPa within the first 20 hours, then remains relatively constant.

Thus, while there is experimental evidence of dislocation-mediated plastic deformation within Sn grains [Kumar *et al.* (2008)], modeling indicates that elastic-plastic behavior alone is insufficient to explain the observed stress stress evolution associated with IMC growth. As in the case of purely elastic behavior, significant stresses develop in the immediate neighborhood of the IMC nodules, but die out very rapidly upward through the thickness of the film. As a result, very little compressive stress is transmitted through the thickness of the film – near the surface of the film, both

tensile and compressive biaxial stresses are generated with magnitudes of less than 1 MPa.

We now examine the stress that develops when IMC growth can be accommodated by mass transport through the Sn film via stress-driven grain boundary diffusion, in addition to elastic and plastic behavior within the Sn grains. In this case, the average biaxial stress in the Sn quickly reaches a maximum compressive value, then remains relatively constant as IMC growth continues (Figure 3.5b). This results from the redistribution of volume along grain boundaries. Where compressive stresses normal to the grain boundaries are largest, in and around the plastic zone, Sn is removed from the adjacent grains and transported to less compressive regions of the grain boundary. Since the stress gradients are largely normal to the plane of the film, this results in net transport of volume from the base of the film toward the surface. As shown in Figures 3.4c and 3.4f, the redistribution of volume via grain boundary diffusion produces relatively uniform compressive stress through the thickness of the Sn layer.

The transport of Sn along grain boundaries also affects the extent of the plastic deformation zone within the Sn grains. Contours of von Mises equivalent stress (Figure 3.6a) show that in the absence of grain boundary diffusion the plastic zone ($\sigma_{\text{mises}} \geq 14.5$ MPa) is restricted to a narrow band at the base of the film, immediately surrounding the IMC particles. However, when grain boundary diffusion is active (Figure 3.6b) the majority of the film is at or near the nominal yield stress.

This mechanism for stress transmission helps explain why the measured stress in the Sn reaches a steady state value which is relatively insensitive to further IMC growth. Only a small volume of IMC growth is required to drive sufficient transport of Sn upward through the film along grain boundaries and produce a relatively uniform stress state through the thickness of the film. After the stress in the Sn reaches the

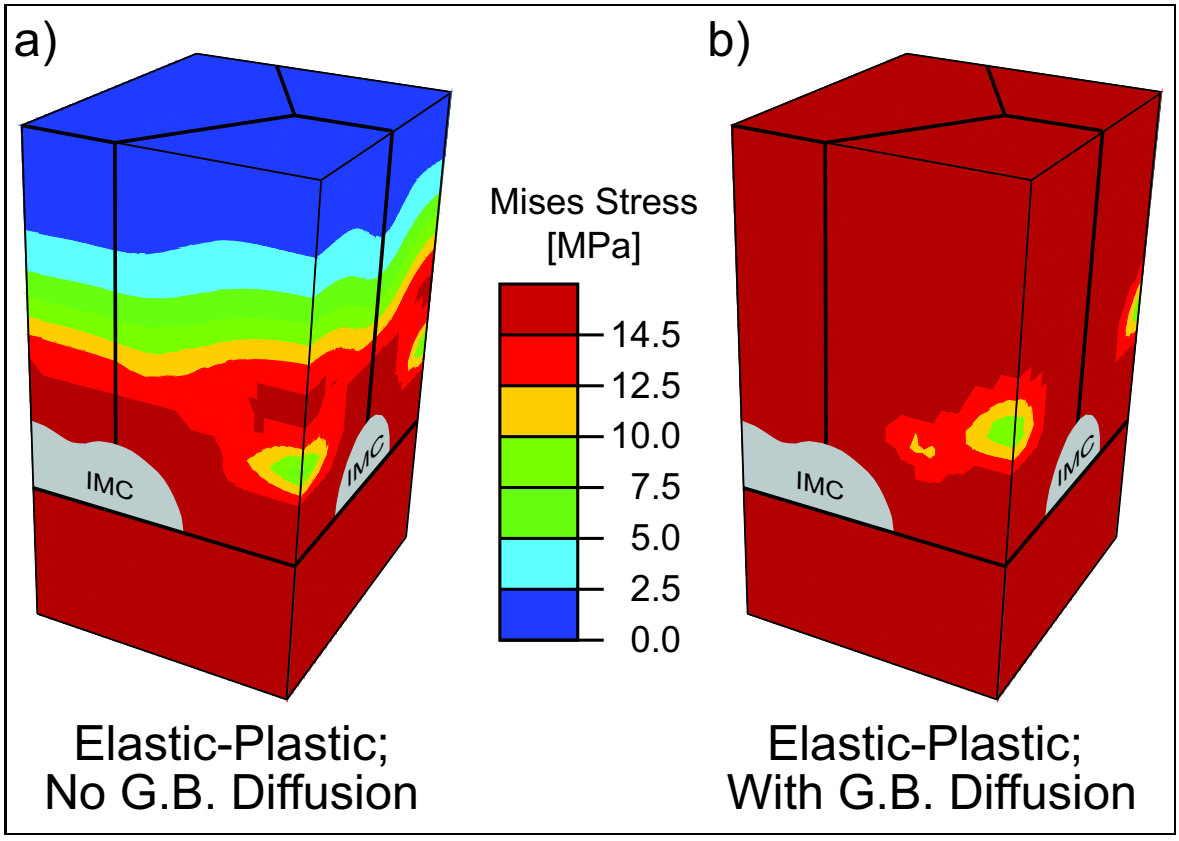

Figure 3.6: Contours of von Mises equivalent stress for simulations a) without and b) with diffusion along grain boundaries. In both cases, elastic-plastic constitutive behavior is assumed within the Sn grains. Without grain boundary diffusion (a), plastic yield ($\sigma_{\text{mises}} \geq 14.5$ MPa) is restricted to a band near the base of the film. However, when material can be transported via grain boundary diffusion (b) the plastically deforming region extends farther into the Sn and the entire film is near yield. t =40 hr and total $V_{\text{imc}}/A = 0.13$ μm in both cases shown.

yield strength, additional IMC growth has little effect.

In our simulations, we assume that the transformation of Sn to IMC is accompanied by local volume expansion. As discussed in the experimental background section, another possibility is that Sn could be expelled to the grain boundaries during the reaction with little or no volume change in the transformed region. To evaluate this case, we consider the amount of volume that would have to be added

to the grain boundaries to produce the experimentally observed stress. A biaxial strain of 2×10^{-4} is sufficient to bring the Sn to its nominal yield stress of 14.5 MPa ($\varepsilon = (1 - \nu_{\mathrm{Sn}})Y_{\mathrm{Sn}}/E_{\mathrm{Sn}} \approx 2 \times 10^{-4}$). For a columnar film with grain size $\phi = 1.4$ μm, this corresponds to a thickening of the grain boundaries by an amount, $\Delta\delta = \varepsilon\phi \approx 0.28$ nm, roughly equivalent to the addition of a monolayer of Sn atoms. Given the exceedingly small volume of excess Sn that would be required in the grain boundaries to produce uniform compressive stress in the Sn, we conclude that IMC transformation involving Sn expulsion rather than (or in addition to) direct expansion is also a plausible mechanism for stress generation. Regardless of the details of the IMC transformation reaction, our primary conclusion, that grain boundary diffusion plays a central role in the development of stress within the film, remains unchanged.

The grain boundary diffusion mechanism for stress transmission that we have just demonstrated depends critically on two features of the Sn film: 1) columnar microstructure, and 2) the presence of a passivating oxide layer. Both are necessary to prevent relaxation of the stress — and therefore, their disruption may provide strategies for minimizing stress development within the Sn film.

The columnar microstructure of Sn films, with very few grain boundaries oriented parallel or at low angle to the plane of the film, prevents stress relaxation via Coble creep. To summarize the argument given by Boettinger *et al.* (2005), grain boundaries parallel to the traction-free surface of the Sn would be subject to very small normal stress and thus have a lower diffusion potential relative to vertically-oriented grain boundaries. This would drive mass transport from vertical to horizontal grain boundaries, resulting in reduced in-plane biaxial compression and slight overall thickening of the film.

The passivating oxide plays a similar constraining role. Without the oxide, diffusion of Sn out of the grain boundaries and onto the free surface of the Sn would be

possible. Mass could be removed from grain boundaries with high compressive normal stress and transported to the traction-free surface of the Sn where the diffusion potential is much lower. Experimentally, in-situ film stress measurements change by an amount consistent with the relaxation of compressive stress within the Sn layer when the surface oxide is removed by etching [Chason *et al.* (2008)]. To demonstrate the effect of the oxide in our FEM simulation, we eliminated the zero flux condition at the top of the grain boundaries which allows diffusion of material out onto the surface of the Sn. As seen in Figures 3.5b and 3.7, removal of the surface oxide results in nearly complete relaxation of stress in the Sn, except in the immediate vicinity of the IMC.

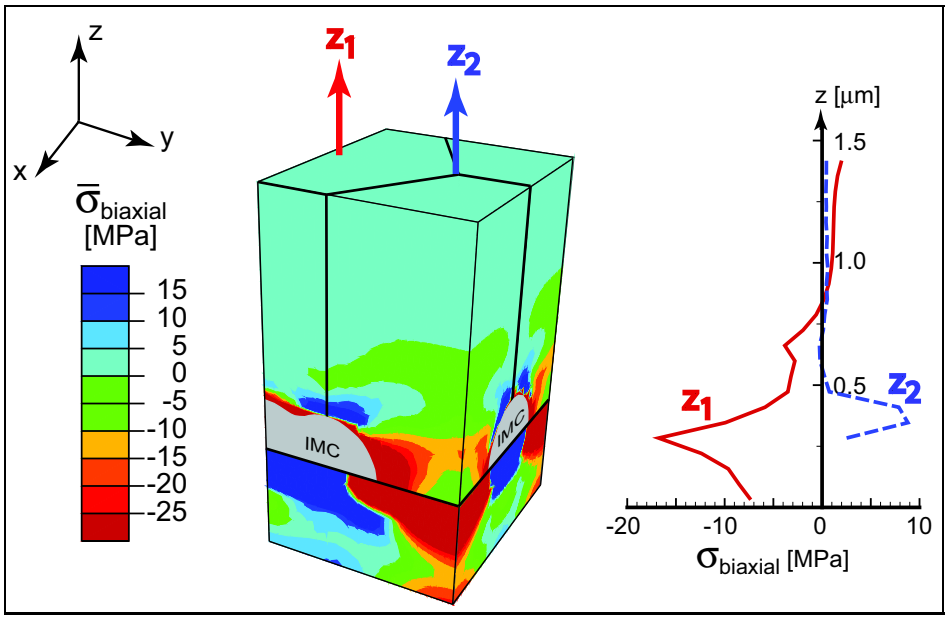

Figure 3.7: When material is allowed to diffuse out of grain boundaries and across the free surface of the Sn, as would be the case if there were no passivating oxide layer present, IMC growth produces little stress through the thickness of the Sn. a) Contours of mean biaxial stress at t =40 hr, corresponding to total $V_{\text{imc}}/A = 0.13$ μm. b) Stress profiles along vertical transects (marked by arrows z_1 and z_2) through the Sn layer.

3.4.2 *Effect of Rate-Dependent Plastic Deformation*

Sn is known to exhibit rate-dependent plasticity, or creep behavior, at room temperature and we now consider how this might affect the development of stress within the film. Shin and Chason (2009) have measured the creep response of Sn films with thickness and microstructure similar to those of the samples used for the correlated measurement of IMC volume and stress shown in Figure 3.1. In their experiments, stress was generated by thermal expansion mismatch between the Sn film and the substrate over temperatures ranging from 297 K to 337K. The resulting stress-time data were used to obtain parameter values for the following power-law creep constitutive equation:

$$\dot{\varepsilon}_p = A\frac{\mu}{T}\exp\left(\frac{-Q}{kT}\right)\left(\frac{\sigma_e}{\mu}\right)^n \tag{3.1}$$

where $\dot{\varepsilon}_p$ is the plastic strain rate, Q is the activation energy for dislocation motion, k is Boltzmann's constant, T is absolute temperature, σ_e is the von Mises equivalent stress and μ is the shear modulus. n and A are empirically-determined material parameters. The values of n and Q determined by Shin and Chason (2009) for two different thickness films are summarized in Table 3.3. Their measured stress exponent values range from 1.9 to 4.6. Other reported values of n for room temperature Sn range from 2 to 9, with the majority between 4 and 6 [McCabe and Fine (2002), Kerr and Chawla (2004), Mathew *et al.* (2005), Chen and Dutta (2008)].

The creep exponent of approximately 2 found by Shin and Chason (2009) for room temperature relaxation of the thinnest film is consistent with a mechanism dominated by grain boundary and surface diffusion [Frost and Ashby (1982)], and therefore probably does not reflect plastic deformation within Sn grains. The majority of their experiments, however, are fit by creep exponents in the range $n = 4.1$ to $n = 4.6$, which is consistent with a diffusion-controlled dislocation climb and glide mechanism within the Sn grains [Frost and Ashby (1982), Shin and Chason (2009)]. It should

	n			
	1.4 μm Sn		8 μm Sn	
ΔT [°C]	T_{max} Q=(70.6 kJ/mol)	Room T (105 kJ/mol)	T_{max} (61.4 kJ/mol)	Room T (61.4 kJ/mol)
15	4.1	1.9	–	–
20	4.2	2.0	4.4	4.3
25	4.3	2.0	–	–
30	4.4	2.0	4.5	4.4
35	4.5	2.1	–	–
40	4.6	2.1	4.6	4.5

Table 3.3: Values of stress exponent n obtained by Shin and Chason (2009). Stress-time data were fit to Equation 3.1, with $A = 1.6 \times 10^{15}$ K/(MPa·s) and $\mu = 16,302$ MPa$-(40.5$ MPa/K$)T$. Values presented in the original paper have been rounded to the first decimal place.

also be noted that higher creep exponents were measured for films subjected to higher stresses. This may indicate the onset of "power-law breakdown", at which point the strain rate increases exponentially with stress. According to Frost and Ashby (1982) power-law behavior is expected to breakdown at $T > 0.6T_{melt}$ and $\sigma_e > 10^{-3}\mu$ where μ is the shear modulus. For Sn, this places the upper limit for the validity of power-law behavior at room temperature and stresses in the neighborhood of 15 MPa.

To assess the effect of rate dependent plasticity on stress evolution, the finite element model described in Sections 3.3 and 3.4.1 has been modified so that plastic deformation within Sn grains is governed by power-law creep (Equation 3.1) rather than plastic yield. All other aspects of the model are as previously described. The development of mean biaxial stress within the Sn layer in response to IMC growth is shown in Figure 3.8 for the combinations of material parameters reported by Shin and Chason (2009) (see Table 3.3). Examining the calculated stress histories, the best fit to the experimental measurements is found for power-law creep parameters $Q = 70.6$ kJ/mol and $4.4 < n < 4.6$.

A number of differences are apparent in the stress evolution curves presented

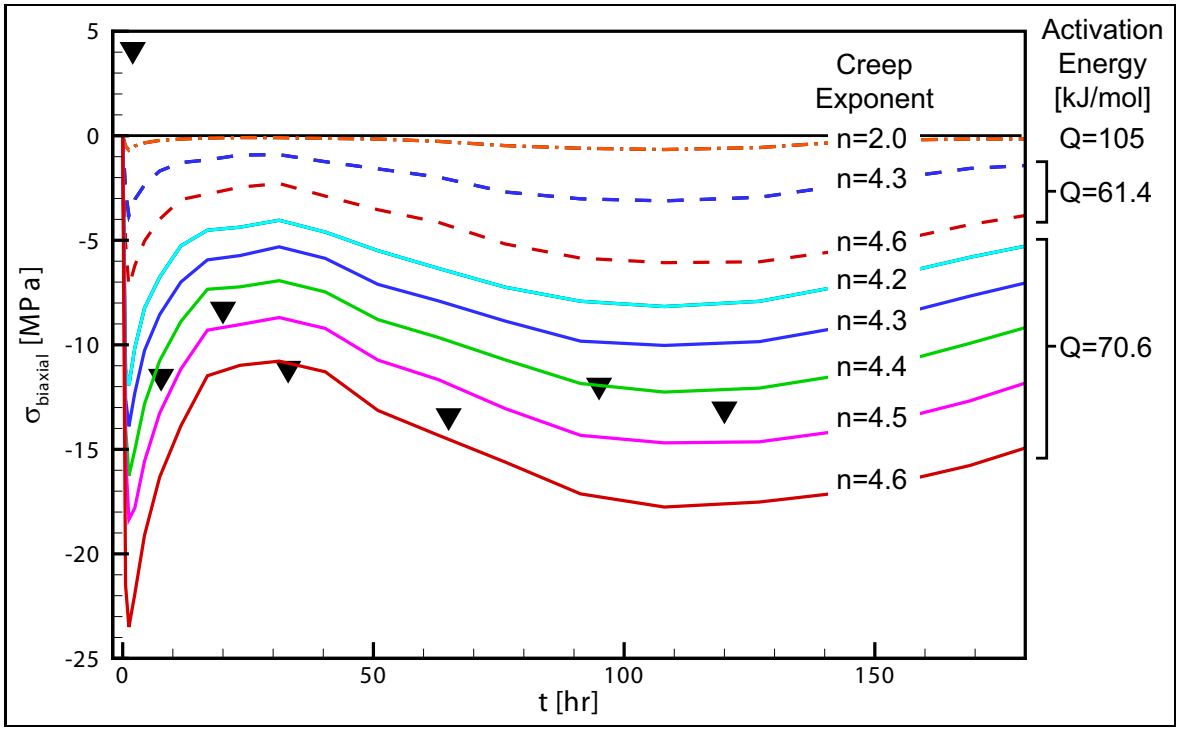

Figure 3.8: Calculated stress evolution assuming power law creep behavior within Sn grains and stress-driven diffusion along grain boundaries. Values for creep exponent, n, and activation energy, Q, are from Shin and Chason (2009). Symbols (∇) are experimentally measured stress values. In all cases the Sn thickness is 1.45 μm with grain size 1.4 μm (L=0.75 μm) and the IMC growth is modeled as $V_{imc}/A = (0.014\ \mu\text{m}\cdot\text{hr}^{-0.6})t^{0.6}$.

in Figure 3.8 relative to those seen previously for Sn modeled by rate-independent plastic yield. The primary conclusion of the previous section, however, that grain boundary diffusion acts as a mechanism for transmitting stress through the thickness of the Sn, remains the same. This can be clearly seen in Figure 3.9 which shows the calculated mean biaxial stress for two models with viscoplastic Sn behavior: one with grain boundary diffusion, the other without. In the model that includes grain boundary diffusion, the mean biaxial stress in the Sn rapidly becomes compressive and remains compressive throughout the simulation (the more complex variations in the stress are discussed in detail below). Without grain boundary diffusion, the mean stress through the Sn layer is initially tensile, only becoming compressive during the

later stages of the simulation. Thus it would appear that grain boundary diffusion plays a key role in the build-up of compressive stress within the Sn.

The details of the stress history are somewhat more complicated and deserve closer examination. To aid interpretation of the mean stress evolution, the variation in biaxial stress along vertical transects through the thickness of the film are plotted in the insets to Figure 3.9 at four different times. First consider the case of viscoplastic Sn *without* grain boundary diffusion. The stress profiles plotted in Figures 3.9a) through d) show that the development of stress is limited to the neighborhood of the IMC particles near the base of the film. The upper half of the Sn film remains nearly stress-free. The overall tensile character of the average stress through the film results from the contribution of the large tensile stress that develops near the base of the Sn, in the region between IMC particles (solid red lines in stress profiles). As the IMC particles grow, the volume of the region under tension decreases and eventually the stress becomes compressive throughout (Figure 3.9d).

When grain boundary diffusion is included in the model, a sharp spike in compressive stress is observed at the outset of the model calculations. The compressive stress reaches its peak value after approximately one hour, then relaxes to half this maximum magnitude within 24 hours. This is followed by a more gradual increase in compressive stress and subsequent relaxation toward zero after about 100 hours. This complicated stress history results from the combined effects of the high initial IMC growth rate imposed in the simulations, stress-driven grain boundary diffusion, and the elastic-viscoplastic rheology of the Sn grains.

As in the plastic yield cases examined in Section 3.4.1, stress-driven grain boundary diffusion rapidly redistributes excess volume generated by the expansion of the IMC through the thickness of the Sn film, which is initially stress-free. Due to the viscoplastic behavior of the Sn, the high strain rate produced by the high initial IMC

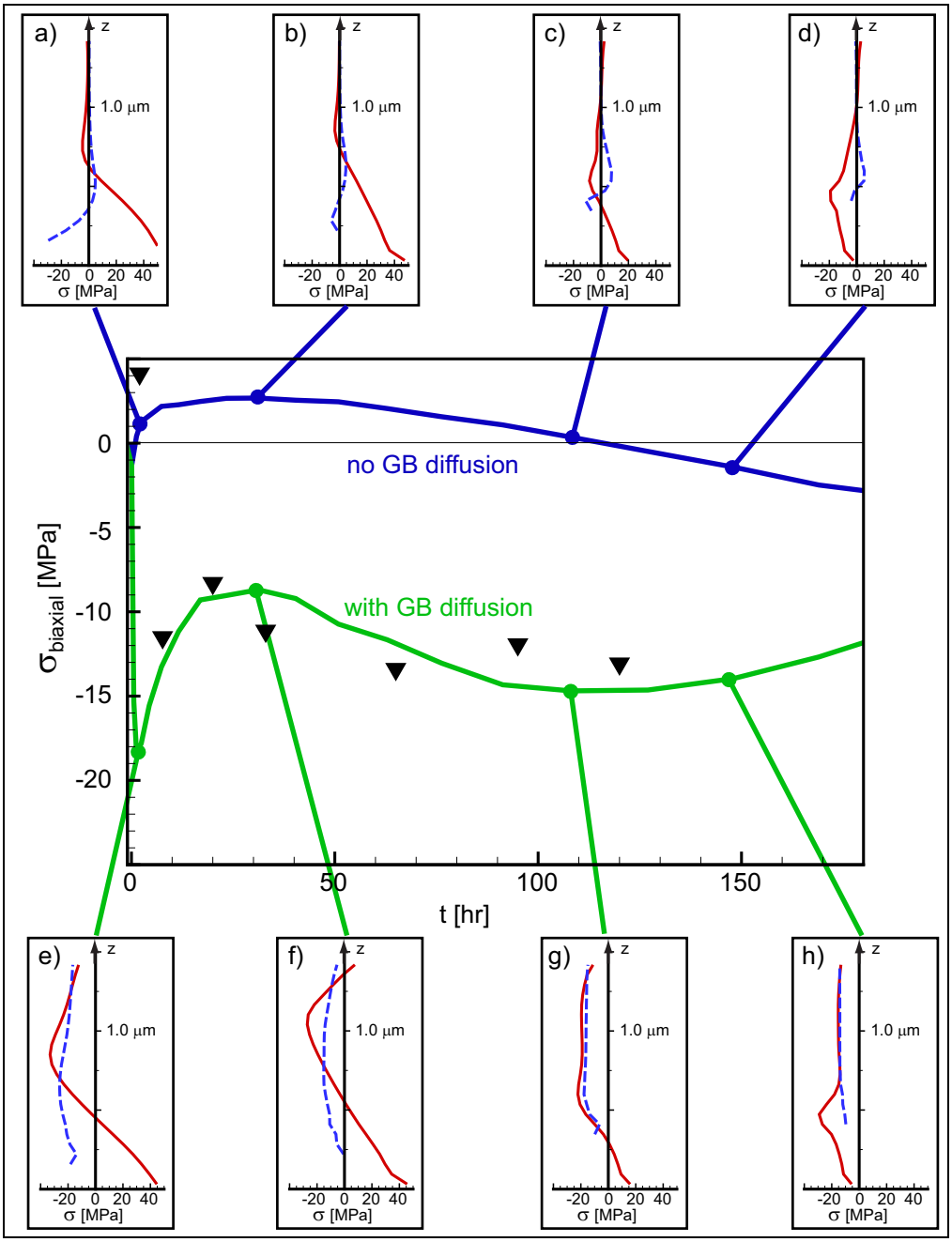

Figure 3.9: Finite element results for models with elastic-viscoplastic Sn constitutive behavior. The central graph plots the evolution of biaxial stress for cases with and without grain boundary diffusion. Symbols are experimental measurements. Insets show biaxial stress along two vertical transects through the Sn, one directly above the IMC growing at triple junctions (dashed blue line), the other at the grain centers (solid red line). In all cases the Sn thickness is 1.45 μm with grain size 1.4 μm (L=0.75 μm) and the IMC growth is modeled as $V_{imc}/A = (0.014\ \mu\text{m}\cdot\text{hr}^{-0.6})t^{0.6}$. Viscoplastic material parameters are $n = 4.5$ and $Q = 70.6$ kJ/mol.

growth rate[1] leads to large compressive stress as seen in Figure 3.9e.

In Figures 3.9e) and f) the vertical stress profiles near the centers of the Sn grains (red curves) suggest the transition from plastic to elastic behavior around a spherical center of contraction. A region of high tensile stress develops near the base of the Sn at the center of the Sn grains, due to the growth of the IMC particles along the surrounding grain boundaries. As the IMC particles expand toward the free surface, tension develops in the adjacent Sn, which remains bonded to the Cu substrate. This region of strong localized tensile stress can be viewed as a center of contraction near the base of the Sn. The transition from tensile to compressive biaxial stress with increasing distance from the base of the film reflects the hoop stress in the region of plastic-dominated deformation. The abrupt change in slope of the stress profile indicates the transition from plastic-dominated to elastic-dominated behavior (analogous to the sharp elastic-plastic boundary in a perfectly plastic material).

The variations in average biaxial stress in the Sn observed after the initial spike in compressive stress arise from the progress of the elastic-plastic transition toward the free surface of the Sn as seen in Figures 3.9e) and f). By 110 hours, the stress within the Sn becomes uniformly compressive above the level of the IMC particles (Figure 3.9g). The rate of IMC growth has also slowed appreciably by this time and the stress gradually relaxes due to viscoplastic creep (Figure 3.9h).

To summarize, the inclusion of viscoplastic constitutive behavior in the FEA simulations, with experimentally-determined material parameters, produces stress-time predictions in agreement with experimental measurements. The predicted stress evolution is somewhat more complicated than that calculated for rate-independent plastic constitutive behavior, but the role played by grain boundary diffusion is very similar. Without grain boundary diffusion, stress remains localized around the expanding

[1]Note that for the cases shown in Figure 3.8, IMC growth is modeled as $V_{imc}/A = (0.014\ \mu\text{m}\cdot\text{hr}^{-0.6})t^{0.6}$ which produces a singular IMC growth rate at $t = 0$.

IMC particles, while the overlying Sn remains nearly stress-free. When grain boundary diffusion is active in the simulations, stress develops throughout the thickness of the Sn. The model also predicts that as the IMC growth rate slows, stress in the Sn will be relaxed by viscoplastic creep. However, experimental measurements indicate that compressive stress in the Sn remains relatively constant, at values between -5 and -10 MPa, for up to two months after deposition [Lee and Lee (1998)]. Why the stress is not relaxed by dislocation-mediated creep as the rate of IMC growth decreases over time, is not immediately clear, but may reflect the effect of work-hardening which is not included in our model.

3.4.3 Effect of Film Thickness

Finite element calculations were also performed for comparison with experimental data collected for a 2.9 μm Sn film deposited on 0.6 μm Cu. As described in Chapter 1, grain size often scales with film thickness, and for these films the mean grain size is 1.8 μm. The measured IMC growth curve for the 2.9 μm Sn samples (see Figure 3.10a) also differed from that measured for the 1.5 μm Sn samples. In the thicker, coarser-grained Sn, IMC growth was initially more rapid and the IMC growth rate slowed more quickly than in the thinner, finer-grained Sn . These differences are reflected in the model $V_{imc}(t)$ functions fit to the two data sets. In the case of the 1.45 μm thick Sn, IMC growth is best fit by $t^{0.6}$ time dependence, while for the 2.9 μm thick Sn the time exponent is 0.25. As seen in Figure 3.10a, there is also more scatter in the experimental V_{imc} measurements for the thicker film compared with the thinner film.

The calculated stress evolution for three different combinations of constitutive behavior, along with the experimental stress measurements for the 2.9 μm thick Sn film, are presented in Figure 3.10b. The results are similar to those for the thinner Sn film. When grain boundary diffusion is included in the model, compressive biaxial

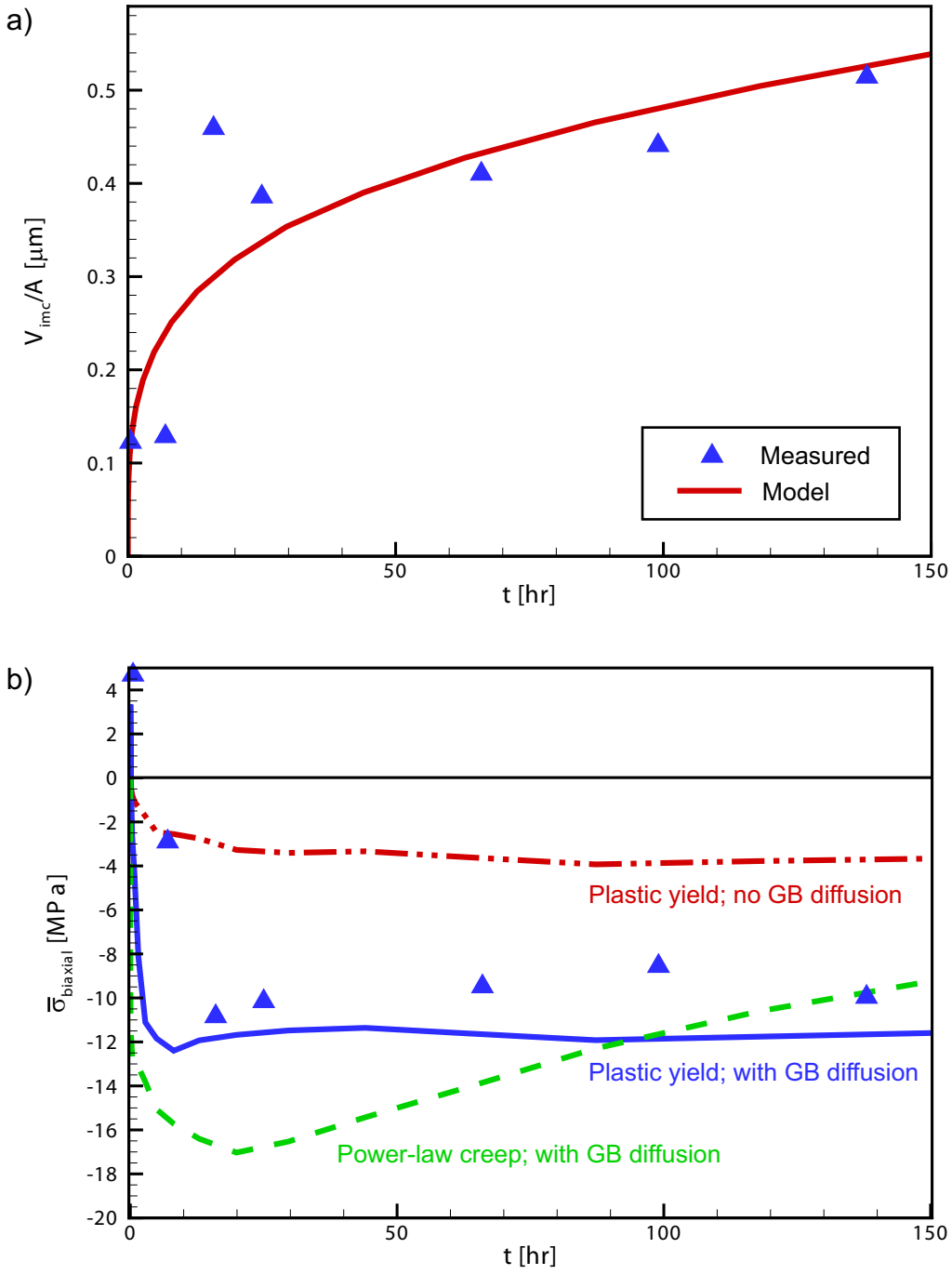

Figure 3.10: Comparison of model results with experimental measurements for 2.9 μm thick Sn film (1.8 μm grain size). a) Symbols (∇) show measured IMC volume. Line is IMC growth curve used in the model calculations: $(V_{imc}/A) = (0.135\mu\text{m}\cdot\text{hr}^{-0.25})t^{0.25}$. b) Calculated mean biaxial stress averaged over the untransformed Sn for three choices of constitutive behavior. Symbols (∇) are experimentally measured values; lines are simulation results.

stress in the Sn rapidly builds to a magnitude limited by plastic relaxation within the Sn, and stress is distributed through the thickness of the film. The increase in compressive stress, however, is more rapid for the thicker film, reflecting the higher initial rate of IMC growth. When grain boundary diffusion is absent from the model, appreciable stress only develops in the immediate vicinity of the expanding IMC particles. The Sn above the level of the IMC particles remains nearly stress-free.

The experimentally measured differences in the average stress measured for the 1.45 μm and 2.9 μm thick Sn films (Figures 3.1e and f), however, are not predicted by the model. For rate-independent plastic behavior, biaxial stress remains constant at approximately -12 MPa as IMC growth continues. This is the same limiting stress magnitude calculated for the 1.45 μm film and reflects the yield strength of the Sn. The approximately 10% to 20% lower compressive stress values measured for the thicker film relative to the thinner film, therefore, cannot explained by the difference in film thickness and grain size alone.

In the case of viscoplastic Sn, the calculated biaxial stress steadily relaxes from its maximum compressive value. The absence of a sharp spike in compressive stress, as seen in calculations for the thinner Sn, reflects the smaller influence of the complex stress field near the IMC particles on the average stress through the film thickness. The degree of stress relaxation predicted by the model, however, is not observed experimentally. This may be due to work hardening during plastic deformation which is not included in the model calculations.

In the preceding cases, the grain size scales with the film thickness. It is also instructive to consider the effect of grain aspect ratio on stress development in columnar Sn films. The rapid time scale for grain boundary diffusion, together with the small excess volume within grain boundaries required to produce compressive stress, suggests that the average stress in the Sn should be relatively insensitive to the thickness

of the film if the grain size is held constant. As seen in Figures 3.5c and 3.5f, relatively uniform biaxial compressive stress, near the yield strength, is produced in the Sn lying above the region of IMC growth. In simulations in which the film thickness is varied from 1.5 μm to 9 μm (with all other parameters identical, including grain size) the average stress in the films varies by less than 10%. It should be noted that the growth of high aspect ratio Sn films by electro-deposition typically involves chemical additions to the plating bath which act to pin grain boundary motion. This may also affect diffusive transport along the grain boundaries.

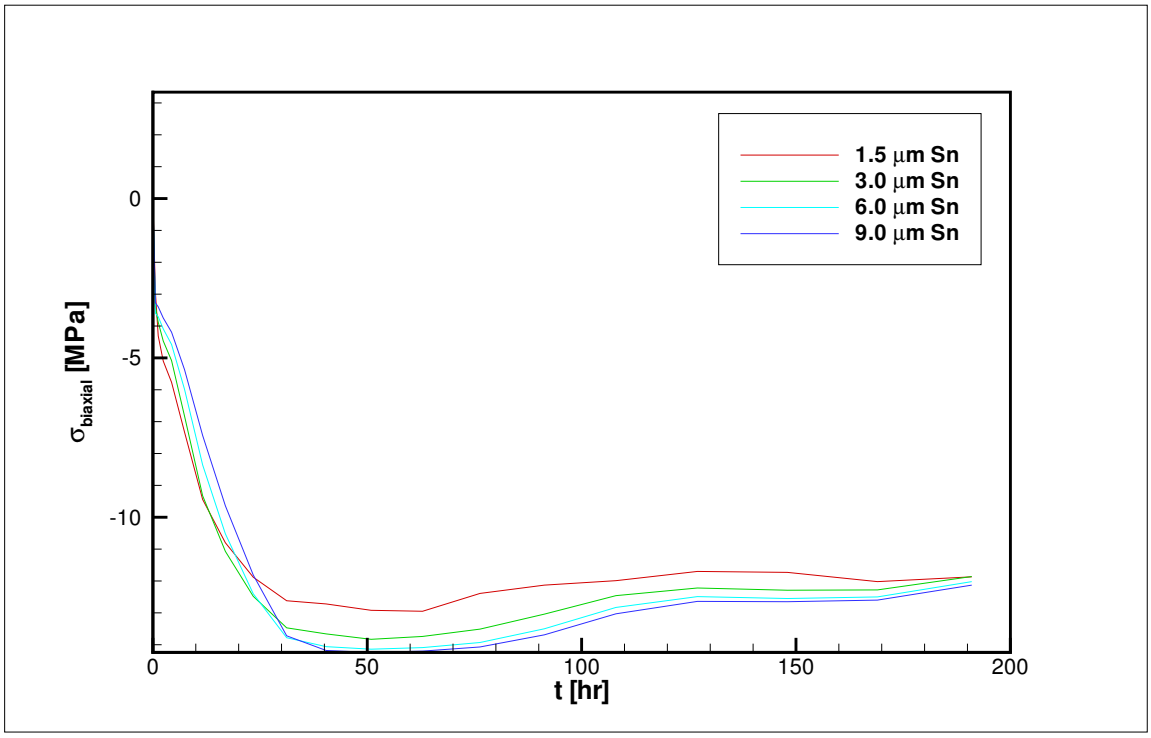

Figure 3.11: Effect of Sn grain aspect ratio on stress evolution. Increasing the film thickness has little effect on the average stress in the Sn when the grain size is held fixed and the same IMC growth curve is assumed. In all cases the grain size is 1.4 μm (L=0.75 μm) and the IMC growth is modeled as $V_{imc}/A = (0.014\ \mu\text{m}\cdot\text{hr}^{-0.6})t^{0.6}$.

3.4.4 Effect of Grain Boundary Diffusivity

We also tested the sensitivity of the modeled stress evolution to the value assumed for grain boundary diffusivity. Variation of the grain boundary diffusivity by three orders of magnitude below and one order of magnitude above the literature value ($4.8 \times 10^{-12}\text{cm}^2/\text{s} \leq D_{\text{gb}} \leq 4.8 \times 10^{-8}\text{cm}^2/\text{s}$) produces a change of only about 10% in the computed average stress levels. From these results we conclude that the time scale governing grain boundary diffusion is much shorter than that governing IMC growth. Thus we do not expect the development of stress is in the Sn film to be limited by the rate of transport along grain boundaries, with the possible exception of the earliest phase of IMC formation when growth rates appear to be very fast.

3.5 Conclusions

The growth of IMC particles at the base of a Sn film generates strain that must be accommodated by the surrounding Sn. Finite element simulations reveal that the details of the resulting stress field in the Sn, as well as the average stress through the Sn layer, are strongly dependent on the deformation processes active within the Sn. Following is a summary of the conclusions that can be drawn from the numerical modeling.

1. Stress-driven grain boundary diffusion, coupled with elastic and plastic behavior within Sn grains, provides an effective mechanism for transmitting stress through the thickness of the Sn. Vertical stress gradients arising from the expansion of IMC at the base of the Sn film drive mass transport upward along grain boundaries. The excess volume in the grain boundaries produces compressive stress resulting in relatively uniform stress though the entire thickness of the Sn.

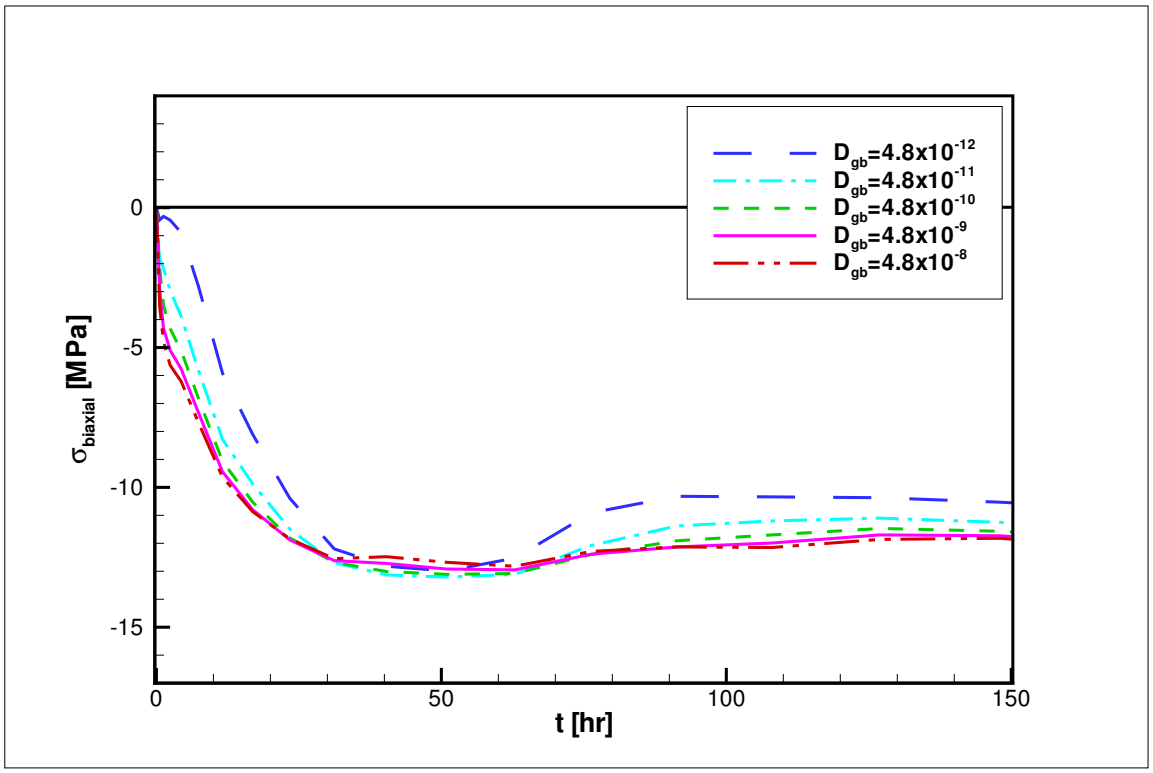

Figure 3.12: Effect of grain boundary diffusion coefficient on calculated stress evolution. Variation of the grain boundary diffusivity by three orders of magnitude below and one order of magnitude above the literature value (4.8×10^{-9}cm^2/s) produces a change of only about 10% in the computed average stress levels. In all cases the Sn thickness is 1.45 μm and grain size is 1.4 μm (L=0.75 μm) and the IMC growth is modeled as $V_{imc}/A = (0.014\ \mu\text{m} \cdot \text{hr}^{-0.6})t^{0.6}$.

2. This mechanism can explain why the stress in the Sn quickly reaches a "steady state" value that remains constant even as IMC continues to grow. Once sufficient volume has been driven into the grain boundaries to bring the entire film to yield, further IMC growth is accommodated plastically and produces no additional stress. The magnitude of the steady state stress reflects the yield stress of the Sn grains. The small excess grain boundary volume required to bring the film to yield and the fast rate of grain boundary diffusion relative to the rate of IMC growth helps explain how the measured Sn stress can reach its steady state compressive value during the early stage of IMC growth.

3. If fast transport of mass along grain boundaries is not possible then the stress produced by elastic and plastic deformation within Sn grains is largely concentrated in a region immediately surrounding the growing IMC particles, at the base of the Sn layer. The stress field diminishes rapidly with distance from the IMC producing large stress gradients through the thickness of the film. Near the surface of the film the calculated in-plane stresses have both tensile and compressive character and are only a few MPa in magnitude.

4. The form of the plastic constitutive law governing deformation within the Sn grains (whether rate-independent yield or rate-dependent viscoplasticity) appears to have a secondary effect on the predicted stress history. The transmission of stress through the thickness of the film by grain boundary diffusion, resulting in a rapid increase in the average compressive stress in the Sn, is still the dominant behavior. The assumption of viscoplastic behavior in the Sn grains produces more a complex stress field at the microscopic scale and greater variation in the time evolution of the average stress in the Sn. The overall stress history predicted by both models, however, is similar.

5. The viscoplastic Sn model predicts decreasing stress levels due to creep relaxation as the rate of IMC growth decreases. This trend, however, is not apparent in the experimental stress measurements. This is somewhat surprising since similar Sn films have been shown to exhibit creep behavior at room temperature [Shin and Chason (2009)] and may be indicative of hardening in the Sn which is not included in the model.

6. The effectiveness of grain boundary diffusion as a mechanism for transmitting compressive stress through the film depends on the columnar microstructure of the Sn, as well as the presence of a passivating oxide layer. This suggests

potential strategies for mitigating whisker formation. If the microstructure or oxide formation could be altered so that strain generated by the growth of IMC could be relaxed via a Coble creep process without producing compressive stress in the Sn, then the driving force for whisker growth could be reduced.

Chapter 4

Whisker Growth Kinetics: FEA

Whisker growth is widely regarded as a mechanism for the relaxation of stress within the Sn film. The basic idea, originally proposed by Fisher *et al.* (1954), is that "whiskers grow by diffusion of tin from a high-pressure region through a region of steep pressure gradient to the whisker base". Material added to the base of the whisker is conveyed out of the plane of the film as the whisker grows, removing volume and relaxing compressive strain. The rate of whisker growth thus depends on the rate at which material can be transported to the base of the whisker which, in turn, depends on the magnitude of the stress gradient surrounding the whisker.

Whisker growth, however, is not the only strain relaxation mechanism operating within the Sn film. As was shown in the previous chapter, the combined operation of plastic deformation within Sn grains and stress-driven diffusion of Sn along grain boundaries is sufficient to prevent significant build-up of compressive stress within the Sn. This raises several questions about how and why whiskers form.

First, if both dislocation motion and whisker growth operate simultaneously to relax strain within the Sn film, how do these two mechanisms interact with and influence each other? Although plastic relaxation within the Sn is sufficient to produce the observed stress evolution in response to IMC growth, the fact that whiskers form

would indicate that they too play a role in relieving strain. Ideally, we would like to understand how strain relaxation is partitioned between whisker growth and plastic deformation within the Sn, and under what conditions one process dominates over the other.

Second, how does the rate of IMC growth affect whisker growth rate? For Sn coatings on Cu, the growth of IMC continuously generates strain within the film. If whiskers play a role in relaxing this strain, then the rate of whisker growth should depend on the rate of IMC growth. Given that several whisker mitigation strategies (*e.g.* post-bake and Ni underlayer) rely on reducing the rate of IMC growth, it would be valuable to understand its relationship to whisker growth rate. How these two rates are related, however, is not immediately obvious as it depends on how the relaxation of strain is partitioned between whisker growth and plastic deformation.

Finally, it is somewhat surprising that a sufficient driving force for whisker growth can be sustained when the compressive stress in the Sn is held at such low values. An analysis of grain boundary transport to a whisker by Tu (1994), required a background stress in the Sn of 70 MPa to produce the observed whisker growth rate of about 2 μm/day. Measured in-plane compressive stress in the Sn film, however, is typically only on the order of 10–15 MPa. In a similar analysis, Hutchinson *et al.* (2004) predict a whisker growth rate of 3 μm/day assuming a more typical background stress of 10 MPa, but their analysis requires a larger value for grain boundary diffusivity and a smaller radius for the diffusion field supplying material to the whisker (20 μm compared with 100 μm assumed by Tu).

In these analyses, the size of the diffusion field surrounding each whisker is assumed to correspond to the mean distance between neighboring whiskers. Since plastic yield within the Sn places an upper bound on the magnitude of the background stress, this would imply that the stress gradient around a whisker, and thus, the rate of whisker

growth, should be lowest when the spacing between whiskers is greatest. However, real-time SEM imaging provides evidence of rapid whisker growth (> 5 μm/day) even when mean spacing between whiskers is large (~ 50 μm) [Jadhav (2010); personal communication]. This would suggest that other factors in addition to whisker density play a role in determining the size of the diffusion field supplying the whisker.

The question of how stress is maintained within the film during whisker growth must also be addressed. Previous diffusion models for whisker growth assume a radial diffusion field surrounding the whisker with a constant stress at the outer boundary [Lindborg (1976), Tu (1994), Tu and Li (2005), Hutchinson *et al.* (2004), Nakadaira *et al.* (2007)]. This boundary stress is typically set by the yield stress of the Sn but no mechanism is provided for the continued generation of stress. This is particularly problematic if the size of the diffusion field is defined by the distance between whiskers, as the boundaries of neighboring diffusion fields coincide.

To address these questions we present a finite element model that includes strain generation as well as two mechanisms for strain relaxation: intra-granular plastic flow and stress-driven grain boundary diffusion. Our model includes no *a priori* assumptions about the conditions controlling diffusion to the whisker. Instead we provide a simple mechanism for maintaining reduced stress in one grain and allow the behavior to emerge naturally from the model. The model results reveal complex kinetic behavior that sheds new light on the questions posed above.

4.1 Whisker Growth Mechanisms

The essential feature of our finite element whisker growth model is the presence of a grain which maintains a lower stress than the surrounding film. The assumption of a low stress grain (or region) is necessary for the development of a stress gradient to drive diffusive transport and can be traced back to the seminal work of Fisher

et al. (1954). A number of microstructural features can be proposed to account for the lower stress at the whisker. Figure 4.1 shows a schematic representation of three such features, or mechanisms, that are examined in this study. In Fig. 4.1a the whisker grain is assumed to have a lower in-plane yield stress under biaxial loading than the other grains. Given the plastic anisotropy of single-crystal Sn, the model in this case could approximate an anomalously oriented grain within a film with strong crystallographic texture. More favorably oriented slip planes within the anomalous grain could allow in-plane strain to be accommodated by dislocation glide at lower stress levels than in the surrounding grains. Normal stress across the grain boundaries adjacent to the whisker would therefore be held at or below the yield stress of the whisker grain.

In Figures 4.1b and 4.1c the whisker grain does not extend to the base of the film, but is bounded below by "root" grain boundaries oriented parallel or at low angle to the surface of the film. Since the Sn surface is traction-free, there is little or no stress normal to the root grain boundaries. For a quantitative estimate of the stress across an obliquely oriented grain boundary, assume the Sn film is in a state of uniform biaxial compression with magnitude σ and a grain boundary makes an angle θ with the free surface (see Fig. 4.1c). The component of traction acting normal to the plane of the grain boundary is then $\sigma \sin^2 \theta$. For a horizontal boundary ($\theta = 0°$) there is no stress acting normal to the grain boundary, and for $\theta = 30°$ the normal stress acting across the grain boundary is 0.25σ. On the vertically-oriented grain boundaries in the surrounding film the full magnitude of the biaxial stress acts normal to the grain boundary plane, producing a higher chemical potential for diffusion relative to the root boundaries beneath the whisker. This provides a driving force for long-range diffusion of Sn to the whisker. We also assume in the model that the arriving material is incorporated into the whisker grain, without regard to the

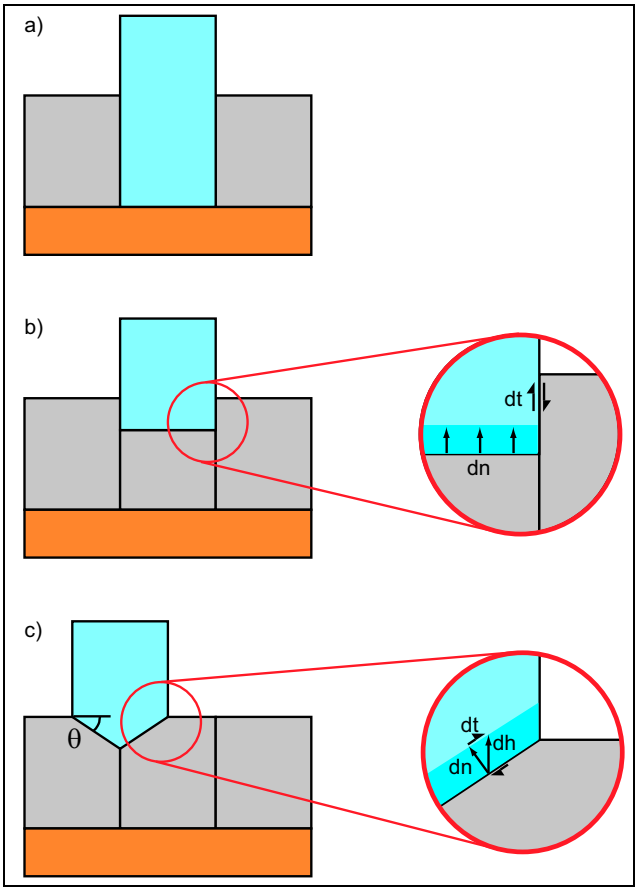

Figure 4.1: Schematic of three whisker mechanisms investigated in this study. a) Shallow whisker grain with horizontal "root" grain boundary. b) Shallow whisker grain with angled "root" grain boundaries. c)"Soft grain" mechanism in which the whisker grain has lower yield stress than the surrounding grains. Insets show components of normal (**dn**) and tangential (**dt**) displacement across grain boundaries associated with an incremental increase in whisker length (**dl**).

specific mechanisms involved.

As the whisker grows, sliding along the grain boundaries generates a viscous-type drag force. In our model, the tangential traction due to grain boundary sliding scales linearly with the sliding velocity (see Section 2.3.2). Thus, the net drag force on the whisker grain depends on the whisker growth velocity and the area and orientation of the sliding boundaries. The component of the net drag force oriented normal to the root boundaries creates back-stress, which reduces the driving force for diffusion by raising the chemical potential at the whisker.

The relationship between grain boundary velocity and sliding resistance depends on the kinematic relations between grain boundary opening and sliding. The simplest case to consider is that of a horizontal root boundary, where there is only normal displacement across the root boundary (Δn in Figure 4.1a) and only tangential displacement along the lateral grain boundaries (Δt in Figure 4.1a). The components Δn and Δt are equal, and the grain boundary sliding velocity is equal to the whisker growth velocity. In the case of a shallow angled root boundary, as shown in Figure 4.1b, both normal and tangential displacements occur across the root boundary in the ratio $\frac{\Delta t}{\Delta n} = \tan\theta$ and the sliding velocity scales as $v_{whisker} \sin\theta$. The effect of grain boundary sliding resistance, therefore, should be less significant for the angled root mechanism as compared with the horizontal root mechanism.

In the case of the "weak grain" mechanism, the relationship between whisker growth and grain boundary sliding is more complex. Extrusion of the whisker from the film requires sliding along the vertical grain boundaries. However, due to plastic deformation, the velocity field within the whisker grain varies from the base of the film to the surface. At the Sn-Cu interface, there will be no tangential velocity jump across the vertical grain boundaries. The velocity jump will increase with distance from the base, becoming equal to the whisker growth velocity at the free surface.

4.2 Model Description

The finite element model discussed in Chapter 3 has been extended to include whisker growth. The primary goal of the analysis is to calculate the rate of material transport to a whisker via stress-driven diffusion along the Sn grain boundary network. The model must therefore include a mechanism for maintaining reduced stress at the whisker relative to the surrounding film and span an area large enough to adequately account for long-range transport. Implicit in this model is the assumption that transport of Sn to the whisker is the rate-limiting process in whisker growth, *i.e.* that new material can be incorporated into the whisker grain as quickly as it can be delivered.

As described in the previous chapter, the Sn film is modeled as an array of columnar grains with hexagonal cross-section, bonded to a homogeneous Cu substrate. Each grain is treated as a homogeneous elastic-plastic solid, and grain boundary diffusion elements separate individual grains. Where the present model differs is in the inclusion of a "whisker grain" whose mechanical properties or microstructure allow it to relax stress more effectively that the other grains in the model.

Figure 4.2a shows a typical model cell. The whisker grain, at the corner of the model cell, has been highlighted in blue. Symmetry boundary conditions effectively create a periodic repetition of the model in the two lateral directions. Thus the model represents a Sn film of infinite lateral extent with a periodic array of whisker grains arranged on a square lattice, as shown in Figure 4.2b. The number density of whiskers in the simulations is controlled by adjusting the size of the model cell.

To simulate realistic whisker densities, which typically range from $10/\text{mm}^2$ to several $100/\text{mm}^2$ [Tu (1994), Lee and Lee (1998), Chason *et al.* (2008)], requires a large model cell containing many Sn grains. For example, a model cell with quarter symmetry corresponding to a Sn film with whisker density of $500/\text{mm}^2$ and grain size

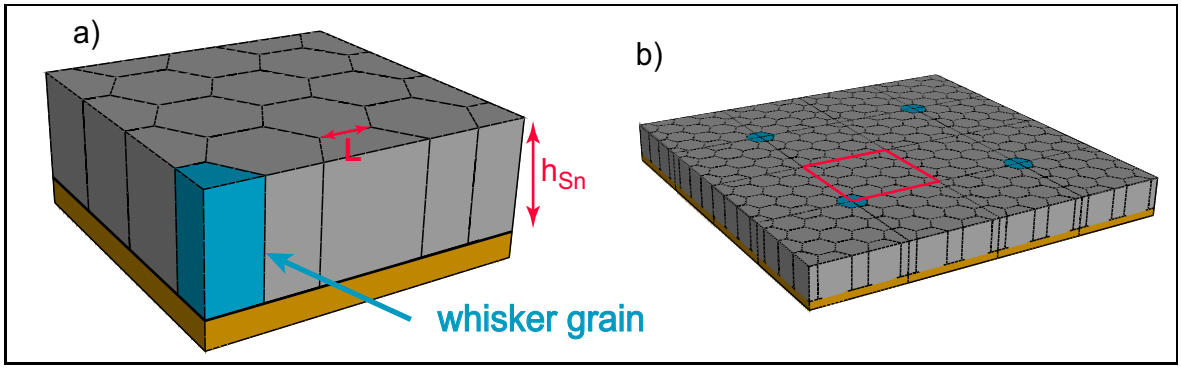

Figure 4.2: a) Typical finite element model cell for whisker growth calculation. The whisker grain, which in this case has a lower yield stress than the surrounding grains, is highlighted in blue. b) Symmetry boundary conditions applied at the lateral faces of the model cell effectively create a periodic array of whisker grains.

$\sim$1.8 μm would contain nearly 200 grains. For models of this size the computational expense involved in simulating the growth of individual IMC particles, as was done in Chapter 3, becomes prohibitive. At the necessary mesh resolution, a 200 grain model would comprise roughly 6,000,000 elements and 20,000,000 degrees of freedom.

In order to reduce the problem to a more tractable size, the effect of IMC growth is approximated by applying a steadily increasing stress-free transformation strain (similar to thermal expansion) over the entire Sn region. This can be justified by considering the results of Chapter 3 which suggest that excess volume generated by IMC expansion is redistributed vertically through the Sn film by grain boundary diffusion. The continuous growth of IMC can therefore be viewed as a continuous source of excess volume (or volumetric strain) within the Sn film. The numerical procedure used to impose the stress-free transformation strain is essentially the same as that used to impose thermal strain. Because the strain is applied uniformly through the Sn layer, larger elements can be used in the finite element calculations without loss of accuracy. This approximation, however, introduces new uncertainty through the assumptions that must be made in correlating the applied expansion with IMC growth. The question of how to correlate experimentally measured IMC volume and

Quantity	**Symbol**	**Value**		**Ref.**
Sn film thickness	h_{Sn}	2.0	μm	
Length of hexagonal grain edge	L	1.0	μm	
Cu film thickness	h_{Cu}	0.5	μm	
Elastic modulus of Sn	E_{Sn}	50	GPa	(1)
Poissons ratio of Sn	ν_{Sn}	0.36		(1)
Yield strength of Sn	Y_{Sn}	15	MPa	(1)
Elastic modulus of Cu	E_{Cu}	117	GPa	(1)
Poissons ratio of Cu	ν_{Cu}	0.34		(1)
Yield strength of Cu	Y_{Cu}	200	MPa	(2)
Grain boundary diffusivity of Sn	D_{gb}	4.8×10^{-9}	cm^2/s	(3)
Grain boundary width of Sn	δ	0.5	nm	(3)
Grain boundary sliding velocity of Sn	η_{gb}	10^{-4}	m/s	
Atomic volume of Sn	Ω	0.027	nm^3	
Temperature	T	298	K	

Table 4.1: Parameters used in the whisker growth simulations. References: (1) Gale and Totemeier (2004); (2) Freund and Suresh (2003); (3) Lange and Bergner (1962).

the applied volumetric strain is taken up in Section 4.3 below.

The finite element procedure for calculating whisker growth velocity is described as follows. In a typical whisker growth FEA calculation, a total volumetric strain of 0.0075 is applied in equal increments over 5 load steps. The load increment, corresponding to a constrained linear expansion of $\varepsilon^* = 0.0005$, was chosen to be large enough to induce yield in the film [$E\varepsilon = (5 \times 10^4 \mathrm{MPa})(5 \times 10^{-4}) = 25\mathrm{MPa} > \sigma_y$]. The applied strain rate for each FEA calculation was controlled via the time interval specified for the load steps. To calculate the steady state whisker growth rate, the displacement of the free surface of the whisker grain is recorded at the end of each load step. The rate of whisker growth as a function of the applied volumetric strain, $\frac{dh_w}{de}$, is then found by least square fit to a straight line using the TecPlot visualization software. Multiplying by the applied strain rate, $\dot{e}$, gives the whisker growth velocity.

Idealized elastic-perfectly plastic constitutive behavior is assumed within Sn grains. Parameter values used in the FEA calculations are shown in Table 4.1. The model

parameters can be combined to form the following dimensionless groups in order to better understand the parameter space that needs to be explored.

$$\begin{aligned} \tau_d &= \frac{kTL^3}{\Omega\delta D_{gb}\Delta\sigma} & \tau_e &= \frac{1}{\dot{e}^*} \\ \tilde{v}_d &= \frac{d\tilde{h}_w}{d\tau_d} & \tilde{v}_e &= \frac{d\tilde{h}_w}{d\tau_e} = \frac{d\tilde{h}_w}{de} \\ \dot{E} &= \frac{\dot{e}kTL^3}{\Omega\delta D_{gb}\Delta\sigma} & S &= \frac{L^2\eta_0}{\delta D_{gb}} \\ N &= \frac{A_w}{A_f} & d\tilde{h}_w &= \frac{h_w}{h_{Sn}} \end{aligned}$$

h_w is the length of the whisker (height above the Sn surface) and $\Delta\sigma$ is a measure of the difference between the far-field stress and the stress at the whisker grain. For the assumption of perfectly plastic Sn behavior used in the finite element models, $\Delta\sigma$ is set equal to the yield stress of the Sn, Y_{Sn}. All other variables are identified in Table 4.1.

The non-dimensional groups have the following physical meaning. τ_d and τ_e are the two characteristic time scales for the problem, the first associated with diffusional transport, the second with the rate of loading or strain generation. Note that τ_d depends only on temperature and material parameters which typically remain constant for a given material system. The dimensionless rate of whisker growth relative to τ_d, $\tilde{v}_d$, should therefore correlate with the dimensional whisker growth rates measured for a real system. $\tilde{v}_e$, on the other hand, measures the change in whisker length per unit applied volumetric strain e^*. The dimensionless strain rate, $\dot{E}$, is a ratio of the strain rate time scale to the diffusional time scale. N is the normalized whisker density, where A_w is the area occupied by whisker grains and A_f is the total area of the film. Finally, S is a ratio of grain boundary sliding velocity to grain boundary diffusion rate. $\dot{E}$ and N define the primary parameter space explored here. We also examine the effect of S.

Additionally, the "efficiency" of whisker growth can be defined as the fraction of total excess volume generated within the film that is removed by the whisker. In

terms of previously defined dimensionless parameters, the whisker efficiency can be expressed as:

$$\eta \equiv \frac{dV_w}{d\Delta V} = \frac{d(h_w A_w)}{d(2/3 e h_f A_f)} = (3/2) N \cdot \tilde{v}_e \tag{4.1}$$

When $\eta = 1$ all excess volume generated within the film is removed by whisker growth, and when $\eta = 0$ all excess volume is accommodated by plastic deformation within the film. The factor of 2/3 arises because the film is unconstrained in the out-of-plane direction. The component of the applied stress-free strain in this direction does not generate strain that must be relaxed by deformation within the Sn.

4.3 Finite Element Results

The FEA results for the three whisker mechanisms discussed in Section 4.1 are both qualitatively and quantitatively very similar. In this section key aspects of the mechanical behavior and the resulting whisker kinetics will first be illustrated through examination of results for the horizontal whisker root mechanism. After the fundamental aspects of the behavior have been identified and discussed, variations due to differences among the three distinct whisker growth mechanisms will be examined. Implications of the model results for understanding whisker growth in real systems will be explored in the discussion section. In this section the focus is on understanding the behavior of the model system.

4.3.1 Stress field surrounding a whisker

Figure 4.3 shows contours of mean biaxial stress, $\frac{1}{2}(\sigma_{11}+\sigma_{22})$, in the neighborhood of a whisker growing at steady state. The mean biaxial stress approximates the normal stress across the vertically-oriented grain boundaries and thus correlates with the driving force for mass diffusion. As seen in the figure, a stress gradient develops

both laterally and vertically within the Sn film surrounding the whisker root. The origin of this gradient is explained by the presence of the horizontal grain boundary at the whisker root, which effectively acts as a stress-free sink for material. Where the normal stress acting across vertical grain boundaries is compressive, atoms are removed from the adjacent Sn grains and transported along the grain boundaries to the whisker root. Atoms arriving at the whisker root are incorporated into the whisker which is free to grow vertically without creating additional stress. Thus, the whisker relaxes in-plane compressive strain by accumulating material from the surrounding Sn and conveying it out of the film.

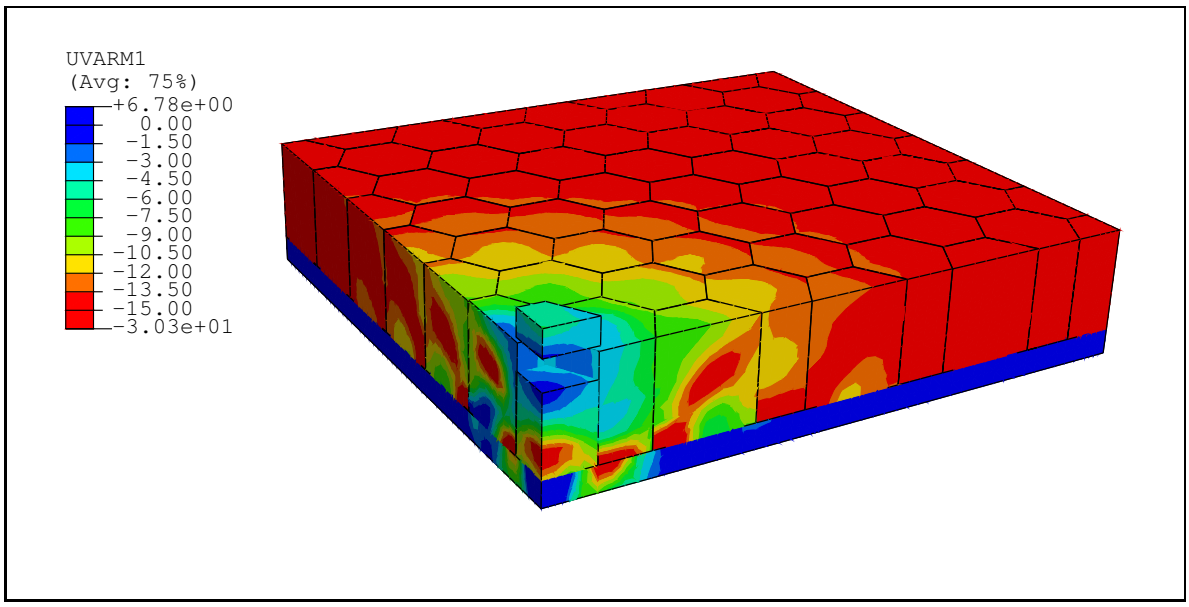

Figure 4.3: Contours of mean biaxial stress in the neighborhood of a whisker growing at constant rate. Total volumetric strain is $e = 1.5 \times 10^{-3}$; normalized strain rate is $\dot{E} = 1.26 \times 10^{-2}$; normalized area per whisker is $A = 208$; grain boundary sliding to diffusion ratio is $S = 140$. Note that the apparent gap below the whisker grain represents material that has been added to the whisker. The post-processing software does not display the grain boundary diffusion elements.

Less obvious is why the stress relaxation is limited to a well-defined region immediately surrounding the whisker. As seen in Figures 4.3 the stress gradient does not extend to the model boundaries, but terminates at a radius about three grain

diameters from the whisker. Beyond this relaxed region the mean biaxial stress is uniformly compressive. It should be emphasized that this is the steady state stress field that develops when volumetric strain is applied in the model at a constant rate. That the model has achieved steady state can clearly be seen in Figure 4.4 which shows contours of mean biaxial stress at three successive load steps. During each load step the whisker height increases by 0.3 μm or 0.15 times the film thickness, while the stress field remains virtually unchanged.

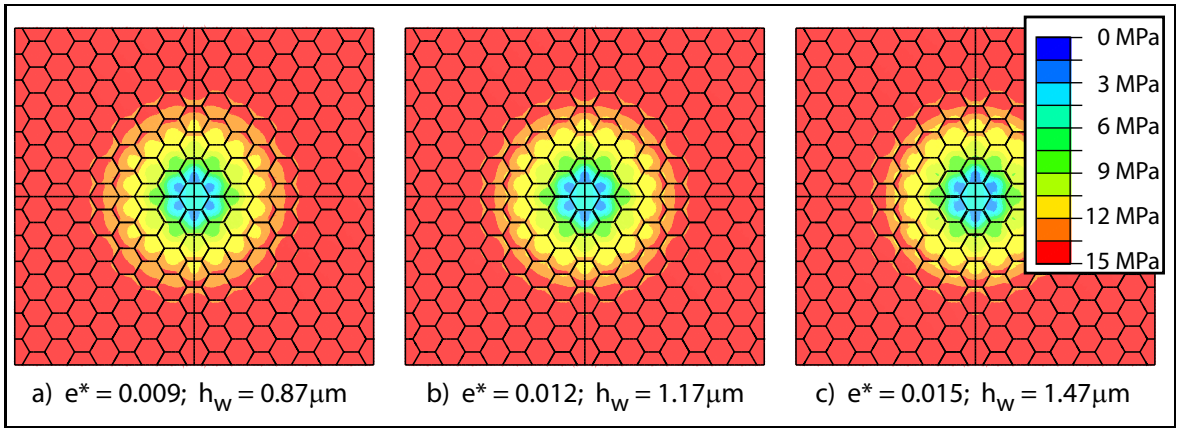

Figure 4.4: Mean biaxial stress around a whisker at successive load steps. The stress field remains constant as the applied volumetric strain (e^*) and whisker height (h_w) steadily increase, indicating that the system is at steady state. The applied volumetric strain rate is $\dot{e^*} = 2.63 \times 10^{-7}$/s.

The fact that the relaxed region surrounding the whisker does not extend to the periodic model boundaries indicates that the steady state stress field is not influenced by the presence of neighboring whiskers. This conclusion is further substantiated by the observation that the size of the relaxed region and the rate of whisker growth are unaffected when the size of the model cell is doubled. This is particularly interesting, as all previous quantitative models of whisker growth have assumed that the stress gradient around the whisker is controlled by the spacing between whiskers [Chaudhari (1974), Tu (1994), Hutchinson *et al.* (2004), Nakadaira *et al.* (2007)]. Understanding the processes controlling the size and nature of the steady state stress field around a

whisker should therefore provide new insight into the kinetics of whisker growth.

The observed steady state behavior indicates a balance between the rates of strain generation and strain relaxation. Since the Sn film is constrained against lateral displacement by the substrate, the in-plane components of total strain must be zero. In the model, in-plane compressive strain is generated by the applied volumetric expansion which approximates the effect of IMC growth. At steady state, this strain must be completely accommodated by a combination of local plastic shearing within the Sn grains and long-range diffusive transport to the whisker. Diffusive transport requires a gradient in stress to provide a driving force, while plastic yield, under the assumption of perfect plasticity, produces a uniform stress field[1]. Therefore, in regions where the Sn grains yield plastically, there is no stress gradient to drive grain boundary diffusion. In these regions, in-plane compressive strain is relieved by shearing of the Sn grains and local thickening of the film. Conversely, in the vicinity of the whisker, compressive strain is relaxed by the removal of Sn atoms adjacent to the grain boundaries and their subsequent transport to the whisker grain where they are conveyed out of the film. Where diffusive transport to the whisker relaxes strain, stress in the Sn remains below the yield stress and there is no plastic shearing within Sn grains.

The region of stress relaxation surrounding the whisker, then, also defines the diffusion field supplying material to the whisker. Since there is no plastic shearing within the relaxed region, all compressive strain generated within that region must be relieved by transport to the whisker. The size of the steady state diffusion field around an isolated whisker is therefore controlled by the rate of strain generation relative to the rate of diffusive transport: specifically by the dimensionless parameter $\dot{E} \equiv$

[1] If the out-of-plane stress component is assumed to be zero, then the von Mises equivalent stress, which defines the yield criterion, has the same magnitude as the equibiaxial stress within the film. Gradients in the in-plane stress can therefore only arise from changes in the yield envelope due to strain hardening.

$\left(\frac{\dot{e}kTL^3}{\Omega\delta D_{gb}\Delta\sigma}\right)$. When $\dot{E}$ is large (*i.e.* strain generation is fast relative to grain boundary transport), the diffusion field is restricted to a small region around the whisker. At smaller values of $\dot{E}$ the diffusion radius becomes larger as Sn is transported a greater distance in the characteristic time associated with the rate of strain generation. The increasing size of the diffusion radius with decreasing values of $\dot{E}$ can be seen in the plots of biaxial stress in Figure 4.5, parts a), b) and c). The corresponding partitioning of strain relaxation between plastic shearing and mass transport to the whisker is indicated in Figures 4.5 d) through f).

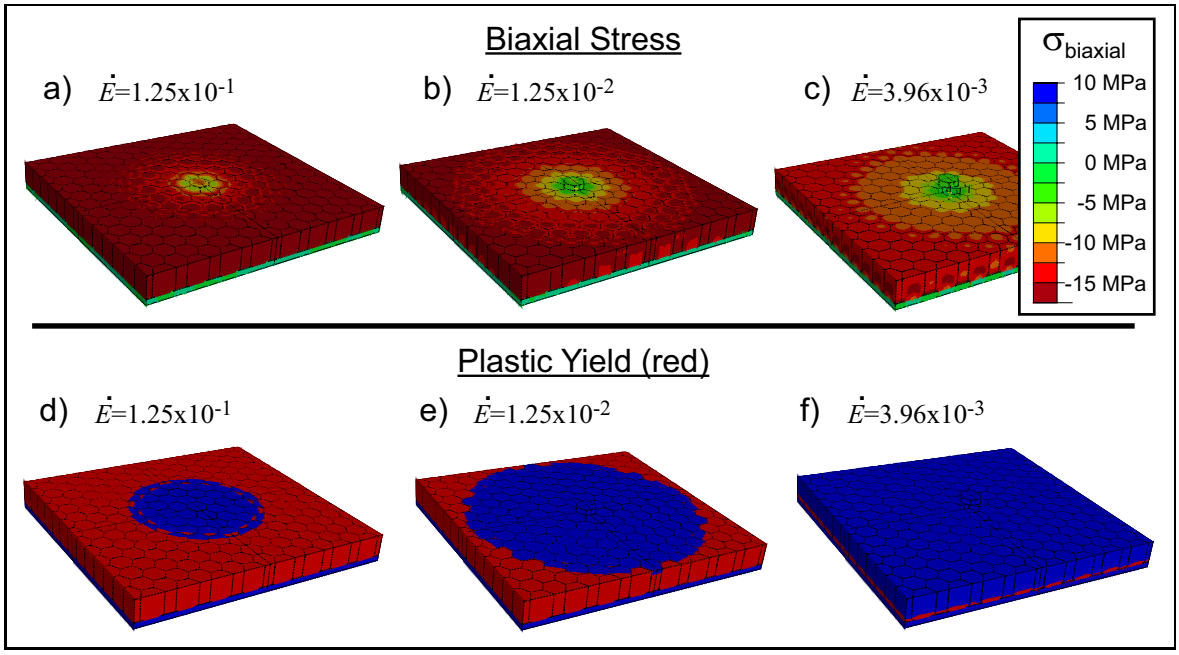

Figure 4.5: (a,b,c) The size of the diffusion field (defined by the region of relaxed biaxial stress) increases as the applied strain rate decreases. (d,e,f) The partitioning of strain relaxation between plastic flow (red) and diffusional transport (blue) is shown for the same models. Applied strain rates are indicated above each cont

The preceding argument applies for isolated whiskers, *i.e.* whiskers separated by more than twice the diffusion radius so that their diffusion fields do no overlap. For a periodic array of whiskers, there will be a critical value of $\dot{E}$ for which the diffusion radius is exactly half the distance between neighboring whiskers. For $\dot{E}$ less than

this critical value the diffusion fields of neighboring whiskers overlap and stress across the entire film is maintained below the yield stress, as shown in Figure 4.5c. In this "whisker-dominated relaxation" regime, all strain generated within the film is relaxed by mass transport to whiskers and plastic deformation within Sn grains plays almost no role (see Figure 4.5f)[2].

The combination of normalized strain rate, $\dot{E}$, and normalized whisker density, N, determines whether whisker growth is the dominant relaxation mechanism or if relaxation is partitioned between whisker growth and dislocation plasticity. By plotting the character of each whisker growth simulation (whisker-dominated or mixed relaxation) against the values of N and $\dot{E}$, a phase diagram has been created in Figure 4.6. The curve marks the boundary in N–$\dot{E}$ space between the two regimes of relaxation. For large $\dot{E}$ (fast IMC growth) the diffusion radius of an isolated whisker is small and therefore the a large whisker density (small distance between whiskers) is required for whisker-dominated relaxation. At small values of $\dot{E}$ (slow IMC growth) the diffusion radius is large, so the transition between whisker-dominated and mixed relaxation regimes occurs at smaller whisker density. To facilitate comparison with experimental measurements, dimensional values of estimated IMC growth rate and whisker density are shown on the upper and right axes of Figure 4.6 for a Sn film with the properties listed in Table 4.1. Calculation of the estimated IMC growth rate is explained in Section 4.3.5.

4.3.2 Partitioning of strain relaxation

The partitioning of strain relaxation between whisker growth and plastic shearing can be quantified by examining the rate of whisker growth relative to the applied

[2]In the finite element calculations there is localized plastic yield within the Sn grains near the base of the film due to the constraint of the Cu substrate. As seen in the previous chapter, localized plastic deformation within Sn grains would also be expected in the neighborhood of growing IMC particles.

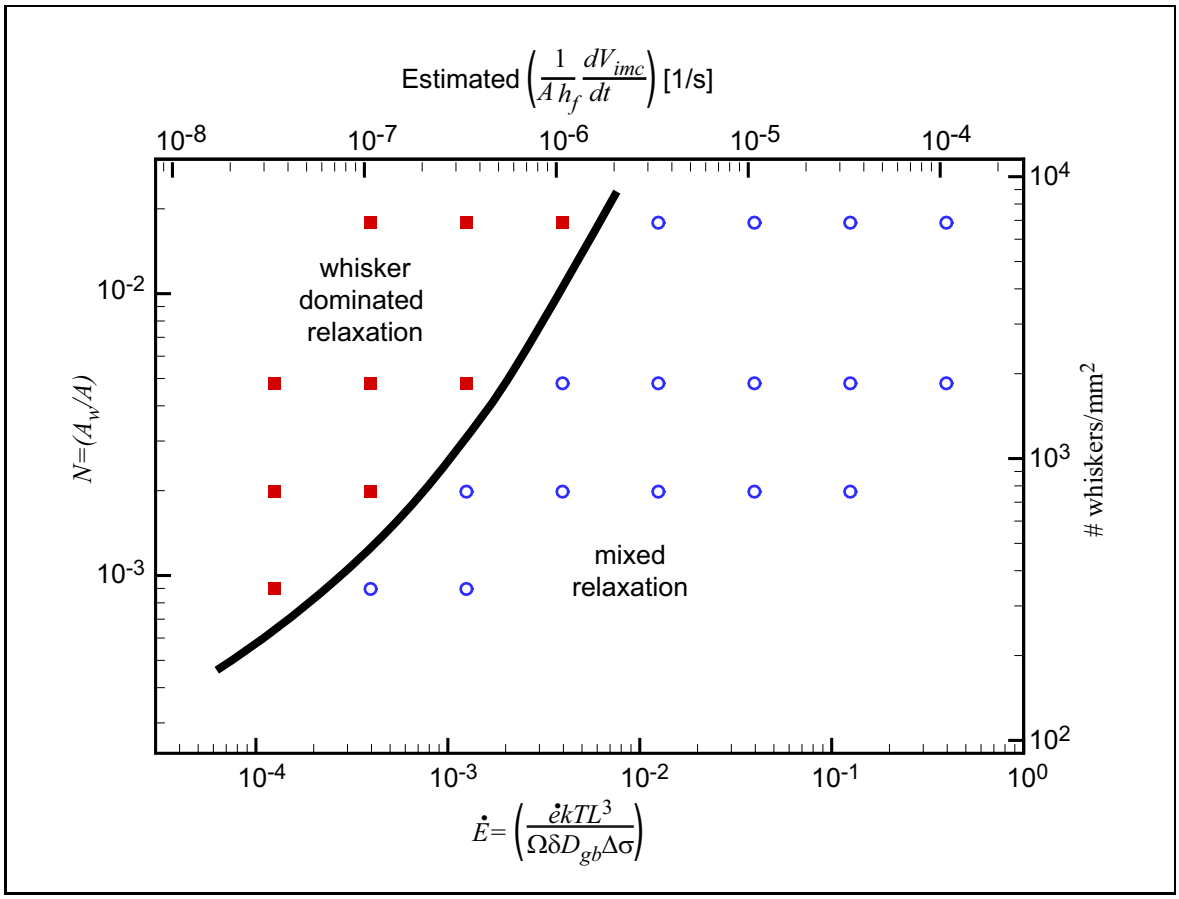

Figure 4.6: "Phase diagram" showing the boundary between whisker-dominated (red squares) and mixed (blue circles) relaxation regimes. Each symbol represents a finite element simulation of whisker growth for the values of normalized strain rate and whisker density indicated on the bottom and left axes. In the whisker-dominated regime, mass transport to whiskers accounts for nearly all strain relaxation. In the mixed regime, strain relaxation by whiskers is limited to a region immediately surrounding the whisker. Beyond this region, strain is accommodated by plastic shearing within Sn grains. The right axis shows whisker density and the upper axis shows estimated IMC growth rate for a Sn film with properties listed in Table 4.1.

strain rate. In the laterally-constrained thin film, the applied volumetric strain can be thought of as a source of *excess* volume which must be accommodated. The rate of excess volume production in the film per unit area is $\frac{1}{A}\frac{d(\Delta V)}{dt} = (2/3)\dot{e}^* h_{Sn}$. The factor of 2/3 arises because the film is unconstrained in the out-of-plane direction. Therefore only the two in-plane components of the spherical volumetric strain contribute to the excess volume that must be either removed by whisker growth or accommodated by local plastic thickening.

Whisker growth rate can also be viewed as the rate of volume removal by the whisker normalized by the cross-sectional area of the whisker. The normalized whisker growth rate, $\tilde{v}_e = \frac{1}{h_{Sn}}\frac{dh_w}{de^*}$, measures the rate of volume removal by the whisker relative to the rate of excess volume production per unit area. A log-log plot of $\tilde{v}_e$ as a function of the normalized strain rate, $\dot{E}$, is presented in Figure 4.7. Four sets of finite element results are plotted, each corresponding to a different model cell size, and thus a different whisker density.

In Figure 4.7 the normalized velocities calculated for each whisker density show the same pattern of variation with $\dot{E}$. Consider the results for a single whisker density. At the lowest strain rates, $\tilde{v}_e$ remains constant as $\dot{E}$ increases, then beyond a critical value of $\dot{E}$, $\tilde{v}_e$ decreases with increasing strain rate. Note that all of the data sets converge to the same linear trend on the log-log plot with slope -0.69. The physical origin of this exponent will be investigated Chapter 5 in the context of a mathematical model that describes whisker growth. What is important here is that $\tilde{v}_e$ varies inversely with $\dot{E}$ and that the exponent is fractional, so that the variation is sub-linear.

The variation of $\tilde{v}_e$ with $\dot{E}$ in Figure 4.7 reflects the expansion of the diffusion field around a whisker with decreasing strain rate. This is most easily explained by considering the progression from high strain rate to low strain for a given whisker

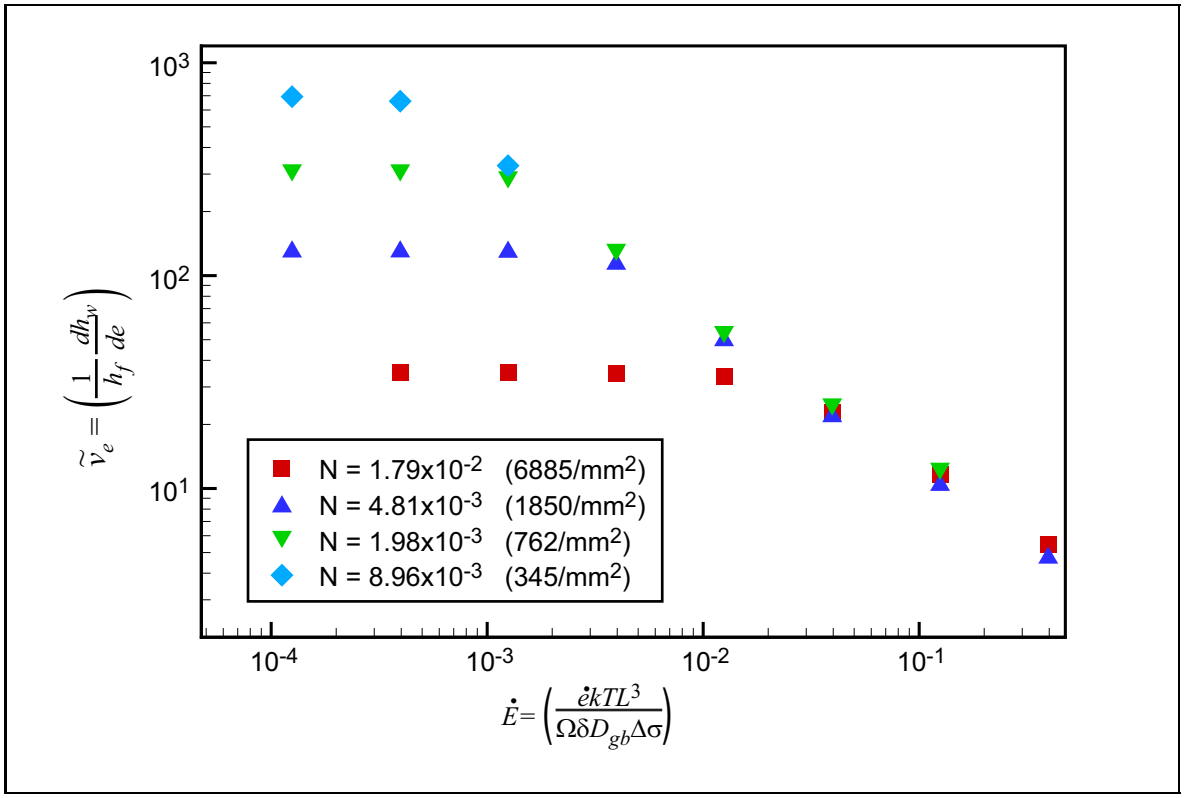

Figure 4.7: Normalized whisker growth rate as a function of dimensionless strain rate. $\tilde{v}_e = \frac{1}{h_{Sn}}\frac{dh_w}{de^*}$ measures the rate of volume removal by the whisker relative to the rate of excess volume production per unit area. Curves show FEA results for different choices of normalized whisker density, N. The corresponding dimensional whisker density for a model film with $L = 1$ μm is shown in parentheses.

density. First, recall that at steady state, all of the excess volume generated within the diffusion field must be transported to the whisker and removed. Note also that $\tilde{v}_e$ is a measure of volume removed by the whisker relative to the applied strain. At high applied strain rates, when the diffusion radius is small and there is no interaction between neighboring whiskers, $\tilde{v}_e$ varies in direct proportion to the area of the diffusion field. The sloped portion of the curve to which all the data sets collapse is then a measure of the area of the diffusion field supplying material to an isolated whisker. As the strain rate decreases, the area of the diffusion field increases. For a single whisker in an infinite film, this relation would continue indefinitely. However, for a

finite whisker density, the diffusion fields of neighboring whiskers eventually begin to overlap at sufficiently low strain rate. Beyond this point the area drained by each whisker remains constant, as indicated by the horizontal portions of the curves. The limiting value of $\tilde{v}_e$ is $2/3(A/A_w)$ or $(2/3)(1/N)$.

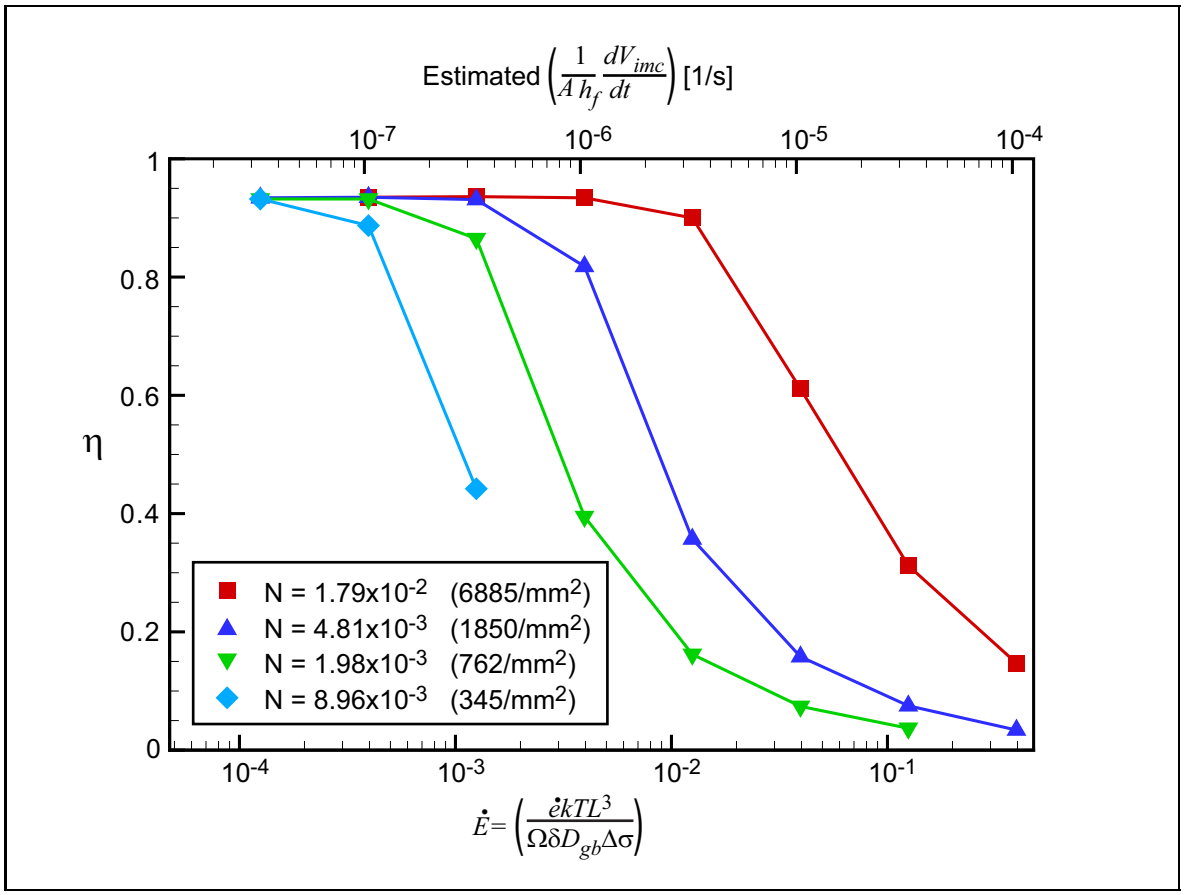

Figure 4.8: Fraction of total strain relaxation due to whisker growth. When $\eta = 1$ all excess volume generated within the film is removed by whisker growth, and when $\eta = 0$ all excess volume is accommodated by plastic deformation within the film.

If $\tilde{v}_e$ is normalized by this limiting value we get the fraction of total excess volume generated within the film that is removed by whisker growth. This is the "whisker efficiency", η, defined in Section 4.2 which provides a direct measure of the partitioning of strain relaxation between whisker growth and local plastic shear. Whisker efficiency is plotted as a function of normalized strain rate and whisker density in

Figure 4.8. In this graph, the maximum values of η at low strain rates correspond to the whisker-dominated relaxation regime discussed previously. Ideally η should attain a value of 1.0. The maximum value achieved in the simulations is slightly less than this due to a small amount of plastic deformation at the base of the Sn where it is constrained by the substrate.

The information presented in Figure 4.8 is similar to that plotted in the relaxation "phase diagram" (Figure 4.6), but with the addition of a quantitative measure of the degree of partitioning within the mixed relaxation regime. To summarize the main conclusions of this section, at sufficiently high applied strain rates or low whisker densities plastic shearing is the dominant mode of relaxation and the diffusion fields surrounding the whiskers comprise a small fraction of the total area of the film. At the other extreme, at sufficiently low applied strain rates or high whisker densities the diffusion fields of all the whiskers merge and whisker growth relaxes all the strain. In this regime stress in the film is maintained below the yield stress. The central question of where real Sn plating films lie within this continuum will be taken up in Section 4.4.

4.3.3 Calculated whisker growth velocities

In the preceding section, we examined the rate of whisker growth with respect to the strain rate in order to understand how strain is partitioned between the two relaxation mechanisms. We now consider the factors controlling the whisker growth velocity, the rate of whisker lengthening per time. Steady state whisker growth velocities obtained from the finite element simulations are plotted in Figure 4.9. The normalized whisker growth velocity in this case is $\tilde{v}_d$, which correlates with the time rate of change of whisker length when material properties and temperature remain fixed. Four sets of results are presented, each corresponding to a different whisker

density. Curves connecting members of each data set have been added as visual guides.

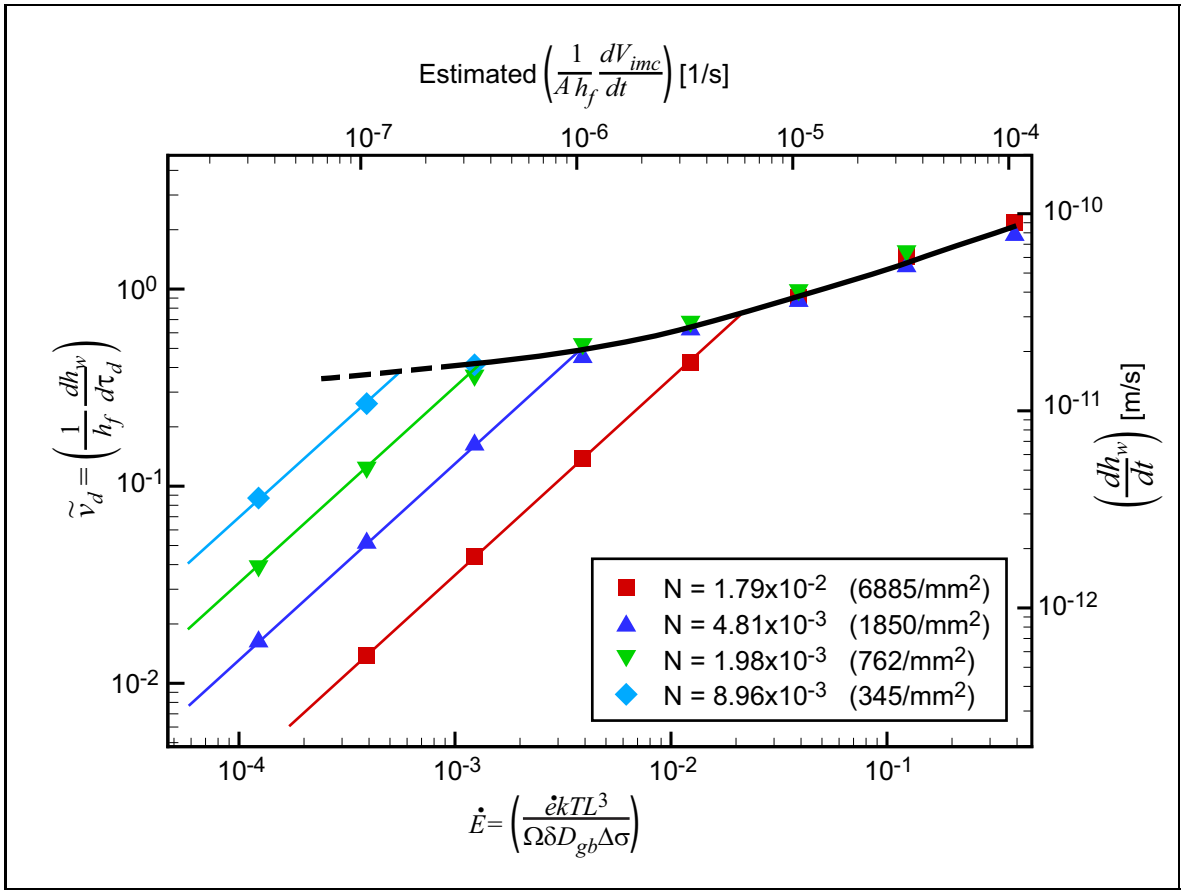

Figure 4.9: Whisker growth velocities as a function of normalized strain rate calculated from finite element simulations. Four sets of results are presented, each corresponding to a different whisker density. Curves connecting members of each data set have been added as visual guides. Dimensionless velocity is shown on the right axis. Dimensional values of of whisker growth velocity and estimated IMC growth rate for a Sn film with the parameter values in Table 4.1 are shown on the upper and right axes, respectively.

The calculated whisker growth velocities in Figure 4.9 define two distinct kinetic regimes, one represented by the curve drawn in black near the top of the graph, the other by the family of straight lines trending from the lower left toward the upper right. As we will show in the following discussion the different growth kinetics

correlate with the two regimes of relaxation identified previously.

First consider the behavior described by the diagonal lines in the lower left quadrant of the graph. The slope of each line is 1.0 on the log-log plot, indicating a linear relationship between the whisker velocity and the applied strain rate. The interpretation here is straightforward. Strain relaxation in these cases is in the whisker-dominated regime, in which all excess volume generated within the film is removed by whisker growth. Consequently, the whisker growth velocity varies in direct proportion to the applied strain rate.

The behavior described by the curve near the top of the graph is more complicated. Here the slope increases slightly with strain rate, and more importantly, the slope is significantly less than one. This indicates a weaker than linear dependence of whisker growth velocity on strain rate. Note that a variation of three orders of magnitude in the strain rate produces only about a five-fold change in the whisker growth rate. Understanding the mechanisms controlling this kinetic behavior is crucial as it could have important implications for whisker mitigation strategies.

Note that the models giving rise to these results are in the mixed relaxation regime, meaning that the diffusion fields of neighboring whiskers do not interact. Due to the partitioning of relaxation, all of the excess volume generated within the diffusion field is transported to the whisker. Therefore, whisker velocity, which also measures the rate of material transport to the whisker, is directly proportional to the product of the the area of the diffusion field and the rate of volume production within the film. As shown in the previous sections, the size of the diffusion field supplying material to an isolated whisker increases with decreasing strain rate. Thus, the larger source area partially compensates for the reduced rate of volume production as the strain rate is decreased. The important implication is that if the film is in the mixed relaxation regime, then reducing the rate of volume production (IMC growth) will not result in

a proportional reduction in the whisker growth rate.

4.3.4 *Effect of different whisker mechanisms*

We conclude the discussion of the FEA results by examining how the three mechanisms described in Section 4.1 affect the calculated whisker growth velocities. Results of four simulation series are plotted in Figure 4.10 corresponding to a whisker with horizontal root grain boundary, a whisker with a pyramidal set of root grain boundaries, and two cases in which the whisker grain has lower yield strength than the surrounding film. The differences due to the choice of mechanism are relatively small, with the exception of the soft grain case with small yield strength contrast. The weak grain mechanism is discussed in greater detail below.

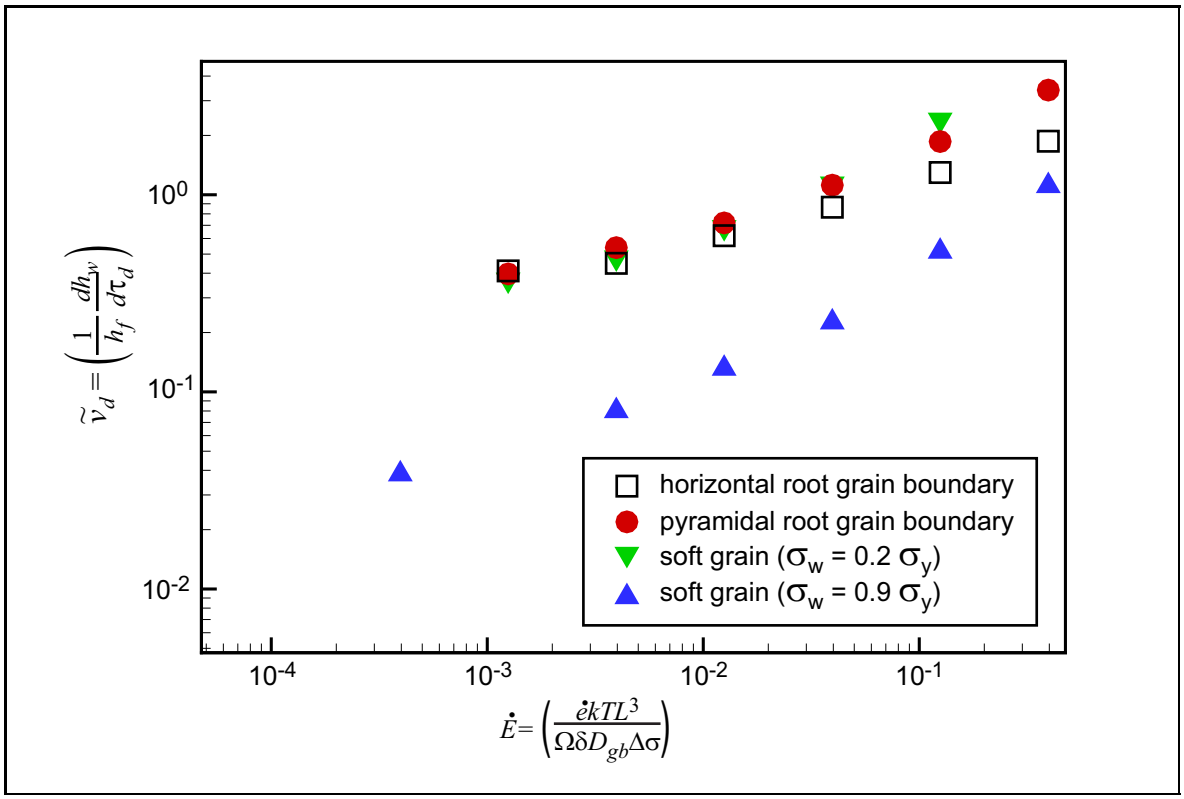

Figure 4.10: Comparison of predicted whisker growth velocities for four different whisker mechanisms.

Focusing on the three similar series of results, note that the differences among them are more pronounced at high strain rates and that they appear to converge at low strain rates. This can be explained by considering the radius of the diffusion field relative to the radius of the whisker. At high strain rates the size of the diffusion field is comparable to the size of the whisker, which is also the grain size of the film. Since diffusion is restricted to the grain boundary network, differences in the geometry of the grain boundary network in the immediate neighborhood of the whisker will influence the net rate of material transport. At low strain rates the diffusion field is large relative to the size of the whisker and also relative to the characteristic length scale of the grain boundary network. Details of the grain boundary network in the neighborhood of the whisker, therefore, exert a much smaller influence on the overall rate of transport.

The differences in whisker growth velocity between the two soft grain cases reflect differences in the driving force. In the root boundary cases, the whisker is essentially stress-free and the magnitude of driving force for diffusion is set by the yield stress of the surrounding Sn. In the case of a soft grain embedded in a stronger matrix, the magnitude of the driving force is set by the *difference* in yield strength between the whisker grain and the surrounding film.

What is most notable about the soft grain simulations is that they predict whisker growth velocities comparable to those predicted by the mechanisms that suppose a stress-free whisker. While the largest yield strength contrast examined, $\sigma_w = 0.2\sigma_y$, may be physically unrealistic, a yield strength contrast of $\sigma_w = 0.9\sigma_y$ could reasonably result from an anomalously-oriented Sn grain in a film with strong preferred crystallographic orientation. Even with this small stress difference of only 1.5 MPa between the whisker and surrounding film, appreciable whisker growth velocities are predicted.

We finish the discussion of whisker growth mechanisms by examining the effect of grain boundary sliding resistance on whisker growth rate. Figure 4.11 compares whisker growth velocities from five series of calculations performed with values of S spanning five orders of magnitude. Within the range of values tested, only the smallest caused appreciable slowing of whisker growth. The differences that are observed are more pronounced at higher strain rates, reflecting greater viscous drag across the model grain boundaries with larger sliding velocities. We also note that grain boundary sliding resistance has no effect on whisker growth rate in the whisker-dominated relaxation regime.

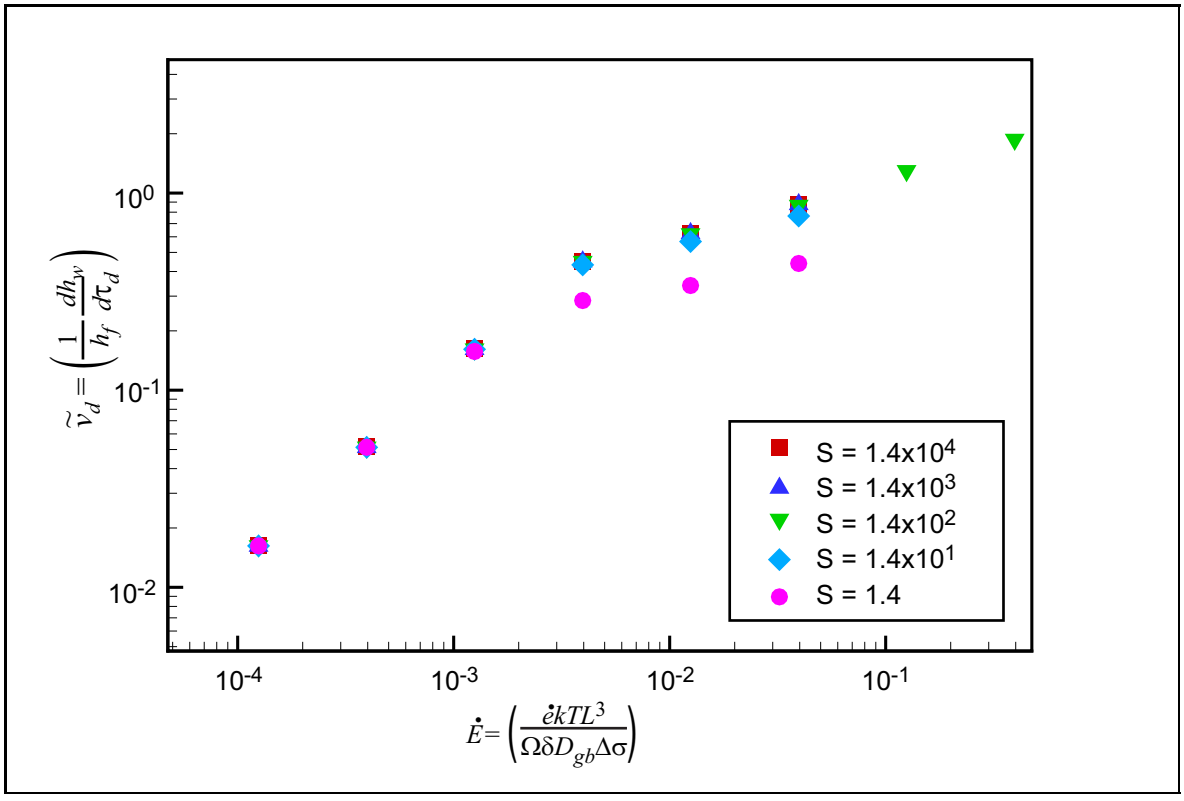

Figure 4.11: Effect of grain boundary sliding resistance on calculated whisker growth velocities.

It is difficult, however, to assess how realistic these values are, as no experimental measurements of grain boundary sliding viscosity could be found for Sn. The value

we used was based on a model for grain boundary sliding presented in Bower and Wininger (2004). In this model the dimensionless parameter $S = 8(L/r)^2$ where L is grain boundary length and r is a characteristic length associated with grain boundary roughness. The choice of r is somewhat arbitrary, and we select a value of η_0 such that $S = 140$ and $(r/L) = 0.24$, which is consistent with the value used by Bower and Wininger (2004). For the smallest value of $S = 1.4$, the corresponding ratio $(r/L) = 2.4$, implying that the characteristic roughness of the grain boundary is 2.4 times greater than the characteristic grain boundary length. Without experimental measurements, however, we can only conclude that grain boundary sliding resistance has very little effect on whisker growth for values of S greater than about 10.

Finally we note that the effect of grain boundary sliding resistance should be greatest for the horizontal root boundary whisker mechanism examined here. Lower sliding velocities relative to the rate of whisker growth are expected for the other two geometries considered, as described in Section 4.1. We therefore expect lower sensitivity to grain boundary sliding for the other two whisker mechanisms.

4.3.5 Correlation between $\dot{e}^*$ and IMC growth rate

In order to compare whisker growth velocities predicted by the FEA models with experimental measurements it is necessary to correlate the uniform volumetric strain imposed in the models with strain generated by IMC growth. As a limiting case, assume that all the excess volume generated by IMC growth is distributed uniformly through the Sn. For a given rate of IMC growth, the associated volumetric strain rate is then:

$$\dot{e} = \frac{d}{dt}\left(\frac{\Delta V}{V_{Sn}}\right) = \left(\frac{1}{A}\frac{dV_{imc}}{dt}\right)\left(\frac{v_{imc} - v_{Sn}}{v_{imc}}\right)\left(\frac{1}{h_{Sn}}\right) = \left(\frac{0.31}{h_{Sn}}\right)\left(\frac{1}{A}\frac{dV_{imc}}{dt}\right) \quad (4.2)$$

where v_α is the specific molar volume of species α, h_{Sn} is the thickness of the Sn film and $(1/A)(dV_{imc}/dt)$ is the normalized IMC growth rate which is measured experimentally.

Not all the excess volume generated by IMC growth, however, is distributed through the film by grain boundary diffusion. Some fraction is accommodated by local plastic deformation around the IMC particles. A more accurate estimate of the fraction of IMC volume contributing to whisker growth has been made by explicitly modeling the growth of discrete IMC particles in a whisker growth FEA calculation. Because of the large computational cost discussed in Section 4.2, a single whisker growth calculation was performed for a model cell with $(A_{cell}/A_w) = 56$. For a constant IMC growth rate of $\left(\frac{1}{A}\frac{dV_{imc}}{dt}\right) = 4.7 \times 10^{-13}$ m/s, the computed whisker growth rate was $\left(\frac{dh_w}{dt}\right) = 1.30 \times 10^{-12}$ m/s. Note that a relatively slow IMC growth rate was chosen so that strain relaxation in the model is in the whisker-dominated regime. Correlating the whisker velocity obtained from the discrete IMC particle model with the velocities plotted in Figure 4.9, a uniformly applied volumetric strain rate of $\dot{e} = 1.9 \times 10^{-8}$ 1/s is found to produce the same whisker growth rate. Using values corresponding to the same whisker growth velocity, the applied volumetric strain rate in the whisker growth models can be correlated with the rate of IMC particle growth through the relation:

$$\dot{e} = \alpha \left(\frac{0.31}{h_{Sn}}\right)\left(\frac{1}{A}\frac{dV_{imc}}{dt}\right) \tag{4.3}$$

where the factor (0.31) is the fractional volume increase per unit IMC volume for the transformation reaction. For the values given above, the proportionality constant α is found to be 0.26. This implies that a maximum of approximately 25% of the *excess* volume generated by IMC growth can be removed by whisker growth. Equation 4.3 with $\alpha = 0.25$ was used to calculate the estimated IMC growth rates shown on the upper axes in Figures 4.6, 4.9 and 4.8.

4.4 Discussion

Finite element analysis of the model system provides important insight into the kinetics of whisker growth and the mechanisms that control it. The results reveal two distinct kinetic regimes for whisker growth. In one regime, strain in the film is relaxed by a combination of plastic deformation within the Sn grains and whisker growth, while in the other regime whisker growth is the dominant relaxation mechanism. In the regime of mixed relaxation, a stress gradient of fixed radius defining the diffusion field develops around each whisker. Because the stress is maintained below the yield stress within the diffusion field, there is no intra-granular plastic flow in this region. Therefore, the rate of volume removal by the whisker must exactly balance the rate of volume production within the diffusion field. This balance, governed by the rate of diffusion relative to the rate of strain generation, determines the size of the diffusion field. As strain rate decreases, the size of the diffusion field increases. As a consequence, whisker growth rate varies only weakly with strain rate. For a given whisker density there is a critical value of strain rate at which the diffusion radius is half the mean spacing between whiskers. Below this strain rate, the diffusion fields of neighboring whiskers overlap. In this whisker-dominated relaxation regime the stress in the film is maintained below the yield stress and whisker growth accounts for all strain relaxation.

With this picture in mind we now consider the implications for whisker growth in the real Sn-Cu system, where both the whisker density and the rate of strain generation vary with time. IMC growth, which generates strain within the Sn, is fastest immediately after the Sn is deposited on Cu then slows over time. Whiskers, on the other hand, do not typically begin to nucleate until several hours to several days after deposition. After nucleation begins, the whisker density then increases monotonically at a rate that decreases with time, as shown in Figure 1.3.

At the earliest stages, before whiskers begin to nucleate, all of the strain generated by IMC growth must be relaxed by plastic flow within Sn grains. This is precisely the situation that was modeled in Chapter 3 where grain boundary diffusion was shown to play an important role in redistributing strain, eventually bringing the film to yield through the entire thickness. It is interesting to note that the first emergence of whiskers appears to coincide with the film stress reaching its steady state value. This may suggest that plastic flow within Sn grains plays a role in whisker nucleation.

During this early stage of evolution we can infer that the system would initially fall somewhere in the "mixed relaxation" field in the lower right quadrant of the phase diagram in Figure 4.6. It would then follow a trajectory toward the boundary defining the whisker-dominated relaxation field as the IMC growth rate decreases and whisker density increases. To make more quantitative predictions about how the system evolves we need to consider realistic values for IMC growth rates and whisker densities.

From examination of the IMC growth curves presented in Figure 1.3 and other published IMC growth data [Zhang *et al.* (2005), Reinbold (2007), Jadhav *et al.* (2010)], IMC growth rates normalized by the volume of the Sn film $\left(\frac{1}{Ah_{Sn}}\frac{dV_{imc}}{dt}\right)$ are found to range from approximately 5×10^{-6}/s to 1×10^{-7}/s during the first 100 hours of growth, eventually slowing to approximately 1×10^{-8}/s after 1 month. Measured whisker densities plotted in Figure 1.3 increase to approximately 300/mm^2 by 5 days after plating for the 1.45 μm thick film, and 150/mm^2 and 100/mm^2 for the 2.9 μm and 5.8 μm films, respectively. When these whisker densities are normalized by the cross-sectional area of the whiskers, the normalized whisker densities range from $N = 4\times10^{-4}$ to 8×10^{-4}. Tu (1973) reports whisker densities of 10/mm^2 to 100/mm^2 , which normalize to $N \approx 3\times10^{-5}$ to 3×10^{-4}. Based on these data, a reasonable estimate for whisker density within the first 5 days after plating is in the range of tens

to hundreds of whiskers/mm^2 ($N \approx 10^{-4}$ to 10^{-3}). The whisker density continues to increase over time, but based on the rates of increase seen in Figure 1.3, maximum whisker densities should remain less than 2 to 4 times the values measured at 100 hours.

We now consider the model predictions within these ranges of whisker density and IMC growth rate. To facilitate comparison with experimental values, dimensional values of whisker growth velocity corresponding to a 2 μm thick Sn film are shown on the right-hand axis of Figure 4.9. We find that the model predicts whisker growth rates between 1×10^{-11}/s and 3×10^{-11}/s over the full range of experimentally measured IMC growth rates. As a point of reference, 10^{-11}m/s $\approx 1\mu$m/day. This is in good agreement with measured average whisker growth rates of 1×10^{-11}m/s to 2×10^{-11}m/s [Tu (1973), Lee and Lee (1998), Hutchinson *et al.* (2004)]. These measurements, however, are averages found by dividing the length of a whisker by the total time since deposition (or whisker nucleation). Recent time-series SEM images [Jadhav (2010); personal communication], however, reveal that the growth of individual whiskers is often intermittent, with periods of constant velocity growth followed by periods of no growth. During the periods of active growth, which typically last from several hours to several days, whisker growth velocities of 5×10^{-11}m/s to 20×10^{-11}m/s have been measured. While these measurements are up to an order of magnitude greater than those predicted by the model, they do exhibit the qualitative behavior predicted by the model. These measurements have been made within a few days of deposition, when IMC growth rates are expected to high and also changing most rapidly. Real-time SEM observation of the whisker growth, however, reveals that individual whiskers often maintain a relatively constant growth velocity over a period of several days, consistent with the predicted weak dependence of whisker growth rate on IMC growth rate.

In regard to the disparity in the magnitude of the predicted whisker growth velocity, note that the dimensional velocity values (right-hand axis) shown in 4.9 are calculated from the non-dimensional velocity, $\tilde{v}_d$. The dimensional velocity scales with $\tilde{v}_d$ as $(1/\tau_d)$ where $\tau_d = \left(\frac{kTL^3}{\Omega\delta D_{gb}\Delta\sigma}\right)$ is the diffusion time scale. Thus, our model would predict greater dimensional whisker growth velocities if a larger value for D_{gb} is assumed. A five- to ten-fold increase in the assumed rate of diffusion through the grain boundary network would be required for the model predictions to agree with the real-time whisker growth velocity measurements. However, it should also be noted that this would also increase the diffusion radius at a given strain rate. Thus our model would predict that whiskers would interact with one another at lower densities.

In addition to whisker growth velocity, we also want to know how strain relaxation is partitioned within the Sn film. This is governed by the whisker density in relation to the strain rate. During the first few days after plating, the normalized whisker density rises from zero to a little less than $N = 10^{-3}$, while the normalized IMC growth rate simultaneously decreases from about 10^{-6}/s to 10^{-7}/s. Considering the phase diagram in Figure 4.6, we see that the system begins well below the phase boundary, in the mixed relaxation regime. However, for whisker densities and strain rates measured five days after plating, the system falls on or near the phase boundary, indicating transition to the whisker-dominated relaxation regime. Unfortunately, given the idealizations and approximations inherent in the model, the uncertainty in the location of the phase boundary is too great to predict with confidence whether the system evolves to the whisker-dominated relaxation regime. We can conclude, however, that the system must begin in the mixed relaxation regime and follow a trajectory toward whisker-dominated behavior. As the system evolves, the partitioning of strain relaxation shifts toward increasing relaxation by whisker growth. If relaxation were whisker-dominated, the model predicts that the stress in the film would

drop below the yield stress and scale with the rate of IMC growth. However, this is not observed experimentally, suggesting that strain relaxation remains in the mixed regime. The intermittent quality of whisker growth observed experimentally may partially explain why the transition to whisker-dominated relaxation does not appear to occur at the expected whisker density. The density of *active* whiskers determines the kinetic behavior. If a significant fraction of the whiskers are inactive, then the observed whisker density will not reflect the number of whiskers relaxing strain at that particular time.

Despite the inconsistencies identified above, the model presented here is in excellent quantitative agreement with published whisker growth velocities and with the predictions of previous models. This is particularly significant since the kinetic behavior in the model arises naturally from the interaction among competing processes. We also note that the model is based on a small number of well-supported assumptions about the constitutive behavior of the Sn and the loading in the system.

4.5 Conclusions

Whisker growth has long been recognized as a mechanism for the relaxation of stress in Sn films, and stress-driven grain boundary diffusion is typically assumed to be the primary mode of long-range transport. For Sn films on Cu, stress generation is generally attributed to the growth of IMC within the Sn and recent experiments find evidence of dislocation-mediated plastic flow within the Sn grains surrounding the IMC. A number of diffusion models have been proposed in the literature to explain and quantify whisker growth kinetics, but none have included the effects of strain generation or plastic flow within Sn grains. In this chapter we present a finite element model for whisker growth that for the first time includes all of these behaviors. The resulting kinetic relations that emerge from the model reveal behavior more complex

than has previously been appreciated. We summarize the model predictions and their implications below.

1. Two distinct kinetic regimes are identified, corresponding to how strain relaxation is partitioned between local plastic flow within grains and long-range transport to whiskers.

2. In the whisker-dominated relaxation regime, whisker growth velocity varies in direct proportion with IMC growth rate.

3. In the mixed relaxation regime, whisker velocity shows weak (less than linear) dependence on the rate of strain generation. In this regime, reducing the IMC growth rate will not significantly reduce whisker growth velocities.

4. The size of the diffusion field surrounding the whisker is fully determined by the balance between the rate of strain generation and the rate of diffusive transport. For a material system with fixed diffusivity, the diffusion radius decreases with increasing rate of strain generation.

5. The self-limiting size of the diffusion field, independent of whisker density, helps explain how a small background stress can produce sufficient driving force for whisker growth. The restricted size of the diffusion field maintains a high stress gradient, even for small stress at the outer boundary.

6. For real Sn-Cu systems the model predicts that strain relaxation will be dominated by plastic flow immediately after plating. As the system evolves, whisker growth is responsible for an increasing fraction of the total strain relaxation. Our model predicts that relaxation should become whisker-dominated at the slowest rates of IMC growth and highest whisker densities observed. Stress measurements, however, suggest that the system remains in the mixed relaxation

regime. This may indicate that the observed whisker densities overestimate the number of whiskers actively relaxing strain at a given time.

7. While the model does not address the issue of whisker nucleation, it does show that any localized feature within the film that relaxes stress more effectively than the surrounding film will drive diffusion toward that point. Whether such features are created during deposition or develop as the film evolves will need to be resolved by experiment.

8. Whisker growth rates predicted by the model are in excellent agreement with reported average growth rate measurements. This is significant, given that the kinetic behavior in the model arises naturally from the interaction among competing processes. Recent real-time SEM observation of actively growing whiskers, however, indicate growth velocities up to an order of magnitude higher than those predicted. Greater diffusivity within the grain boundary network could account for these faster velocities.

In the next chapter, a mathematical description is presented that allows further systematic study of whisker kinetics, including the influence of more realistic rate-dependent material behavior and the effect of thermal cycling.

Chapter 5

Whisker Growth Kinetics: Analytical Models

The essential features of the behavior observed in the FEA simulations can be captured in an axisymmetric boundary value problem. A number of similar axisymmetric models of whisker growth have been proposed by previous authors [Chaudhari (1974), Lindborg (1976), Tu (1994), Hutchinson *et al.* (2004), Tu and Li (2005), Nakadaira *et al.* (2007)]. In this chapter we present a mathematical description of whisker growth that extends the prior models by 1) accounting for strain generation within the film and 2) accounting for strain relaxation by intra-granular plastic flow. In addition to perfectly plastic behavior assumed in the FEA, we also pose and solve the problem for material with rate-dependent viscoplastic flow with power-law sensitivity. This empirical constitutive law has been shown experimentally to accurately describe the behavior of Sn thin films.

The problem is first posed for a material with rate-independent elastic-perfect plastic constitutive behavior, and an analytical solution is presented. The problem is then posed for a material with rate-dependent plastic deformation governed by a power-law von Mises flow potential. The resulting non-linear partial differential

equation is solved by numerical techniques. Results from both model descriptions are compared. We conclude with an application of our model to the kinetics of whisker growth driven by thermal cycling.

5.1 Problem definition

As demonstrated by the FEA simulations, transport of material to a whisker is governed by the balance between strain generation and strain relaxation. Making a number of simplifying assumptions, the problem can be posed as an axially symmetric boundary value problem as follows.

We consider a thin film of thickness h_f bonded to a rigid substrate which prevents lateral displacement. The film is treated as a linear elastic continuum that can also deform by plastic flow or stress-driven volume diffusion. Extending through the thickness of the film is a cylindrical "whisker" grain of radius a. Stress relaxation in the whisker grain is enhanced relative to the surrounding film. For simplicity we assume that the whisker grain can support no stress so that the surface $r = a$ remains stress free. We also assume that the whisker acts as a perfect sink for volume with all material passing across the boundary $r = a$ being extruded from the film as a whisker of constant cross-sectional area. The geometry of the problem is shown in Figure 5.1.

Strain is generated continuously in the film at rate $\dot{\varepsilon}^*$ where ε^* is a stress-free transformation strain. Strain is relaxed by a combination of elastic and plastic deformation and volume diffusion to the whisker grain. Diffusion along the network of vertically-oriented grain boundaries in the polycrystalline Sn film is approximated as bulk diffusion with effective diffusivity defined as:

$$D = \alpha \left(\frac{\delta}{a} \right) D_{gb} \tag{5.1}$$

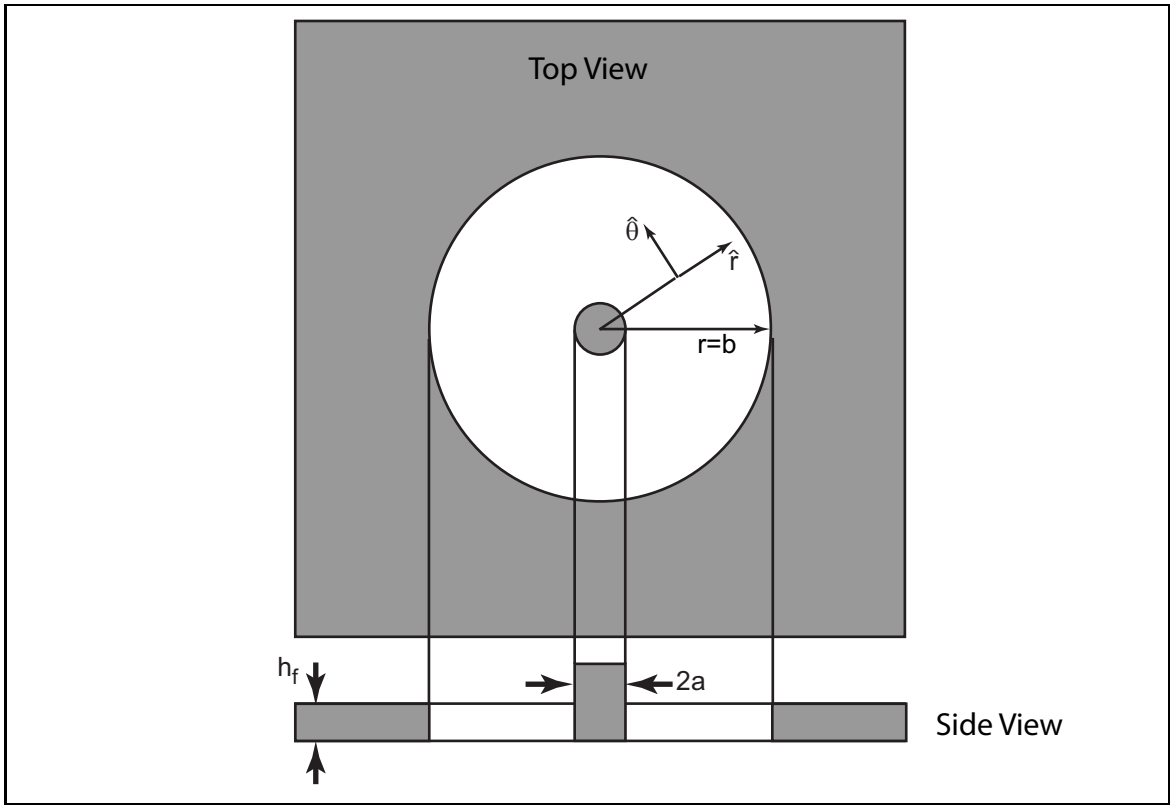

Figure 5.1: Geometry of the problem. The region $r < a$ is the "whisker grain" which, by an unspecified mechanism, is able to relax stress more effectively than the surrounding film.

where δ is the nominal grain boundary thickness and D_{gb} is the grain boundary diffusivity. The radius of the whisker, a, is a characteristic length taken to represent the grain size of the polycrystalline Sn film. The proportionality constant α accounts for the geometry of the grain boundary network and is of order 1.

Due to the lateral constraint imposed by the substrate, the in-plane components of total strain in the film must be zero at every material point. In rate form, the balance equation is:

$$\dot{\varepsilon}^{total} = \dot{\varepsilon}^{e} + \dot{\varepsilon}^{p} + \dot{\varepsilon}^{d} + \dot{\varepsilon}^{*} = 0 \tag{5.2}$$

where $\dot{\varepsilon}^{e}$ is the elastic strain rate, $\dot{\varepsilon}^{p}$ is the plastic strain rate, $\dot{\varepsilon}^{d}$ is the strain rate

resulting from diffusion of atoms, and $\dot{\varepsilon}^*$ is the imposed stress-free strain rate. Equation 5.2 is the fundamental balance law defining the problem.

The problem is axisymmetric about the central axis of the whisker and we adopt a cylindrical coordinate system. A state of plane stress is assumed and field quantities have no z dependence. Both the applied stress-free strain and the strain due to the diffusion of atoms are spherical which produces an equibiaxial stress state under the plane stress assumption. The problem can be expressed in terms of a single stress variable with radial dependence only:

$$\sigma_{rr} = \sigma_{\theta\theta} \equiv \sigma(r)$$

$$\sigma_{zz} = 0$$

In order to apply the strain rate balance (5.2), each of the strain rates must be expressed as a function of stress through an appropriate contitutive relation. For equibiaxial plane stress the linear elastic stress-strain relation is

$$\dot{\varepsilon}^e = \frac{\dot{\sigma}}{M} \tag{5.3}$$

$$M = \frac{E}{(1-\nu)} \tag{5.4}$$

where M is the biaxial modulus, E is Young's modulus and ν is Poisson's ratio.

To derive the stress-strain relation for diffusion, we first recognize that the rate of volumetric strain due to diffusion is given by the divergence of the volume flux:

$$\dot{e}^d = 3\dot{\varepsilon}^d = -\nabla\vec{j}_v \tag{5.5}$$

where $\dot{e}^d$ is the volumetric strain rate and the volume flux, $\vec{j}_v$, follows from Fick's first

law:

$$\vec{j}_v = -\frac{D}{kT}\nabla\mu \tag{5.6}$$

$$= +\frac{D\Omega}{kT}\nabla\sigma. \tag{5.7}$$

In going from (5.6) to (5.7), we note that the effective bulk diffusion in the model is meant to approximate diffusion along a network of vertically-oriented grain boundaries. Following the description of grain boundary diffusion given in Section 2.3.1, we define the chemical potential for diffusion, μ, as $\mu = -\Omega\sigma_n$, where σ_n is the normal stress across the grain boundary, and recognize that σ_n is equal to the equibiaxial stress, σ. Combining (5.5) and (5.7) gives

$$\dot{\varepsilon}^d = -\frac{1}{3}\frac{D\Omega}{kT}\nabla^2\sigma. \tag{5.8}$$

In polar coordinates the relation connecting stress and the rate of strain due to mass diffusion is

$$\dot{\varepsilon}^d = -\frac{1}{3}\frac{D\Omega}{kT}\left(\frac{\partial^2\sigma}{\partial r^2} + \frac{1}{r}\frac{\partial\sigma}{\partial r}\right). \tag{5.9}$$

In the following two sections we develop mathematical models for whisker growth assuming two different constitutive relations for plastic flow.

5.2 Steady-state perfectly plastic model

Here we develop the governing equation for steady state diffusion to a whisker, assuming rate-independent elastic-perfectly plastic behavior within the Sn. The model system is analogous to the one studied via FEA in Chapter 4.

We begin with the strain balance equation, (5.2), and note that at steady state the elastic strain rate must vanish. This follows from the fact that only the elastic strain

contributes to the stress, which must remain fixed at steady state. As discussed in the previous chapter, for perfectly plastic behavior the film is divided into two distinct regions separated by a sharp boundary. In an annular region surrounding the whisker a stress gradient develops which drives diffusion toward the whisker. Beyond this region, the biaxial stress remains fixed at the yield stress as the film undergoes continuous plastic shearing. If the radius of the annular diffusion field is b, then the strain rate balance in the two regions becomes:

$$\dot{\varepsilon}^* + \dot{\varepsilon}^d = 0 \qquad (a \leq r < b) \tag{5.10}$$

$$\dot{\varepsilon}^* + \dot{\varepsilon}^p = 0 \qquad (r \geq b) \tag{5.11}$$

Combining (5.10) and (5.9) gives an ordinary differential equation for the steady state stress field in the region surrounding the whisker:

$$\frac{D\Omega}{kT}\left(\frac{\partial^2\sigma}{\partial r^2} + \frac{1}{r}\frac{\partial\sigma}{\partial r}\right) = \dot{e}^* \tag{5.12}$$

$$a \leq r < b \tag{5.13}$$

$$\sigma(a) = -\sigma_w \tag{5.14}$$

$$\sigma(b) = -\sigma_y \tag{5.15}$$

$$\left.\frac{\partial\sigma}{\partial r}\right|_{r=b} = 0 \tag{5.16}$$

where σ_w is the yield stress of the whisker and σ_y is the yield stress in the surrounding film. The volumetric applied strain rate, $\dot{e}^* = 3\dot{\varepsilon}^*$, is substituted above to facilitate comparison with the results from Chapter 4. The third boundary condition, (5.16), imposes zero flux across the outer boundary and is used to determine b. For the

following choice of dimensionless parameters,

$$\begin{aligned} \xi &= \left(\frac{r}{a}\right) & \beta &= \left(\frac{b}{a}\right) \\ q &= \left(\frac{\sigma - \sigma_w}{\Delta\sigma}\right) & \Delta\sigma &= (\sigma_y - \sigma_w) \end{aligned}$$

the boundary value problem can be posed in non-dimensional form as:

$$\left(\frac{\partial^2 q}{\partial \xi^2} + \frac{1}{\xi}\frac{\partial q}{\partial \xi}\right) = \left(\frac{kTa^2\dot{e}^*}{D\Omega\Delta\sigma}\right) \equiv \dot{E} \tag{5.17}$$

$$1 \leq \xi < \beta \tag{5.18}$$

$$q(1) = 0 \tag{5.19}$$

$$q(\beta) = -1 \tag{5.20}$$

$$\left.\frac{\partial q}{\partial \xi}\right|_{\xi=\beta} = 0 \tag{5.21}$$

Note that the solution depends the dimensionless parameter, $\dot{E}$, that expresses the rate of strain generation relative to the rate of strain relaxation by diffusion. The analytical solution to (5.17–5.20) is:

$$q(\xi) = \left(\frac{\ln(\xi)}{\ln(\beta)}\right) - \frac{\dot{E}}{4}\left[\xi^2 - (\beta^2 - 1)\left(\frac{\ln(\xi)}{\ln(\beta)}\right) - 1\right]. \tag{5.22}$$

To determine the radius of the diffusion field, we enforce the zero flux condition at $\xi = \beta$. Setting the derivative with respect to ξ equal to zero at $\xi = \beta$ to yields the following transcendental equation which can be solved numerically for β:

$$\left[\beta^2(2\ln(\beta) - 1) + 1\right]\dot{E} - 4 = 0. \tag{5.23}$$

To find the whisker growth velocity we take advantage of the fact that there is no plastic shearing within the diffusion field, $1 \leq \xi < \beta$. Therefore, at steady state, the

volume of material removed by the whisker must balance the volume of new material generated within the diffusion field. The whisker velocity is calculated by dividing the rate of volume production in the region $1 \leq \xi < \beta$ by the cross-sectional area of the whisker. In dimensional form:

$$\frac{dh_w}{dt} = \frac{\dot{e}^* h_f \pi b^2}{\pi a^2} = \dot{e}^* h_f \beta^2. \tag{5.24}$$

Note that the volume produced within the whisker is included in the total volume. To non-dimensionalize the whisker growth rate, note that there are two natural time scales in the problem, one related to the rate of strain generation, the other to the rate of diffusion:

$$\tau_e = \left(\frac{1}{\dot{e}^*}\right) \qquad \tau_d = \left(\frac{kTa^2}{D\Omega\Delta\sigma}\right) \tag{5.25}$$

Normalizing whisker height by the strain generation time scale gives:

$$\frac{d\tilde{h}_w}{d\tau_e} = \frac{d\tilde{h}_w}{de} = \beta^2 \tag{5.26}$$

where $\tilde{h}_w = (h_w/h_f)$. This rate shows the change in whisker length per increment of applied strain and reflects the area of the annular region supplying material to the whisker. Normalizing by the characteristic diffusion time scale, τ_d, yields

$$\frac{d\tilde{h}_w}{d\tau_d} = \dot{E}\beta^2. \tag{5.27}$$

Since the time scale, τ_d, depends only on temperature and material parameters, $(d\tilde{h}_w/d\tau_d)$ is directly proportional to the dimensional whisker velocity for a given material system at fixed temperature. Results of this model are discussed in Section 5.4.

5.3 Rate-dependent plasticity model

We now pose the same problem for a material that can deform by rate-dependent plastic flow with power-law stress sensitivity. The plastic strain rate is given by

$$\dot{\varepsilon}_{ij}^{p} = \dot{\varepsilon}_{0}^{p} \exp\left(\frac{-Q}{kT}\right)\left(\frac{\sigma_e}{\sigma_0}\right)^{m}\left(\frac{3}{2}\frac{S_{ij}}{\sigma_e}\right). \tag{5.28}$$

$$\sigma_e = \sqrt{\frac{3}{2}S_{ij}S_{ij}} \tag{5.29}$$

$$S_{ij} = \sigma_{ij} - \frac{1}{3}\sigma_{kk}\delta_{ij} \tag{5.30}$$

where S_{ij} is the deviatoric stress, σ_e is the von Mises equivalent stress, and $\dot{\varepsilon}_0^p$, Q, and m are material parameters that define the characteristic strain rate, activation energy, and stress sensitivity, respectively. We assume there is no hardening so the nominal yield stress, σ_0, is constant. At fixed temperature the exponential term can be included within the constant $\dot{\varepsilon}_0^p$. For an equibiaxial stress state with magnitude σ, $S_{rr} = S_{\theta\theta} = (\sigma/3)$ and $\sigma_e = |\sigma|$. The plastic strain rate is also equibiaxial, so we can drop the subscripts and express the in-plane plastic strain rate as

$$\dot{\varepsilon}^{p} = \dot{\varepsilon}_{0}^{p}\left[\frac{|\sigma|}{\sigma_0}\right]^{m}\frac{1}{2}\frac{\sigma}{|\sigma|}. \tag{5.31}$$

Substituting this plastic strain rate into the strain balance equation, (5.2), along with the expressions for $\dot{\varepsilon}^e$, $\dot{\varepsilon}^d$, and $\dot{\varepsilon}^*$ yields the following non-linear partial differential equation for $\sigma(r)$

$$\frac{1}{M}\frac{\partial\sigma}{\partial t} - \frac{1}{3}\left(\frac{D\Omega}{kT}\right)\left[\frac{\partial^2\sigma}{\partial r^2} + \frac{1}{r}\frac{\partial\sigma}{\partial r}\right] + \dot{\varepsilon}_0^p\left[\frac{|\sigma|}{\sigma_0}\right]^{m}\frac{1}{2}\frac{\sigma}{|\sigma|} + \dot{\varepsilon}^* = 0 \tag{5.32}$$

The boundary condition on the inner boundary is set by the stress in the whisker grain. For simplicity, we assume the whisker supports no stress so that $\sigma(a) = 0$. More

complex boundary conditions could be imposed, such as allowing the stress within the whisker root to vary with the rate of volume flux, but these are not considered here.

To set the outer boundary condition, we assume a finite density of equally spaced whisker grains. If the fraction of the total film area occupied by whisker grains is N, then the mean spacing between whiskers is $(a/\sqrt{N})$. The flux across the surface $r = (a/\sqrt{N})$ must therefore be zero, assuming identical behavior for all of the whiskers in a periodic array. This provides the second boundary condition, $\frac{\partial \sigma}{\partial r} = 0$ at $r = (a/\sqrt{N})$.

The most physically realistic initial condition would be to assume a state of constant equibiaxial stress corresponding to the stress in the film at the time of whisker nucleation. To find the magnitude of this stress, imagine the system at steady state with no strain relaxation due to whisker growth. All strain must be relaxed by plastic flow, implying $\dot{\varepsilon}^p = -\dot{\varepsilon}^*$. For plastic strain rate given by (5.31), the magnitude of the resulting steady state stress is

$$\sigma_\infty = \left[\frac{2\dot{\varepsilon}^*}{\dot{\varepsilon}_0^p}\right]^{1/m} \sigma_0. \tag{5.33}$$

This sets the characteristic scale for stress in the problem. The time required for the system to reach this stress defines the characteristic time scale

$$t_0 = \left(\frac{\sigma_\infty}{M\dot{\varepsilon}^*}\right), \tag{5.34}$$

and the radius of the whisker defines the characteristic length scale. We use these scales to define the non-dimensional variables

$$\xi = \left(\frac{r}{a}\right) \qquad \tau = \left(\frac{t}{t_0}\right) \qquad q = \left(\frac{\sigma}{\sigma_\infty}\right) \tag{5.35}$$

and cast (5.32) and the associated initial and boundary conditions in the following non-dimensional form

$$\frac{\partial q}{\partial \tau} - \Gamma\left(\frac{\partial^2 q}{\partial \xi^2} + \frac{1}{\xi}\frac{\partial q}{\partial \xi}\right) + |q|^m \frac{q}{|q|} + 1 = 0 \tag{5.36}$$

$$q(0,\xi) = 0 \tag{5.37}$$

$$q(\tau,1) = 0 \tag{5.38}$$

$$\left.\frac{\partial q}{\partial \xi}\right|_{\xi=(1/\sqrt{N})} = 0 \tag{5.39}$$

where

$$\Gamma = \frac{1}{3}\left(\frac{D\Omega\sigma_0}{kTa^2\dot{\varepsilon}^*}\right)\left[\frac{2\dot{\varepsilon}^*}{\dot{\varepsilon}_0^p}\right]^{1/m}. \tag{5.40}$$

Notice that $1/\Gamma$ represents the same ratio as $\dot{E}$, but with $\sigma\Delta$ replaced by σ_∞. A numerical method is required to solve the initial-boundary value problem defined by (5.36-5.39), and a finite element solution has been written for the Matlab computational software.

Prior to examining the numerical results, we consider the steady state solution and show that the boundary value problem describing whisker growth for a material with rate-independent perfectly plastic behavior (5.17–5.21) is a limiting case of rate dependent formulation.

At steady state the partial differential equation reduces to an ordinary differential equation

$$\Gamma\left(\frac{\partial^2 q}{\partial \xi^2} + \frac{1}{\xi}\frac{\partial q}{\partial \xi}\right) - |q|^m \frac{q}{|q|} - 1 = 0 \tag{5.41}$$

$$q(1) = 0 \tag{5.42}$$

$$\left.\frac{\partial q}{\partial \xi}\right|_{\xi=(1/\sqrt{N})} = 0. \tag{5.43}$$

This boundary value problem can be solved numerically using standard solving routines in the Matlab computational software. To connect with the rate-independent model, we take the limit as the rate sensitivity exponent goes to infinity,

$$\lim_{m\to\infty} \Gamma = \frac{1}{3}\left(\frac{D\Omega\sigma_0}{kTa^2\dot{\varepsilon}^*}\right) \tag{5.44}$$

$$\lim_{m\to\infty} |q|^m = \begin{cases} 0 & q < 1 \\ 1 & q = 1 \\ \infty & q > 1. \end{cases} \tag{5.45}$$

Thus $q = 1$ defines a yield surface. Recall that in the annular domain surrounding the whisker in the rate-independent problem, the stress remains below the yield stress, and at the outer boundary $q = -1$. We fully recover the rate-independent formulation (which is also fully expected). We note that in the rate-dependent problem, $(1/\Gamma)$ corresponds to the dimensionless strain-rate, $\dot{E}$, defined for the rate-independent problem and in the FEA.

The only issue remaining is to determine how to compute the whisker growth velocity from the solution to the rate dependent problem, $q(\tau, \xi)$. Unlike in the rate-independent case, here plastic flow and diffusion operate simultaneously at the same material points. We therefore must calculate the whisker velocity from the flux of volume across the cylindrical bounding surface of the whisker. Dividing the rate at which new volume enters the whisker, $(dV/dt) = -\vec{j}_v(2\pi a h_f)$, by the cross-sectional area of the whisker, πa^2, and substituting (5.7) for the volume flux gives the whisker growth velocity in dimensional form,

$$\frac{dh_w}{dt} = -2h_f\left(\frac{D\Omega}{kT}\right)\left.\frac{\partial\sigma}{\partial r}\right|_{r=a} \tag{5.46}$$

In terms of the non-dimensional solution, this is

$$\frac{dh_w}{dt} = -2h_f\dot{\varepsilon}^*\Gamma \left.\frac{\partial q}{\partial \xi}\right|_{\xi=1} \tag{5.47}$$

Finally, dividing the rate of volume accumulation in the whisker by the rate of volume generation within the domain $1 < \xi < (1/\sqrt{N})$ gives the whisker "efficiency"

$$\eta = -\left(\frac{N}{1-N}\right)\Gamma \left.\frac{\partial q}{\partial \xi}\right|_{\xi=1}. \tag{5.48}$$

5.4 Model predictions and discussion

In this section we examine some of the predictions of the two models presented above. The fundamental processes governing the whisker growth-mass transport problem were discussed at length in Chapter 4. The discussion here aims only to highlight new observations. First we would like to verify that the solutions capture the behavior they were intended to replicate. Whisker growth velocities calculated with the rate-independent material model are plotted in Figure 5.2. To produce the dimensional velocities we assumed the same material property values as in the FEA, listed in Table 4.1. The simplified one-parameter model clearly reproduces the kinetic relations found via FEA. This probably speaks more to the idealized nature of the FEA model than the validity of the equations. The ease of computation provided by the mathematical model allows the parameter space to be explored more thoroughly than is feasible with FEA.

With these models we are able to examine the partitioning of strain relaxation between whisker growth and plastic flow in greater detail. The idea of the "phase diagram" indicating the mode of relaxation presented in Figure 4.6 can be extended by plotting the calculated values of the whisker efficiency, η over the space defined

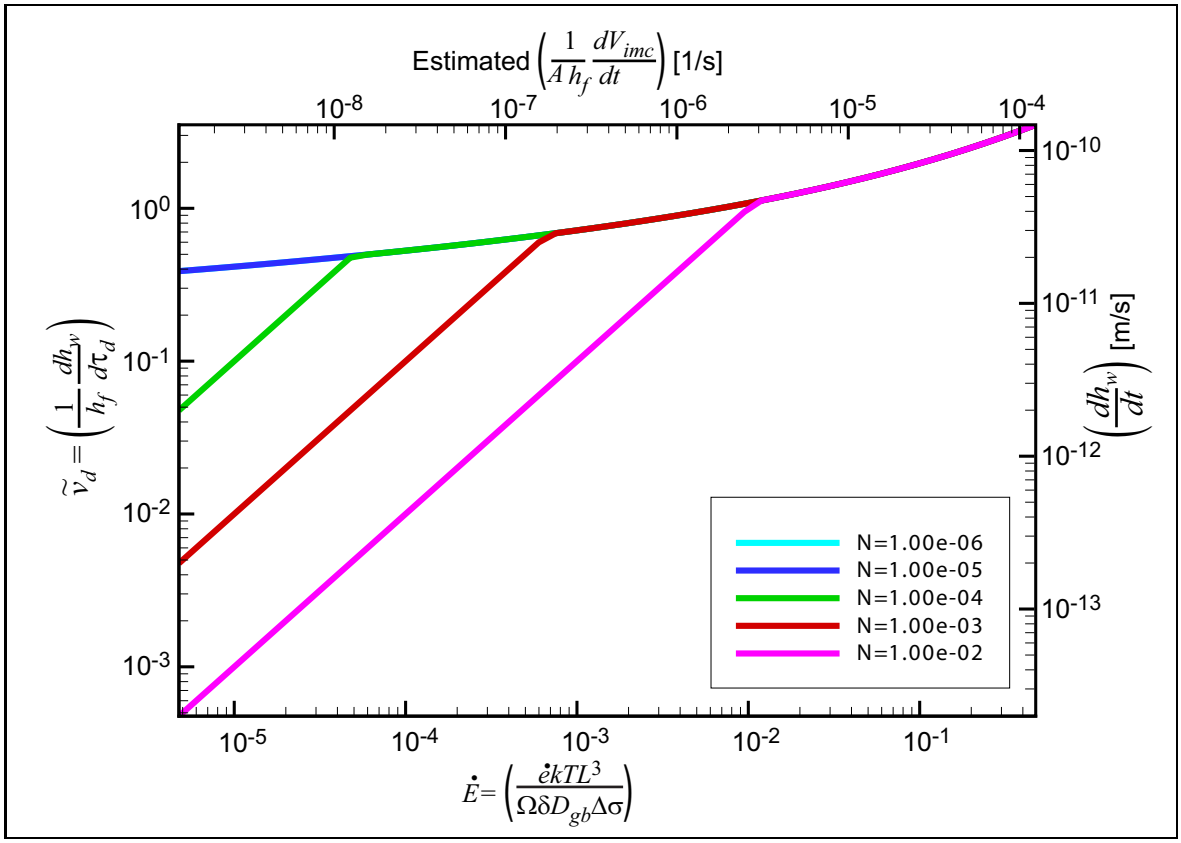

Figure 5.2: Whisker growth velocities predicted by solution of the steady-state boundary value problem for viscoplastic behavior. Perfectly plastic behavior is assumed. Material parameters identical to those used in the FEA in Chapter 3 are used to calculate dimensional values.

by dimensionless strain rate, $\dot{E}$ and whisker density, N. A contour plot of η is provided in Figure 5.3a. We see that the transition from the plastic flow-dominated to the whisker-dominated regimes is relatively sharp, spanning a small band of the parameter space. The shape of the boundary is nearly a straight line on the log-log plot, with slope slightly less than +1. The whisker growth velocity is plotted similarly in Figure 5.3b. This provides the same information as the line plot in Figure 5.2 but reveals the combined effects of whisker density and strain rate more directly. The relationships in this case are straightforward, showing that whisker velocity is entirely determined by the strain rate (vertical color bands) until a critical density is reached.

The effect of rate-dependent plastic flow can be examined as well. Figure 5.4 plots steady state whisker velocities calculated for a material with power-law viscoplastic flow. The results are plotted in dimensional form to allow comparison with the results for rate independent yield behavior. Material parameters measured by Shin and Chason (2009) for creep behavior in thin film Sn were used to generate the dimensional values. The kinetic behavior represented in the whisker velocity plot is qualitatively very similar to that for rate independent yield. The predicted magnitudes, however, are lower by a factor of approximately 10.

Contour plots of the strain partitioning measure, η, and the maximum stress in the film, are plotted in Figure 5.5. The maximum stress is the stress calculated at the mid-distance between whiskers, $\xi = 1/\sqrt{N}$ (not the parameter, σ_∞). Notice that the maximum compressive stress decreases sharply in a band that cuts diagonally across the plot. Somewhat surprisingly, the fraction of relaxation by whisker growth does not correlate strongly with the change in stress. The most striking feature of the plot in Figure 5.5a) is its near uniform blue color, indicating that whisker growth accounts for less than 10% of the total strain relaxation. Unlike the situation with a perfectly plastic material where strain relaxation modes are strictly segregated to distinct regions in the film, for the rate-dependent material, plastic flow occurs throughout the film. Thus plastic flow accounts for a much greater portion of the relaxation.

We also note that a well-defined relaxed region develops around the whisker for the rate-dependent material, similar to that observed for the rate-independent material. Figure 5.6 shows steady-state stress profiles across the domain $1 < \xi < \beta$ for different values of $(1/\Gamma)$. At high strain rate the stress gradient defining the diffusion field of the whisker is limited to a radius much smaller than half the whisker separation.

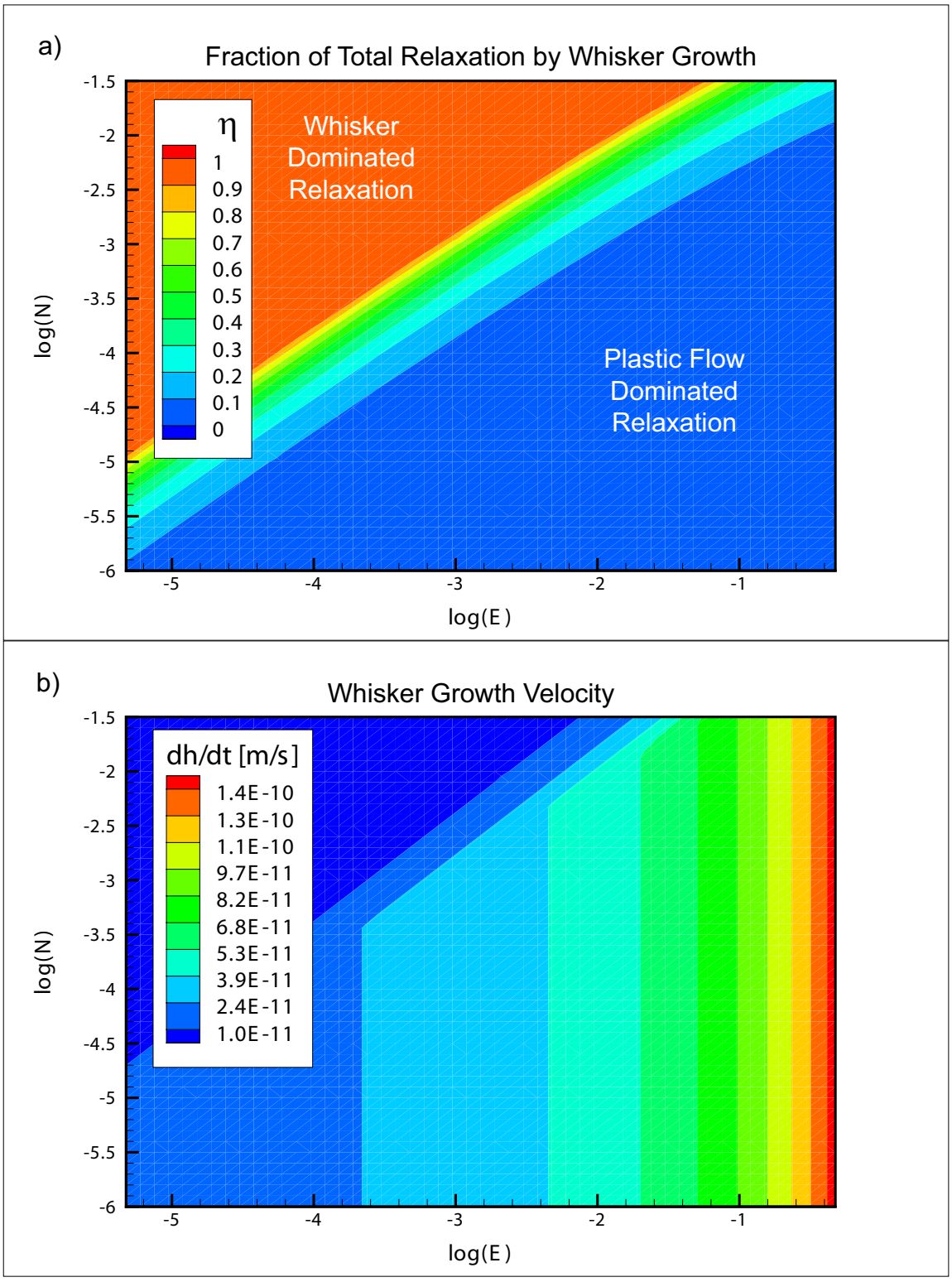

Figure 5.3: Contour plots showing the variations in a) fractional relaxation by whisker growth and b) whisker growth velocity over the parameter space of non-dimensional strain rate, E, and whisker density, N. Perfectly plastic behavior is assumed with material parameters identical to those used in the FEA in Chapter 3.

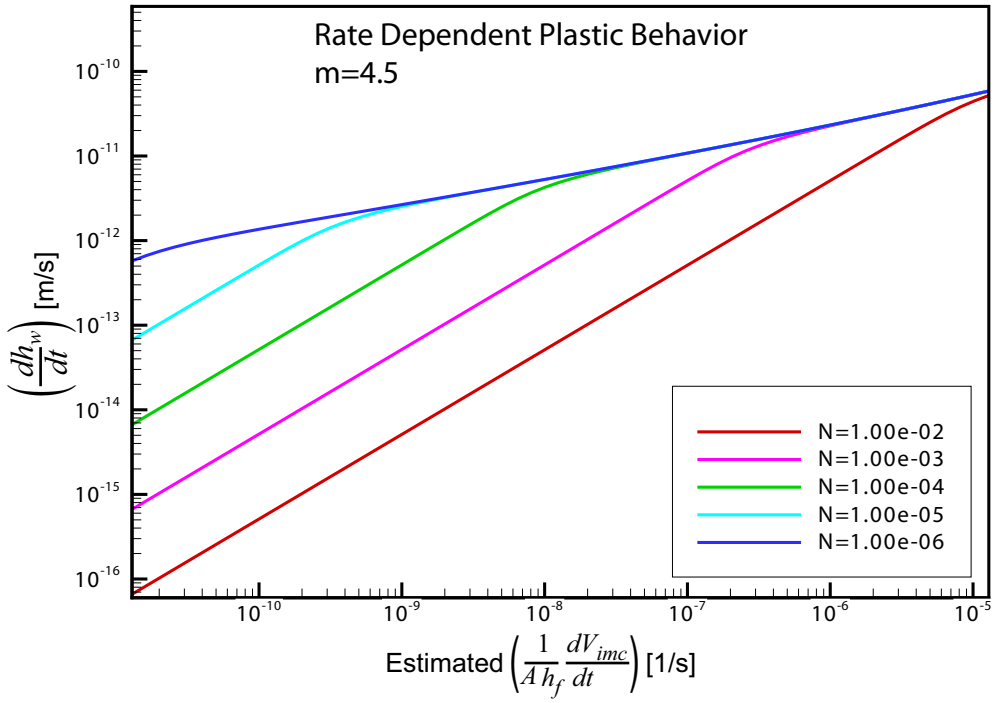

Figure 5.4: Whisker growth velocities predicted by solution of the steady-state boundary value problem for viscoplastic behavior. Rate-dependent plastic flow with power-law stress sensitivity is assumed with stress exponent $m = 4.5$ and material parameters for Sn as presented in Section 3.4.2 are used to calculate dimensional values.

Lower strain rate results in larger diffusion radius, and at a critical value the diffusion fields of neighboring whiskers begin to interact. This is fully analogous to the kinetic behavior described previously for the perfectly plastic material.

Solution of the time-dependent problem does not shed new light on the kinetic behavior. As would be expected, a stress gradient grows outward from the whisker until a steady-state balance between volume production and volume removal is achieved. However, the time-dependent solution can be extended to model the growth kinetics of whiskers formed by thermal stresses, as described in the following section.

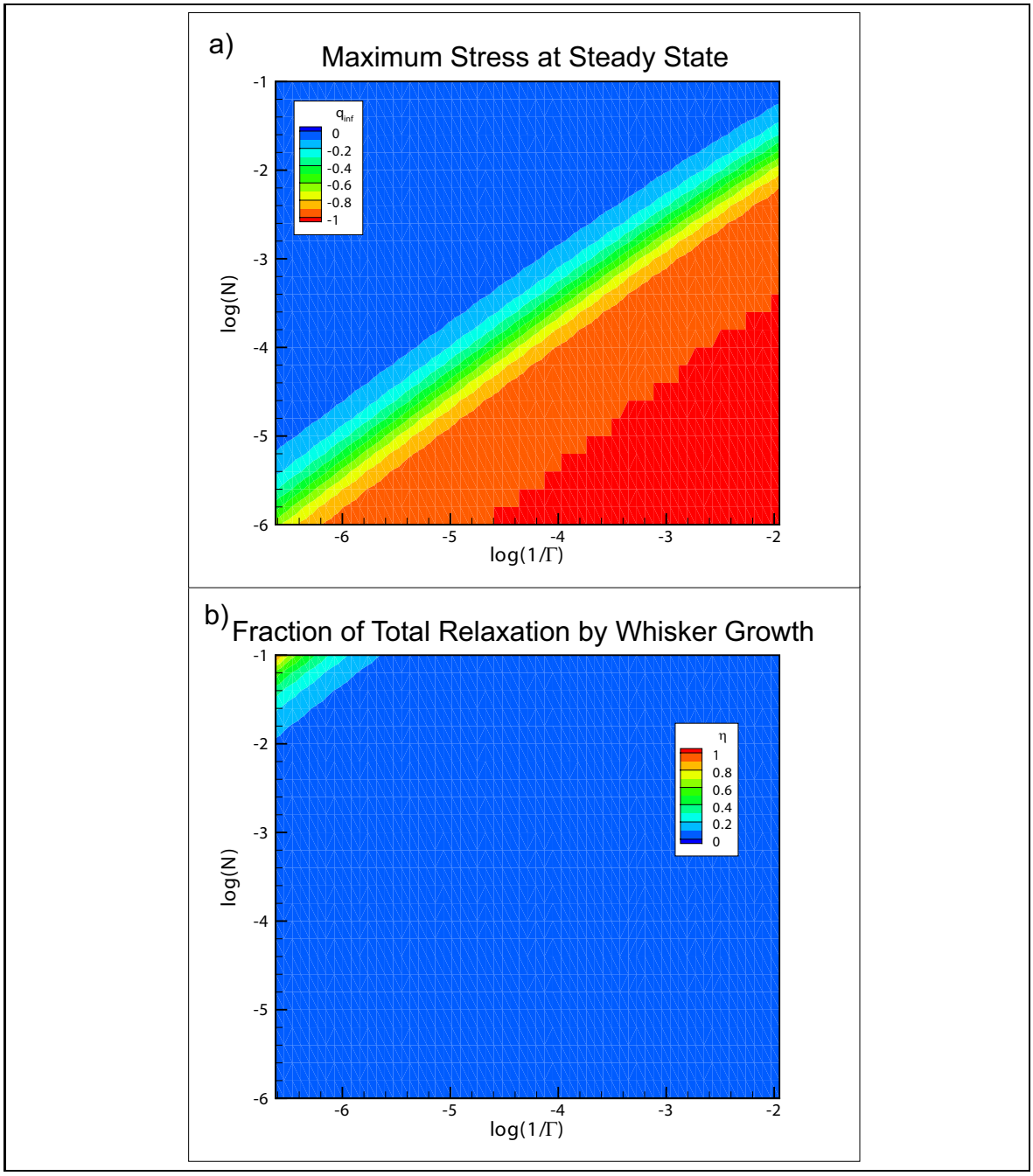

Figure 5.5: Contour plots showing the variations in a) maximum film stress and b) fractional relaxation by whisker growth over the parameter space of non-dimensional strain rate, $1/\Gamma$, and whisker density, N. Rate-dependent plastic flow with power-law stress sensitivity is assumed with stress exponent $m = 4.5$ and material parameters for Sn as presented in Section 3.4.2.

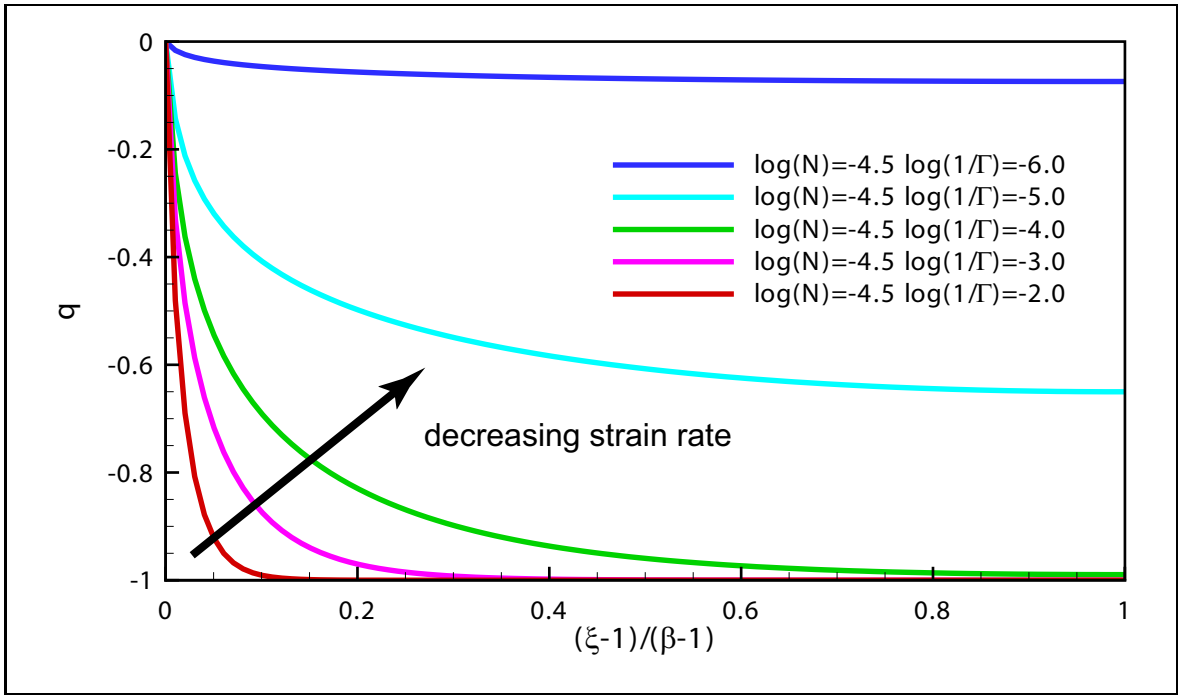

Figure 5.6: Steady-state stress distribution around a whisker for different values of non-dimensional strain rate, $1/\Gamma$, and fixed whisker density, N. Rate-dependent plastic flow with power-law stress sensitivity is assumed with stress exponent $m = 4.5$. At high applied strain rate, relaxation is limited to a radius less than half the whisker separation, analogous to the behavior observed for the perfectly plastic material.

5.5 *Extension to thermal cycling*

Thermally induced stress has been employed experimentally to produce whisker growth in Sn films deposited on non-reactive substrates [Chaudhari (1974), Nakadaira *et al.* (2007)]. The potential for whisker growth due to thermal cycling is of particular interest in the microelectronics industry because periodic temperature variation is often inherent in the environment in which electronic components operate. With the ability to efficiently solve the time-dependent transport problem afforded by the mathematical formulation in Section 5.3, we now have the potential to model the kinetics of whisker growth due to thermal cycling. The work presented here is preliminary, but it identifies a new area for more intensive future study.

The finite element solution for the time-dependent whisker growth problem is modified to allow for temperature dependent material properties. Specifically, the rate of strain generation is related to the rate of temperature change by the difference in thermal expansion coefficients, $\Delta\alpha$, between the film and substrate

$$\dot{\varepsilon}^* = \Delta\alpha \frac{dT}{dt}. \tag{5.49}$$

Both grain boundary diffusivity and viscoplastic flow rate vary exponentially with the inverse of temperature. In the finite element model we include this dependence as

$$\dot{\varepsilon}^p = \left[A\frac{\mu}{T}\exp\left(\frac{-Q_p}{kT}\right)\right]\left[\frac{|\sigma|}{\sigma_0}\right]^m \frac{1}{2}\frac{\sigma}{|\sigma|}. \tag{5.50}$$

and

$$D_{gb} = D^0_{gb}\exp\left(-Q_{gb}/kT\right) \tag{5.51}$$

where σ_0, A, D_0,Q_p, Q_{gb} and m are material parameters discussed previously in Sections 3.4.2 and 2.3.1. μ is the shear modulus which also has temperature dependence. We use the empirical model for μ given in Shin and Chason (2009) to get the temperature-dependent biaxial modulus, M

$$M = 2\mu\left(\frac{(1+\nu)}{(1-\nu)}\right) \qquad \text{where} \qquad \mu = 16302 \text{ MPa} - (40.5 \text{ MPa/C})T \tag{5.52}$$

and the temperature is specified in degrees Celsius.

In the finite element solution, the dimensionless coefficient, Γ, is updated at each increment based on a specified temperature-time curve. A preliminary result is shown in Figure 5.7 for an 8 μm film with Sn properties deposited on a silicon substrate subjected to a cyclic variation in temperature between -55°Cand +85°C. The temperature profile is shown at the top of the first graph. Our goal here is to test the feasibility

of the model and we realize that the imposed temperature variation may exceed the limits of validity of the assumed constitutive laws. The blue curve in the top graph tracks the total length of the whisker over three temperature cycles. A ratchet-like growth results due to the difference in material parameters during the high and low temperature hold periods. The variation of the plastic flow rate, diffusivity and stiffness over a single temperature cycle are shown in the bottom graph. During the high temperature portion of the cycle both plastic flow and diffusive transport to the whisker are fast processes (relative to the period of the cycle). Thus, even though compressive stress is quickly relaxed to approximately -10 MPa, as shown in the center graph, there is sufficient driving force to cause significant flow of material to the whisker.

Due to the total relaxation strain (both diffusive and intragranular flow) at high temperature, the film has a different stress-free reference state when the temperature cycle reverses. Thermal contraction now induces tensile stress. It should be noted that in our model formulation the process of material accumulation at the whisker is fully reversible, which may not be true in the physical system[1]. During the low temperature hold period, however, the characteristic rates of diffusion and plastic flow are orders of magnitude slower. Therefore, even though the magnitude of the film stress is over tens times greater than during the high temperature period due to the increased stiffness, the total amount of material removed from the whisker during the tensile phase is only a fraction of the amount that accumulated over the same time period at high temperature. The result is a thermal ratchet for whisker growth that requires no inherent irreversibility in any of the material behaviors.

Due to the reversibility of the material behavior, our model would predict asymmetric *removal* of material from the whisker if the film were bonded to a material

[1]Some degree of reversibility during hillock growth has been observed experimentally by Chaudhari (1974). There he documents the shrinkage of hillocks due to thermally-induced tensile stress.

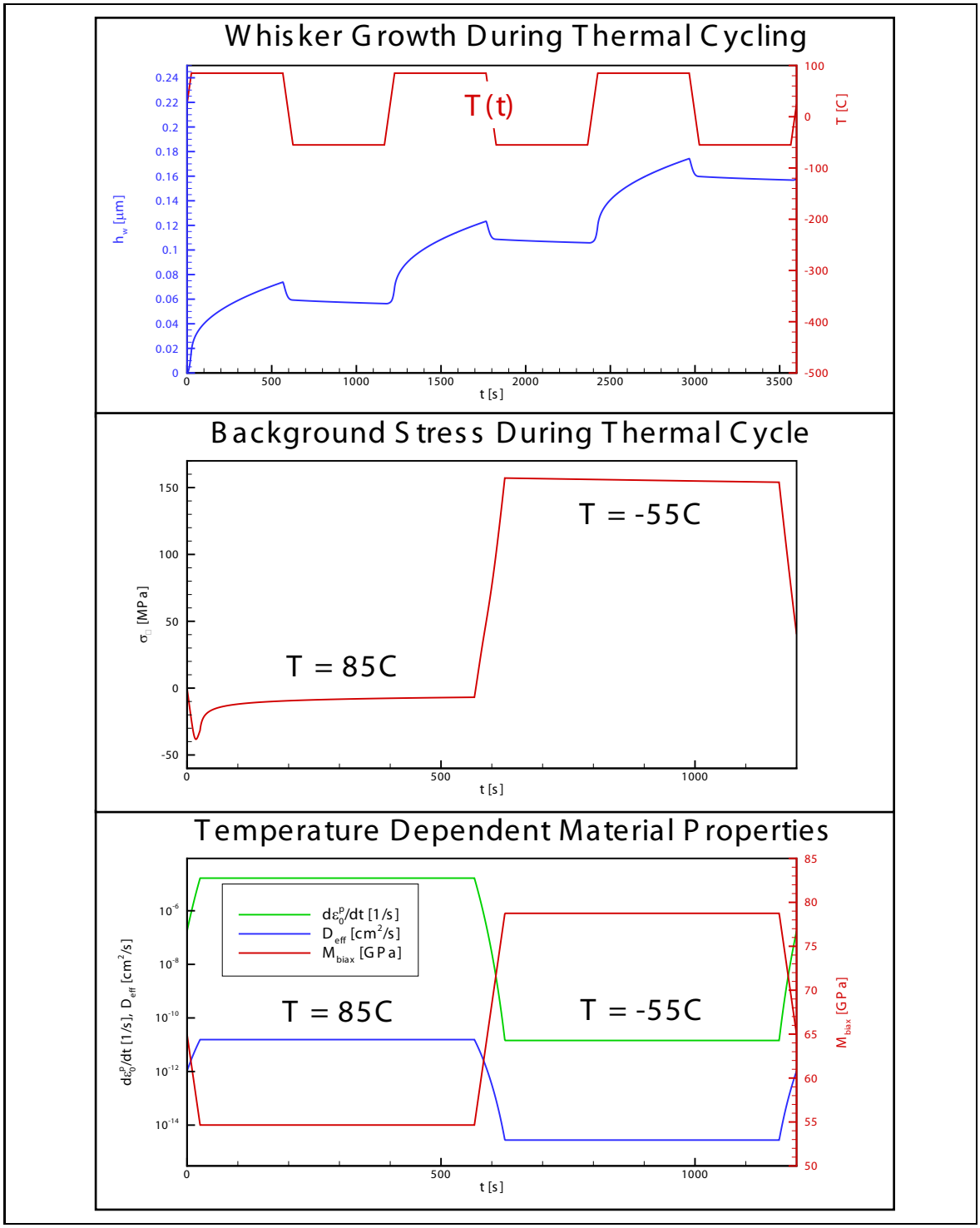

Figure 5.7: Results of 1-D finite element solution of the time-dependent viscoplastic model for a film subjected to ±65°Cthermal cycling. a) The applied temperature variation is shown in red along with the net whisker length as a function of time (blue). b) Stress variation over one cycle. c) Variation material properties over one cycle due to temperature variation.

with higher coefficient of thermal expansion. In this case, the film would be in tension at high temperature and compression at low temperature. Thus material would be removed from the grain with enhanced stress relaxation.

These results, although preliminary, suggest the possibility for further study of whisker growth kinetics involving the complementary use of experiment and computation. Experimentally, strain generation can be controlled through the temperature without the complication of non-uniform, localized IMC growth. This offers new possibilities for correlated simulation as well. Without IMC growth, deformation and stress are nearly constant through the thickness of the thin film, as is the columnar microstructure. Thus, the system is effectively two-dimensional, which greatly reduces the computational cost associated with finite element modeling. This would enable FEA of large areas of the film spanning many grains. Experimentally observed microstructures, including individual grain orientations, could be faithfully reproduced in models. The potential for direct correlation of model results with experimental measurements would warrant the development of FEA models with more realistic constitutive laws for Sn, including anisotropic elasticity and viscoplasticity and possibly grain boundary migration (grain growth).

5.6 Conclusions

In this chapter, a mathematical formulation describing the kinetics of mass transport to a whisker is developed. This work extends previous axisymmetric models of whisker growth [Chaudhari (1974), Lindborg (1976), Tu (1994), Hutchinson *et al.* (2004), Tu and Li (2005), Nakadaira *et al.* (2007)] by including the effects of two mechanical processes: strain generation and intra-granular plastic flow. The operation of these processes in Sn during whisker growth is supported by experimental evidence. An analytical solution is presented for the assumption of rate-independent

perfectly plastic behavior. This is analogous to the material behavior assumed in the FEA models in Chapter 4 and the predictions of the simplified model fully capture the kinetic behavior identified in that chapter.

The problem was also formulated for a material with viscoplastic behavior with power-law rate sensitivity. In this case numerical solution is necessary. The numerical solutions reveal that the kinetic behavior of a viscoplastic material with properties comparable to those of Sn is qualitatively very similar to that of the perfectly plastic material. Quantitatively, the viscoplastic model predicts whisker growth velocities approximately an order of magnitude lower than the perfectly plastic model. The partitioning of strain relaxation is also significantly different, with plastic flow accounting the majority of relaxation over a broad range of the parameter space.

Finally, we present a time-dependent formulation for viscoplastic material behavior that also permits the inclusion of temperature-dependent material behavior in the one-dimensional finite element code written to solve the initial-boundary value problem. Preliminary results of this model suggest that ratchet-like behavior for whisker growth can result from fully reversible material behaviors under thermal cycling. This also suggests the opportunity for further study of the fundamental processes and features controlling whisker kinetics through correlated computation and experiment on Sn films subjected to thermal cycling.

Chapter 6

Conclusions

In the preceding chapters we have examined the nature of the coupling among several features and processes known to be involved in the complex material system that leads to the formation of whiskers from Sn films. These include the phase transformation reaction between Sn-Cu (growth of IMC) which generates strain within the Sn, the elastic and plastic deformation within the Sn grains, and the long-range transport of Sn within the film by grain boundary diffusion. There is strong experimental evidence indicating each of these processes is involved in the whisker formation process. What we have attempted to do here is explore the relationships and interactions among these material processes to better understand how their collective behavior gives rise to whisker formation.

Quantitative analysis based on the principles of mechanics has been used to evaluate the consequences of different assumptions about material behavior and microstructure. Through the use of computational modeling, we have been free to include or exclude individual features of the model system and quantitatively predict the corresponding response of the system. Probing the system in this manner, we have been able to assess the relative importance and mutual interactions among material behaviors known to operate in the Sn-Cu system. The following picture of stress generation

and whisker growth emerges from this work.

In Chapter 3 we investigated the mechanisms of stress generation and simultaneous relaxation operating within the Sn film. Most significantly, we found that the coupled actions of intra-granular plastic flow and mass transport by grain boundary diffusion are sufficient to account for both the rapid build-up of compressive stress in response to IMC growth, and the maintenance of that stress at a constant level as the volume of IMC continues to increase. We also found that both the columnar microstructure of the film and a surface oxide layer that prevents diffusion out of grain boundaries are necessary conditions for the development of compressive stress. The morphology of the IMC growth is also critically important, as the expansion associated with the IMC transformation reaction must occur *within* the Sn film. Growth of IMC as a uniform layer provides no mechanism for stress generation within the Sn.

The conclusion that deformation within the Sn film is sufficient to produce the observed stress history *in the absence of whisker growth* raises a number of questions about the role whisker growth plays in the overall relaxation of strain within the film. These questions are addressed in Chapter 4 where we find that the kinetics of mass transport to a whisker are governed by the mutual interaction of grain boundary diffusion and intra-granular plastic flow. Under the model assumptions of elastic-perfectly plastic behavior, strain relaxation in the film is segregated between regions that are relaxed exclusively by mass diffusion to a whisker and regions relaxed exclusively by intra-granular plastic flow. Although the sharpness of the division can be attributed to the overly simple plasticity model for Sn, the FEA results reveal how the competition between the two relaxation mechanisms controls the kinetics of mass transport to the whisker.

The behavior suggested by the modeling resolves several important questions. First, we find that the size of the region supplying material to the whisker (the

diffusion field) is determined by the rate of strain generation relative to the rate of diffusive transport. As the normalized rate of strain generation decreases, the size of the diffusion field increases. As consequence the net flux of volume to the whisker (and thus the whisker growth velocity) varies only weakly with strain rate. When a finite density of whiskers is present, a second kinetic regime is possible. At sufficiently low strain rates the diffusion fields of neighboring whiskers begin to interact and whisker growth becomes the primary strain relaxation mechanism. In this regime, whisker growth velocity scales linearly with rate of strain generation. FEA results provide quantitative estimates of whisker growth velocity and allow the partitioning of strain relaxation to be quantified as well. The predicted growth velocities from our model are in excellent agreement with reported average whisker growth rates, and significantly, the diffusion radius arises naturally out the model. Recent whisker growth rate measurements made by continuous observation of individual whiskers over a period of days, however, are roughly an order of magnitude larger.

Finally, two mathematical descriptions of whisker growth kinetics are presented in Chapter 5 that account for the behavior observed through FEA. The first model, based on the assumption of perfect plasticity in the Sn, is a limiting case of the more general model that assumes rate-dependent viscoplasticity with power-law stress sensitivity. For rate-dependent plastic behavior with material constants appropriate to Sn, the model predicts that whisker growth should account for a small fraction of total strain relaxation and lower whisker growth rates over the range of experimentally measured IMC growth rates and whisker densities.

These findings have a number of implications for the control of stress and mitigation of whisker growth in real Sn-Cu films. Both the columnar microstructure and passivating oxide layer appear to be necessary for stress generation in the Sn film. Therefore, alloy compositions or processing techniques that disrupt these features

should also reduce stress within the Sn. We note, however, that continuous strain relaxation, equal to the rate of strain generation, is necessary to maintain low stress levels as long as IMC growth continues. Thus, changes such as the later development of an oxide layer, would allow stress to build as long as IMC growth continues.

The morphology of the IMC phase is also important, and processing that promotes the growth of IMC as a uniform layer, rather than discrete particles, will also reduce stress in the Sn. The effectiveness of the industrial post-bake mitigation treatment would appear to be due, at least in part, to the uniform layer IMC morphology it promotes. Continued IMC growth will not produce stress, in the Sn as long as the IMC remains smooth. However, if subsequent IMC growth is non-uniform, such as might result from preferential growth into Sn-Sn grain boundaries, stress would be generated in the film.

The whisker growth kinetics results indicate that, at least early in the process of whisker formation, when whisker densities are low, whisker growth can account for only a small fraction of the total relaxation in the film. The whisker growth velocities in this regime are relatively insensitive to the rate of IMC growth. Therefore, strategies that reduce IMC growth rate will not necessarily result in an equivalent reduction in whisker growth rate. The question of whether the whisker density eventually becomes great enough that whisker growth dominates the strain relaxation remains unanswered. Experimental stress measurements correlated with whisker densities suggest that whiskers are not the dominant relaxation mode.

Another unresolved question regards the effect of viscoplastic creep. Based on the model results we would expect a greater degree of stress relaxation due to viscoplastic creep in the Sn than is observed experimentally. This may indicate that the effectiveness of creep relaxation is reduced in Sn-Cu films relative to pure Sn films on non-reactive substrates. Alternatively this could result from hardening due to the

large plastic deformation in the Sn caused by IMC growth or Cu precipitation in the Sn, or from features of the real material behavior or microstructure not included in the idealized model presented here.

Hopefully, the work presented in this thesis provides valuable insight into the nature of the relationships among important material processes involved in whisker growth. The picture that emerges, however, is painted with a broad brush. Many of the more puzzling aspects of whisker growth, such as what controls where and when whiskers nucleate and what causes whiskers to stop, restart, and change directions during growth, remain hidden in the details.

Bibliography

Arnold, S. M. (1959), 'The growth of metal whiskers on electrical components', *Proc. of the IEEE Elec. Comp. Conf.* pp. 75–82.

Barrett, C. S. (1943), *Structure of Metals*, 1 edn, McGraw-Hill, New York.

Bieler, T. R., Jiang, H., Lehman, L., Kirkpatrick, T., Cotts, E. J. and Nandagopal, B. (2008), 'Influence of Sn Grain Size and Orientation on the Thermomechanical Response and Reliability of Pb-free Solder Joints', *IEEE Transactions on Components and Packaging Technologies* **31**(2), 370–381.

Boettinger, W. J., Johnson, C. E., Bendersky, L. A., Moon, K.-W., Williams, M. E. and Stafford, G. R. (2005), 'Whisker and hillock formation on Sn, Sn-Cu and Sn-Pb electrodeposits', *Acta Materialia* **53**, 5033–5050.

Bower, A. F. (2010), *Applied Mechanics of Solids*, CRC Press, Boca Raton, FL.

Bower, A. F. and Wininger, E. (2004), 'A two-dimensional finite element method for simulating the constitutive response and microstructure of polycrystals during high temperature plastic deformation', *Journal of the Mechanics and Physics of Solids* **52**, 1289–1317.

Chason, E., Jadhav, N., Chan, W. L., Reinbold, L. and Kumar, K. S. (2008), 'Whisker

formation in Sn and Pb-Sn coatings: Role of intermetallic growth, stress evolution, and plastic deformation processes', *Applied Physics Letters* **92**, 171901.

Chaudhari, P. (1974), 'Hillock growth in thin films', *Journal of Applied Physics* **45**(10), 4339–4346.

Chen, T. and Dutta, I. (2008), 'Effect of Ag and Cu concentrations on the creep behavior of Sn-based solders', *Journal of Electronic Materials* **37**, 347.

Choi, W. J., Lee, T. Y., Tu, K. N., Tamura, N., Celestre, R. S., MacDowell, A. A., Bong, Y. Y. and Nguyen, L. (2003), 'Tin whiskers studied by synchrotron radiation scanning X-ray micro-diffraction', *Acta Materialia* **51**, 6253–6261.

Deng, X., Chawla, N., Chawla, K. K. and Koopman, M. (2004), 'Deformation behavior of (Cu,Ag)–Sn intermetallics by nanoindentation', *Acta Materialia* **54**, 4291–4303.

Du, N. (2009), Multiscale modeling of deformation and failure mechanisms of Al alloys at elevated temperature, PhD thesis, Brown University.

Ellis, W. C., Gibbons, D. F. and Treuting, R. G. (1958), *Growth of metal whiskers from the solid*.

Fields, R. J., III, S. R. L. and Jr., G. K. L. (n.d.), *Metal science of joining*.

Fisher, R. M., Darken, L. S. and Carroll, K. G. (1954), 'Accelerated growth of tin whiskers', *Acta Metallurgica* **2**, 368.

Freund, L. B. and Suresh, S. (2003), *Thin Film Materials*, Cambridge University Press, Cambridge.

Frost, H. J. and Ashby, M. F. (1982), *Deformation-Mechanism Maps: The Plasticity and Creep of Metals and Ceramics*, Pergamon Press, Elmsford, NY.

Fujiwara, M. and Hirokawa, T. (1987), 'The strength of main obstacles to dislocation motion in white tin crystals', *Journal of The Japan Institute of Metals* **51**(9), 830–838.

Gale, W. F. and Totemeier, T. C., eds (2004), *Smithells metals reference book*, 8 edn, Elsevier Butterworth-Heinemann.

Galyon, G. T. (2004), A history of tin whisker theory: 1946 to 2004, SMTAI International conference.

Galyon, G. T. (2005), 'Annotated tin whisker bibliography and anthology', *IEEE Transactions on Electronic Packaging Manufacturing* **28**(1), 94–122.

Galyon, G. T. and Palmer, L. (2005), 'An integrated theory of whisker formation: The physical metallurgy of whisker formation and the role of internal stresses', *IEEE Transactions on Electronic Packaging Manufacturing* **28**(1), 17–30.

Hirokawa, T., Yomogita, K. and Honda, K. (1968), 'Dependence of strain rate on stress and temperature in tin single crystals', *Transactions of the Japan Institute of Metals* **9**, 837–842.

Hutchinson, W. B., Oliver, J., Nylén, M. and Hagstroem, J. (2004), 'Whisker growth from tin coatings', *Materials Science Forum* **467–470**, 465–470.

iNEMI (2006), iNEMI recommendations on lead-free finishes for components use in high-reliability products: version 4 (12-1-06), Technical report, International Electronics Manufacturing Initiative.

Jadhav, N., Buchovecky, E., Reinbold, L., Kumar, S., Bower, A. F. and Chason, E. (2010), 'Understanding the correlation between intermetallic growth, stress evolution and Sn whisker nucleation', *IEEE Transactions on Electronic Packaging Manufacturing*. [accepted].

Kerr, M. and Chawla, N. (2004), 'Creep deformation behavior of Sn-3.5Ag solder at small length scales', *Journal of the Minerals, Metals and Materials Society* pp. 50–54.

Kirichenko, G. I. (1987), 'Anisotropy of plastic deformation of tin single crystals in the temperature range 4.2–300K', *The Physics of Metals and Metallography* **63**(1), 144–151.

Krishnamurthy, R. and Srolovitz, D. J. (2005), 'Reaction layer growth in a substrate/polycrystalline film system', *Acta Materialia* **53**, 5189–5902.

Kumar, K. S., Reinbold, L., Bower, A. F. and Chason, E. (2008), 'Plastic deformation processes in Cu/Sn bimetallic films', *Journal of Materials Research* **23**, 2916–2934.

Lange, W. and Bergner, D. (1962), 'Messung der korngrenzenselbstdiffusion in polykristallinem zinn', *Physica Status Solidi* **2**, 1410–1414.

Lee, B. Z. and Lee, D. N. (1998), 'Spontaneous growth mechanism of tin whiskers', *Acta Metallurgica* **46**, 3701.

Lin, S. K., Yorikado, Y., Jiang, J. X., Kim, K. S., Suganuma, K., Chen, S. W., Tsujimoto, M. and Yanada, I. (2007), 'Microstructure development of mechanical-deformation-induced sn whiskers', *Journal of Electronic Materials* **36**(12), 1732–1734.

Lindborg, U. (1975), 'Observations on the growth of whisker crystals from zinc electroplate', *Metallurgical Transactions A* **6A**, 1581–1586.

Lindborg, U. (1976), 'A model for the spontaneous growth of zinc, cadmium and tin whiskers', *Acta Metallurgica* **24**(2), 181–186.

Malvern, L. E. (1969), *Introduction to the mechanics of a continuous medium*, Prentice-Hall, Englewood Cliffs, NJ.

Mathew, M. D., Yang, H., Movva, S. and Murty, K. L. (2005), 'Creep deformation characteristics of tin and tin-based electronic solder alloys', *Metallurgical and Materials Transactions A* **36**, 99.

McCabe, R. J. and Fine, M. E. (2002), 'Creep of tin, Sb-strengthened tin, and SbSn-precipitate-strengthened tin', *Metallurgical and Materials Transactions A* **33A**, 1531–1539.

Nagasaka, M. (1989), 'Temperature dependence of plastic deformation in white tin single crystals', *Japanese Journal of Applied Physics* **28**(3), 446–452.

Nagasaka, M. (1999), 'Strain-rate and temperature dependence of plastic deformation in white tin single crystals', *Japanese Journal of Applied Physics* **38**(1A), 171–175.

Nakadaira, Y., Jeong, S., Shim, J., Seo, J., Min, S., Cho, T., Kang, S. and Oh, S. (2007), 'Growth of tin whiskers for lead-free plated leadframe packages in high humid environments and during thermal cycling', *Microelectronics Reliability* **47**, 1928–1949.

NASA (2009), 'http://nepp.nasa.gov/whisker'.

Pitt, C. H. and Henning, R. G. (1964), 'Pressure-induced growth of metal whiskers', *Journal of Applied Physics* **35**, 459–460.

Reinbold, L. K. (2007), Kinetics of interfacial reaction and stress evolution in bimetallic copper-tin thin films, PhD thesis, Brown University.

Reinbold, L. K., Jadhav, N., Chason, E. and Kumar, K. S. (2009), 'Relation of Sn

whisker formation to intermetallic growth: Results from a novel SnCu bimetal ledge specimen', *Journal of Materials Research* **24**(12), 3583–3589.

Sheng, G. T. T., Hu, C. F., Choi, W. J., Tu, K. N., Bong, Y. Y. and Nguyen, L. (2002), 'Tin whiskers studied by focused ion beam imaging and transmission electron microscopy', *Journal of Applied Physics* **92**(1), 64–69.

Shibutani, T., Yu, Q., Yamashita, T. and Shiratori, M. (2006), 'Stress-induced tin whisker initiation under contact loading'.

Shin, J. W. and Chason, E. (2009), 'Stress behavior of electroplated Sn films during thermal cycling', *Journal of Materials Research* **24**(4), 1522–1528.

Smetana, J. (2007*a*), 'iNEMI updates tin whisker recommendations', *Global SMT and Packaging* **7**(6), 14–18.

Smetana, J. (2007*b*), 'Theory of Tin Whisker Growth: "The End Game"', *IEEE Transactions on Electronic Packaging Manufacturing* **30**(1), 11–22.

Sobiech, M., Welzel, U., Mittemeijer, E. J., Hugel, W. and Seekamp, A. (2008), 'Driving force for Sn whisker growth in the system Cu–Sn', *Applied Physics Letters* **93**(1), 011906.

Sobiech, M., Wohlschlogel, M., Welzel, U., Mittemeijer, E. J., Hugel, W., Seekamp, A., Liu, W. and Ice, G. E. (2009), 'Local, submicron, strain gradients as the cause of Sn whisker growth', *Applied Physics Letters* **94**(22), 221901.

Tsuji, K. (2003), 'Role of grain boundary free energy and surface free energy for tin whisker growth', *in Proc. of the IPC-JEDEC Conf.* pp. 169–186.

Tu, K. N. (1973), 'Interdiffusion and reaction in bimetallic Cu-Sn thin films', *Acta Metallurgica* **21**(4), 347–354.

Tu, K. N. (1994), 'Irreversible processes of spontaneous whisker growth in bimetallic Cu-Sn thin-film reactions', *Physical Review B* **49**(3), 2030–2034.

Tu, K. N. (1996), 'Cu/Sn interfacial reactions: thin-film case versus bulk case', *Materials Chemistry and Physics* **46**, 217–223.

Tu, K. N. and Li, J. C. M. (2005), 'Spontaneous whisker growth on lead-free solder finishes', *Materials Science and Engineering A* **409**, 131–139.

Tu, K. N. and Thompson, R. D. (1982), 'Kinetics of Interfacial Reaction in Bimetallic Cu-Sn Thin-Films', *Acta Metallurgica* **30**(5), 947–952.

Vianco, P. T. and Rejent, J. A. (2009), 'Dynamic recrystallization (DRX) as the mechanism for Sn whisker development. Part I: A model', *Journal of Electronic Materials* **38**(9), 1817–1825.

Weertman, J. and Breen, J. E. (1956), 'Creep of tin single crystals', *Journal of Applied Physics* **27**(10), 1189–1193.

Zamiri, A., Bieler, T. R. and Pourboghrat, F. (2008), 'Anisotropic Crystal Plasticity Finite Element Modeling of the Effect of Crystal Orientation and Solder Joint Geometry on Deformation after Temperature Change', *Journal of Electronic Materials* **38**(2), 231–240.

Zhang, W., Egli, A., Schwager, F. and Brown, N. (2005), 'Investigation of Sn-Cu intermetallic Compounds by AFM: New aspects of the role of intermetallic compounds in whisker formation', *IEEE Transactions on Electronic Packaging Manufacturing* **28**(1), 85–93.

Zhao, J.-H., Su, P., Ding, M., Chopin, S. and Ho, P. S. (2006), 'Microstructure-based stress modeling of tin whisker growth', **29**(4), 265–273.